SHAPE COEXISTENCE IN ^{151}Gd

SHAPE COEXISTENCE IN ^{151}Gd

by

HAROLD JOHN SMITH, B.Sc., M.Sc.

A Thesis
Submitted to the School of Graduate Studies
in Partial Fulfilment of the Requirements
for the Degree
Doctor of Philosophy

McMaster University
August,1977.

DOCTOR OF PHILOSOPHY (1977)
(Physics)

McMASTER UNIVERSITY,
Hamilton, Ontario

TITLE: Shape Coexistence in ^{151}Gd

AUTHOR: Harold John Smith, B.Sc.(Tor.), M.Sc.(Guelph)

SUPERVISOR: Dr. M.W.Johns

NUMBER OF PAGES: viii, 202

ABSTRACT

The level structure of the odd-A transitional nucleus ^{151}Gd has been studied by means of the ^{149}Sm(α,2n)^{151}Gd reaction through γ-ray singles, γ-ray angular distributions, γ-γ coincidence and conversion electron measurements.

A number of rotational band-like structures have been observed, indicating that the nucleus is deformed when produced in this reaction. A rotational band built on one of the states populated in the reaction conforms well to present theory and indicates that the nucleus has a large deformation when this state is populated. The other bands are not well explained by present theory, although a much smaller nuclear deformation is indicated.

The implication is that the Nilsson model, in its present stage of development, is inadequate for treating nuclei such as ^{151}Gd. Further theoretical work is necessary particularly in the treatment of multiple particle states where j is not a good quantum number and the core is not a rigid rotor.

ACKNOWLEDGEMENTS

I thought at first that it would be a simple task to say 'Thank You' to those to whom I am indebted after finishing this project. However, I now find that it is impossible to describe in a few words the feelings and relationships that have developed during four years of team work. It is a period where you both learn from and give to your colleagues. A period during which you develop the skills to coax Nature into yielding her secrets and the insight to interpret what she tells you. I have thoroughly enjoyed the easy camaraderie of the McMaster Tandem Accelerator Laboratory and the helpful Computer Science staff of the university.

It is fitting that a number of people should receive special thanks for the strong role that each has played in my personal development.

Dr. M.W. Johns, my supervisor, whose complete honesty, objectivity and perseverence I have adopted as my personal models and for his substantial help in the preparation of this thesis.

Drs. D.G. Burke and G. King, the other members of my supervising committee for their advice.

Dr. J.C. Waddington, a friend and associate, who introduced me to the mysteries and techniques of accelerator experiments and initially suggested the work on ^{151}Gd, for many fruitful discussions, timely suggestions and assistance in performing the experiments.

Dr.W.B. Cook for tutoring me in the interpretation of coincidence data and bridge hands and help in performing the experiments.

Dr.G. Løvhøiden for his helpful discussions on rotational bands, friendship and assistance in performing the experiments.

Dr.T.L. Khoo, whose earlier work had left the 'Orange' β-ray spectrometer in fine working condition.

Dr.D. Kelley for his assistance with the laboratory computers.

Dr.O. Straume for his assistance with the theoretical interpretation.

Dr.A.Volkov for his personal interest and assistance with the theoretical interpretation.

Dr.J.Thompson and Miss K.Marshall for assistance with the experiments.

Mrs.E.Williams, Mrs.L.Reschke and Miss J.Balogh who assisted in the early preparation of the thesis.

My wife, Ilene, without whose support throughout the years and help with the final draft this project would never have been finished.

Finally, I wish to acknowledge with gratitude the National Research Council of Canada for their support in the form of a scholarship.

TABLE OF CONTENTS

CHAPTER Page

5 EXPERIMENTAL RESULTS FOR ^{151}Gd

6 DISCUSSION OF EXPERIMENTAL RESULTS

Chapter 1

INTRODUCTION

With the development of machines capable of accelerating a wide range of charged particles, the heavy ion, xn reactions have become very popular. The reaction of a heavy ion with a nucleus generally transfers a large amount of angular momentum and hence populates high spin states in the residual nucleus which are not excited in proton or deuteron reactions. The development of high resolution Ge(Li) radiation spectrometers about 15 years ago, has made it possible to study the very complex gamma ray spectra created by the xn reactions. These developments have resulted in high quality data on classes of nuclear states which had previously been unknown and to apply stringent tests to current nuclear models.

For nuclei which exhibit a stable spherical shape the shell model adequately describes the observed behaviour. For deformed nuclei, the unified model, which combines single particle motions with pairing correlations and collective effects has been very successful. Between these two extremes there are a number of nuclei which are not adequately described by either model. These are called the transitional nuclei in which one might expect to find aspects of both spherical and deformed behaviour. A study of these nuclei serves to indicate the range of applicability of both models.

A large number of rare earth nuclei have been studied at the McMaster tandem laboratory and have provided initial tests of the Nilsson model. In particular, the band based on the $11/2^-$ [505] state has been identified in a number of nuclei near the lower end of the deformed region. This project was undertaken to discover if this rotational band was populated in ^{151}Gd which has two less neutrons than the lightest nucleus in which this band had been found. An analysis of the properties of this band in ^{151}Gd forms part of this thesis.

Since the $11/2^-$ state had been found to be isomeric in ^{153}Gd and ^{155}Gd (Løvhøiden 1972, Løvhøiden 1970, Borrggreen 1969) a search for isomerism in ^{151}Gd was conducted using pulsed beam techniques and the ^{149}Sm(^{4}He, 2n) reaction. All these attempts failed but many new gamma rays and band structures in ^{151}Gd were found. The delineation of the properties of these bands and their interpretation forms the major portion of this thesis.

Chapter 2

NUCLEAR SPECTROSCOPY WITH HEAVY IONS

2.1 A Simple View of Heavy Ion Induced Reactions

The brief discussion which follows draws heavily on the excellent review article by J.O. Newton (1969). For the purpose of reaction studies, the term 'heavy ion' is used in referring to all projectiles of mass >2. In these reactions, the incoming projectile combines with the target to form a compound nucleus in a highly excited state. This nucleus loses energy by the evaporation of neutrons and charged particles or by fission. In light nuclei where the Coulomb barrier is low, charged particle evaporation competes favourably with neutron emission. For medium mass nuclei, the Coulomb barrier is sufficient to reduce the charged particle cross sections to the point where neutron evaporation is dominant. For heavy nuclei (Z >80) fission becomes competitive with the (HI, xn) process.

In the rare earth region of concern in this thesis, the total (HI, xn) cross section is ∿1 barn and that for other reactions is negligible. A schematic picture of the process is illustrated in Figure 2-1 which depicts the situation for a $^{149}_{62}Sm_{87}$ target bombarded by 24 MeV alpha particles. These particles have

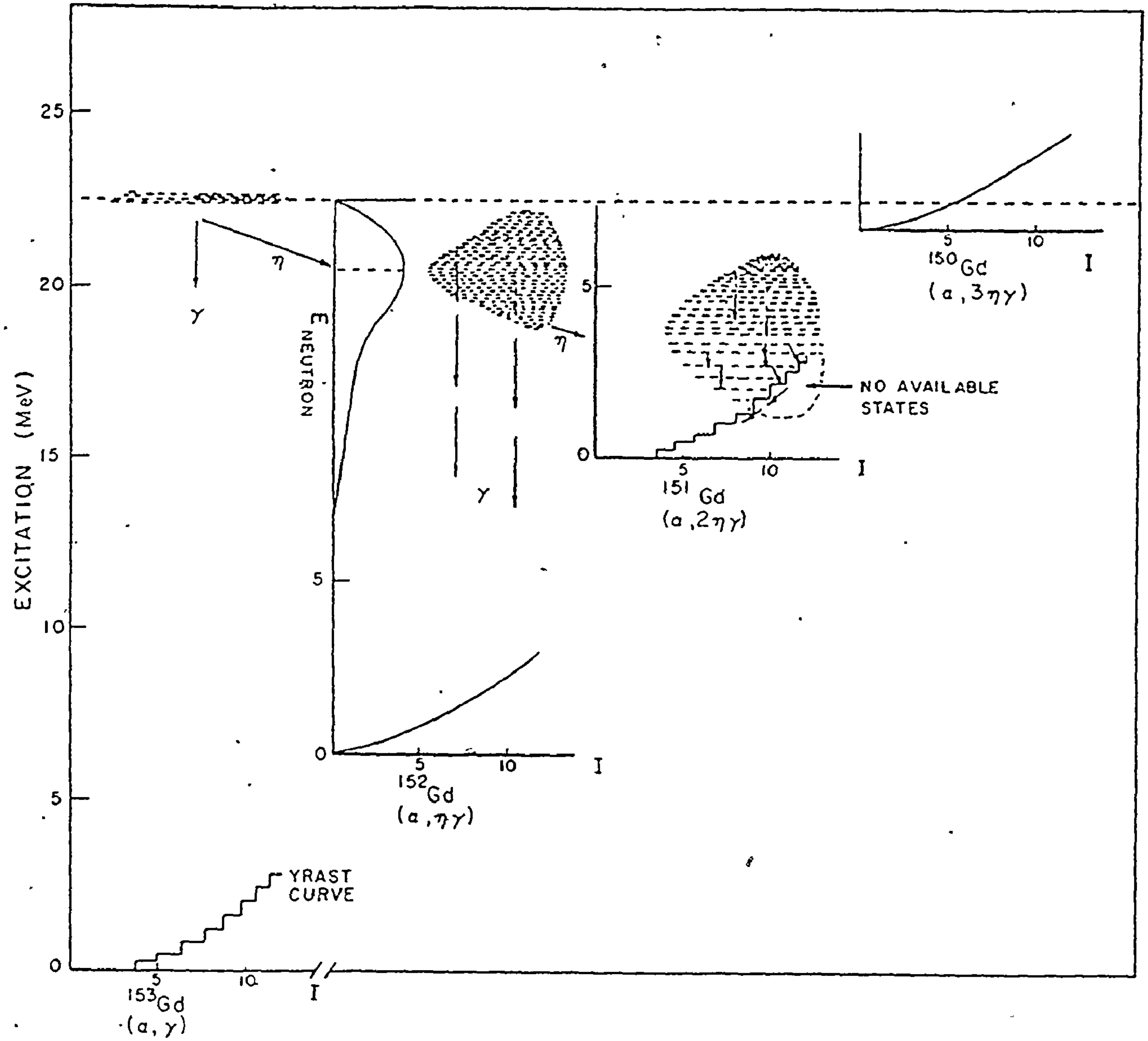

Figure 2-1

A schematic picture of the (α,xn) reactions for a ^{149}Sm target bombarded by 24 MeV α particles. (Based on a drawing by J.O.Newton,1969) energy sufficient to penetrate the Coulomb barrier and create a ^{153}Gd compound nucleus with excitation energy 22.4 MeV (the Q value of the ^{149}Sm(α,γ) ^{153}Gd reaction is -1.6 MeV). Since the (α,n), (α,2n) and (α,3n) reactions have Q values of -8.08, -16.6 and -23.2 MeV respectively, the maximum excitation energies available for ^{152}Gd, ^{151}Gd and ^{150}Gd are 16.0, 7.4 and 0.8 MeV respectively. Since the neutrons emitted in these reactions have a broad spectrum of energies peaking at ∿2 MeV (see insert in the ^{152}Gd column), ^{152}Gd will be produced with excitations ranging from approximately 7 MeV to 16 MeV with a maximum population of states around 14 MeV. In the same way ^{151}Gd will be formed with excitations ranging from 0 to 7.6 MeV with a maximum population of states at ∿4 MeV. The cross section for the (α,3n) reaction will be negligible. Under the conditions of this sketch, neutron emission is highly favoured over gamma ray emission in both ^{153}Gd and ^{152}Gd while gamma emission is the only de-excitation process available in ^{151}Gd.

2.2 Excitation Functions

Heavy ion reactions are characterized by the large amount of angular momentum transferred to the compound nucleus. In terms of the total angular momentum I this is given by $\sqrt{I(I+1)}\,\hbar$. Since, even with alpha beams, the experimental data show that I may be as large as 10 - 15 units of $\hbar$ one will not go far wrong by using the classical expression for angular momentum (L) :

$$L = \sqrt{2ME}\ .\ b$$

where M is the projectile mass and E its kinetic energy.

We see that for a given impact parameter, b, L increases as $\sqrt{E}$ and as $\sqrt{M}$. Since neither neutron nor dipole radiation can carry away much angular momentum from the nucleus the angular momentum initially imparted to the compound nucleus persists in the residual nucleus to rather low levels of excitation. For each of the gadolinium nuclei shown in Figure 2-1, I is plotted along the x-axis as a measure of the nuclear angular momentum present. The shaded areas roughly indicate the distribution in both energy and momentum of the states populated when these nuclei are formed.

The 'yrast' curve shows the excitation of the lowest state of a given I in a given nucleus as a function of I. In ^{153}Gd it is possible for an initial state with any value of I to deexcite either by dipole emission to a state of similar spin in ^{153}Gd, or by neutron emission to a state of similar spin in ^{152}Gd. In ^{152}Gd neutron emission from high spin states at the lower excitation edge of the population region would be impossible since the 8 MeV loss in excitation associated with neutron evaporation would place the final state below the yrast curve for ^{151}Gd. Since a relatively small increase in beam energy would lift the population region for ^{151}Gd above the yrast curve, it is clear that the intensity with which high spin states are populated is a sensitive and rapidly varying function of beam energy. The cross section for population of low spin states, on the other hand, will be relatively insensitive to this variable.

The same type of qualitative arguments can be used to explain why the cross section for the (α,n) reaction increases rapidly from zero at the threshold to a maximum and then begins to fall off as the beam energy passes the threshold for the (α,2n) reaction.

By measuring the intensity of each gamma ray as a function of beam energy one can identify the reaction which led to its production and hence the residual nucleus to which the gamma ray belongs. Further, as indicated above, the yield curves of the various gamma rays may also be a rough indicator of the spin of the initial state involved.

An attempt was made by Jackson (1956) to use the statistical model to calculate excitation functions. It was adequate to deal with xn reactions induced by light ions such as protons where rather a small amount of angular momentum is brought into the compound system. It is, however, not adequate to deal with reactions induced by heavy ions where as much as 20-100 units can be brought into the system depending on the ions used. A proper theory of the heavy ion induced reactions requires consideration of the angular momentum dependence of level density, competition from fission, charged particle and gamma ray emission and the reduction of the compound nucleus cross section by reactions occurring near to the nuclear surface, none of which were included by Jackson. Grover and Gilat (1967, a,b,c), Grover (1967) and Jagare (1967) have made more realistic calculations which have included some of these features, but ignoring the surface reactions. Unfortunately they did not attempt to calculate excitation functions so their theory has been of little direct use in this work.

2.3 Angular Distributions

The residual nuclei produced in (HI,xn) reactions are strongly aligned and hence the gamma rays emitted in their decay have pronounced angular distributions.

The reason for the strong alignment can be easily understood. The incoming particle brings orbital angular momentum into the compound system in the m = 0 substate only, taking the beam direction as the quantization axis. When the projectiles are heavy ions the average orbital angular momentum brought into the system is very large, in the range of 20-100 units. These values greatly exceed the spins of target and projectile. Consequently the compound nuclei are strongly aligned, with their angular momentum vectors lying nearly in the plane perpendicular to the beam direction. The evaporation of several neutrons, each of which can carry away only one or two units of angular momentum will leave the initial spin distribution almost unchanged. Thus the final distribution will be very strongly peaked around the m = 0 substate. The effect is illustrated in the vector picture. It can be seen that the projections on the Z axis of the individual neutron angular momentum vectors will be randomly distributed and tend to cancel.

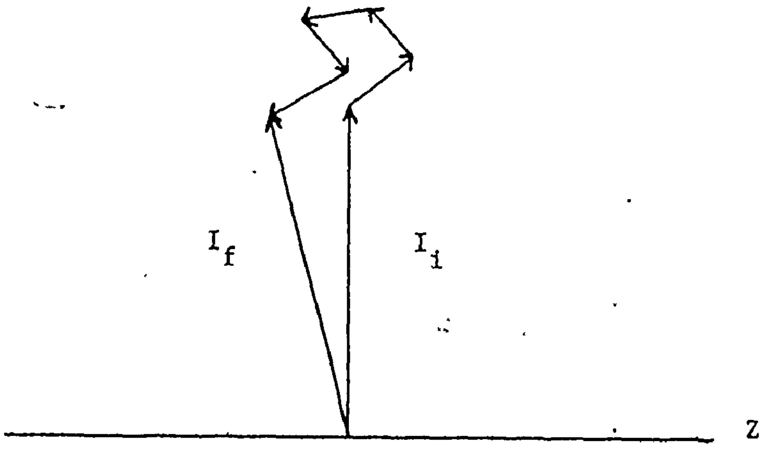

The angular distribution $W(\theta)$ is symmetric about 90° (with respect to the beam axis) and may be expressed in the form:

$$W(\theta) = 1 + \alpha_2 A_2' P_2 (\cos\theta) + \alpha_4 A_4' P_4 (\cos\theta).$$

In this expression $P_{2N}(\cos\theta)$ are Legendre polynomials, and A_{2N}' are the appropriate coefficients for the Legendre polynomials based on the assumption of complete alignment. The α_{2N} are coefficients which express the attenuation of the A_{2N}' coefficients for reasons of geometry or departures of the population parameters from perfect alignment. Experimentally, one can only determine the products $\alpha_2 A_2'$ and $\alpha_4 A_4'$ which in future will be referred to simply as A_2 and A_4.

In extreme cases (i.e. when the decaying state is highly aligned) the function $W(\theta)$ may change by a factor of 4 as θ is varied. Factors from 1 to 1.5 are much more common. The possible values of A_2' and A_4' for transitions between many combinations of spin values have been tabulated by Yamazaki (1967). It is possible to make reasonable assumptions about the population parameters of the initial state and thus to predict the angular distribution to be expected for various spin sequences. Since these may not differ significantly it is not generally possible to arrive at unique spin assignments from angular distributions alone.

Finally, angular distribution measurements can not distinguish between electric and magnetic transitions of the same multipole order. This is a serious limitation because, for example, E1 transitions connect states of opposite parity while M1 transitions connect states of the same parity. Nevertheless, it is a powerful method for limiting the spin options for the states involved. Much of the ambiguity resulting from angular distribution measurements can be removed by measuring the internal conversion coefficient of the transition.

Chapter 3

THEORY

3.1 Introduction

The interactions among nucleons are extremely complicated, and an exact solution of the equations describing their relative motions is impossible. Instead one is forced to create a simple physical system, a model, which incorporates the major features of the real system. Physical quantities are calculated, using the model, for comparison with measured values. In the course of this comparison refinements are added as embellishments to the model to improve the agreement between theory and experiment.

3.2 A Brief Survey of Nuclear Models

3.2.1 Shell Model

The earliest successful model for the interpretation of nuclear structure was the shell model (Mayer and Jensen(1955)) which borrowed heavily from the atomic shell model. This model treats each nucleon as if it were moving independently in a quantized orbit in a common average potential. Using a central potential it is possible to calculate the behaviour of spherical nuclei. The interaction between individual nucleons is considered to be a small perturbation on the interaction between a nucleon and the potential field. Despite its early accomplishments the theory needed the addition of a strong spin-orbit coupling term in the potential before it became effective.

This model makes it possible to predict correctly the total angular momentum, I, of nuclei in their ground states with a few exceptions and to make predictions about spins of low lying states. It is thus possible to assign values of the total angular momentum, I, to nuclear states for which this quantity has not been measured. Such assignments are very useful in the study of β-decay where the probability of β-decay depends on the difference between the total angular momentum of the initial and final nuclei. The theoretical predictions with regard to the allowed or forbidden nature of many β-decay processes , based on shell model assignments, agree well with experimental results.

The model accounts for the discontinuity in various nuclear properties at the so called "magic numbers" of nucleons. This is related to the closing of various proton or neutron shells of nucleons at the magic numbers of 2, 8, 20, 50, 82,and 126 particles. At these values the binding energy of the last nucleon is found to be very large so that closed shell nuclei are exceptionally stable.

The shell model can be used to predict the location of long-lived (i.e. isomeric) excited states of nuclei. Isomerism occurs when neighbouring energy levels of a nucleus have a large difference in total angular momentum. In such a situation the transition between the states is highly forbidden and the upper state has a measurable lifetime. The shell model can predict that the conditions for isomerism should occur in the mass region below the magic numbers 50, 82 and 126 but not immediately above them. These predictions correspond to the well documented "islands of isomerism" found experimentally.

Experimental data on magnetic moments (μ) and electric quadrupole moments (Q) have also been interpreted with some success in terms of the nuclear shell model. For example, at the proton numbers 2, 8, 20, 50 and 82, the quadrupole moment is zero or small. When a new shell begins to form, the quadrupole moment is negative; as the number of protons increases in the unfilled shell, Q becomes positive and increases until it reaches a maximum when the shell is 2/3 filled; Q then decreases to zero at the magic proton numbers after which it becomes negative. This behaviour is in rough agreement with the predictions of shell theory.

For nuclei midway between shell closings the quadrupole moment is found to be much larger than predicted by the shell model. Since the magnitude of the quadrupole moment is a measure of the deviation of a nucleus from spherical shape, these large experimental values of Q strongly suggest that the shell models assumption of a spherical potential is not correct. The Nilsson model to be discussed in Section 3.2.4 is designed to meet this problem.

3.2.2 The Liquid Drop Model

There are several properties of nuclear forces which suggest that the nucleus may be likened to a drop of liquid.

One of these is the short range nature of the nuclear force. The implication of this characteristic is that a nucleon interacts only with its nearest neighbours.

Another property is the saturation of the nuclear force, which implies a repulsive core. Without this characteristic the nuclear density would continue to increase as one added more nucleons despite the short range nature of the force. The fact that the nuclear radius is proportional to $A^{1/3}$ indicates that the nuclear density is roughly constant in the nuclear interior and such behaviour requires a repulsive core.

The correct dependence of nuclear binding energies on the number of particles can be obtained if it is assumed that the forces between nucleons possess those properties which are characteristic of the behaviour of molecules in a drop of liquid.

The combination of classical concepts of electrostatic repulsion and surface tension with the analogy of the nucleus to a drop of incompressible fluid of very high density resulted in a semi-empirical formula for determining the mass or binding energy of a nucleus in its ground state. The formula involves a number of terms whose structures are based on theory and whose constants are derived from experimental data.

The formula has been used to calculate the mass values of approximately 5000 (A,Z)(mass number, charge number) values. It reproduces quite accurately the values for many nuclei and gives the main features of the dependence on A and Z. However it is less successful for very light nuclei where there are too few particles to be treated as a liquid drop with a continuous distribution of material.

3.2.3 The Statistical and Optical Models

In Chapter Two the reactions of concern to this thesis were described in terms of the compound nucleus concept. This derives from the statistical model for nuclear reactions. The statistical nature of the compound nucleus theory implies that its predictions are at best averages, and do not take into account the differences between specific nuclei. It is not surprising, therefore, that a more detailed model is needed for the description of nuclear reactions.

One of the most serious failures of the compound nucleus theory is its inability to account for the rapid fluctuations of total neutron cross sections with neutron energy. The statistical model assumes that the compound nucleus is formed immediately when the incident neutron reaches the nuclear surface. It predicts cross sections which should vary as $E^{-\frac{1}{2}}$ for low energies reaching an asymptotic value of $2\pi R^2$ for large energies, where R is the radius of the target nucleus. Although experimental results reproduce this general trend, the observed total cross sections show a more complicated behaviour which seems to point to a combination of single particle and compound nucleus properties. Large scale maxima which occur are similar to those predicted by the theory of a single particle moving in an attractive potential e.g. a square well, but such a potential does not permit absorption of the particle as required by the compound nucleus concept. These two ideas have been successfully combined in the optical model.

This model describes the behaviour of the incident particle in a potential well $-V_o(r)$ but allows for the possibility of compound nucleus formation by adding to the potential a negative imaginary term $-iV_1(r)$. This term produces an absorption of the incident particle within the nucleus and this absorption is to represent the formation of the compound nucleus. According to the optical model, compound nucleus formation does not occur "immediately" nor with complete certainty. If $V_o(r)$ and $V_1(r)$ are reasonably constant over the nucleus it is possible to define a "coalescence coefficient" which is the probability per unit length for the incident particle in nuclear matter to form the compound nucleus. In this picture, if an incident particle gets into the nucleus it is reflected back and forth before escaping or being absorbed. This theory accounts very well for the behaviour of neutron cross sections.

3.2.4 The Collective Model

There is a large body of experimental evidence that cannot readily be explained in terms of the behaviour of individual particles. One example is fission, the division of a nucleus into two fragments. This process can be described as the deformation of a drop of nuclear matter. Another example is the existence of nuclei (in the mass ranges $18<A<28$, $150<A<190$, and $A>224$) which possess rather large quadrupole moments. The quadrupole moment is a measure of the deformation of the nucleus from spherical shape. The dynamical description of such a system involves the collective motion of a large number of nucleons such as would occur in surface oscillations or elastic vibrations of a liquid drop.

The simplest type of collective motion is connected with rotations of a deformed nucleus. If the rotational motion is sufficiently slow, it will not affect the internal structure of the nucleus. According to classical physics, the rotational energy is given by:

$$E_{rot} = \tfrac{1}{2} I \omega^2 \qquad [3-1]$$

where ω is the angular velocity of the rotation and $\mathcal{I}$ is an effective moment of inertia. for the nucleus.

For even-even nuclei, quantization of the angular momentum leads to the result:

$$E_{rot} = \frac{\hbar^2}{2\mathcal{I}} . I(I+1) \qquad [3\text{-}2]$$

where I is the total angular momentum quantum number of the nucleus. In the case of spheroidal nuclei the deformation is symmetric with respect to reflection in the nuclear center. This condition restricts I to even values 0, 2, 4, 6... and the parity is even. This implies that I^{π} for the first excited state is 2+, for the second excited state 4+ and so on. The excitation energies of these states should be proportional to I(I+1) and the transitions between them form rotational bands which are common throughout the mass regions mentioned above. At the ends of these mass regions the nuclei become 'soft' against deformation and the observed energy intervals no longer agree with equation 3-2.

3.2.5 The Nilsson Model

The behaviour of an odd nucleon moving in a deformed potential is described by the Nilsson model. This model envisages the outer nucleons moving around a deformed core composed of the spherical closed shells plus all the nucleons outside.

manner analogous to that of the shell model the wave functions are constructed by filling the lowest available energy states in a self consistent deformed potential (Nilsson (1955)). The simple potential chosen by Nilsson (an axially symmetric oscillator with spin-orbit coupling) led to rather simple wave functions and calculable matrix elements. Since then a number of physically more realistic potentials have been suggested but all of these made calculations more difficult. Since the resulting wave functions were not significantly better than those obtained by Nilsson, the Nilsson potential is almost universally used.

The single particle Hamiltonian is of the following form:

$$H_p = H_o + H_\delta + C\underline{\ell s} + D\underline{\ell\ell} \qquad [3\text{-}3]$$

In this expression $H_o + H_\delta$ represents the spheroidal harmonic oscillator potential which has been split into two parts. One of these (H_o) is spherically symmetric, the other (H_δ) is a function of the deformation, δ. The $\underline{\ell s}$ term accounts for the spin-orbit coupling already used in the shell model. The $\underline{\ell\ell}$ term is included to reduce the excitation of high angular momentum states, in agreement with observation.

Equation [3-3] can be expressed more explicitly as:

$$H_p = \frac{p^2}{2m} + \frac{m}{2}\left[\omega_\perp^2(x^2+y^2) + \omega_z^2 Z^2\right] - \kappa\hbar\omega_o(2\underline{\ell s} + \mu\ell^2) \qquad [3\text{-}4]$$

for the case of cylindrical symmetry.

In this expression the symbol ω represents an oscillation frequency. Those which appear in [3-4] are defined as:

$$\omega_{\perp}^{2} = \omega_{o}^{2}(\delta)\ [1 + \frac{2\delta}{3}] \qquad [3\text{-}5]$$

$$\omega_{z}^{2} = \omega_{o}^{2}(\delta)\ [1 - \frac{4\delta}{3}] \qquad [3\text{-}6]$$

where

$$\omega_{o}(\delta) = \omega_{oo}(1 - \frac{4\delta^{2}}{3} - \frac{16\delta^{3}}{27})^{-1/6} \text{ and}$$

$$\hbar\,\omega_{oo} = \hbar\,\omega_{o}(\delta = 0) \sim 41A^{-1/3}\text{MeV}$$

The parameter, δ, is approximately the ratio of the difference between the major and minor axes of the ellipsoid to the mean diameter (i.e. $\delta \sim \frac{\Delta R}{R_{o}}$). For the rare earth nuclei, δ, is positive indicating a prolate deformation (i.e. stretched along the symmetry axis or cigar shaped).

The constants κ and μ are adjusted to reproduce the sequence of shell model states already established in the Shell Model. Hence the Nilsson model reduces to the shell model at zero deformation.

As a result of the lack of spherical symmetry the total angular momentum of a particle orbiting the deformed core is not conserved. However the projection of the single particle total angular momentum on the symmetry axis, Ω, is a good quantum number.

The wave functions may be constructed as linear combinations of the basis vectors $|N\ell\Lambda\Sigma\rangle$. N is the appropriate harmonic oscillator shell and the other symbols are defined in Figure 3-1. This yields single particle wave functions of the form:

$$\chi_\Omega = \sum_{\ell\Lambda\Sigma} a^\Omega_{\ell\Lambda\Sigma} |N\ell\Lambda\Sigma\rangle \qquad [3\text{-}7]$$

Alternatively they may be expressed in terms of the spherical harmonic oscillator basis vectors $|N\ell j\Omega\rangle$ as:

$$\chi_\Omega = \sum_{j\ell} C^\Omega_{j\ell} |N\ell j\Omega\rangle \qquad [3\text{-}8]$$

The coefficients in each representation are related by an appropriate transformation.

In Figure 3-2 some results, for neutron states, of Nilsson model calculations are presented. At zero deformation the states are (2j + 1) fold degenerate shell model orbitals. As the deformation increases each shell model state splits into (j + ½) orbitals, each of which contains two nucleons. There is one such orbital for each value of Ω. For $\delta>0$ the low Ω states are depressed in energy while the high Ω states are raised. The converse is true for $\delta<0$. Each level can accommodate two particles corresponding to the projections $\pm\,\Omega$ of j on the symmetry axis. Similar diagrams are produced for protons although there is a slight rearrangement of the orbitals due to the Coulomb energy.

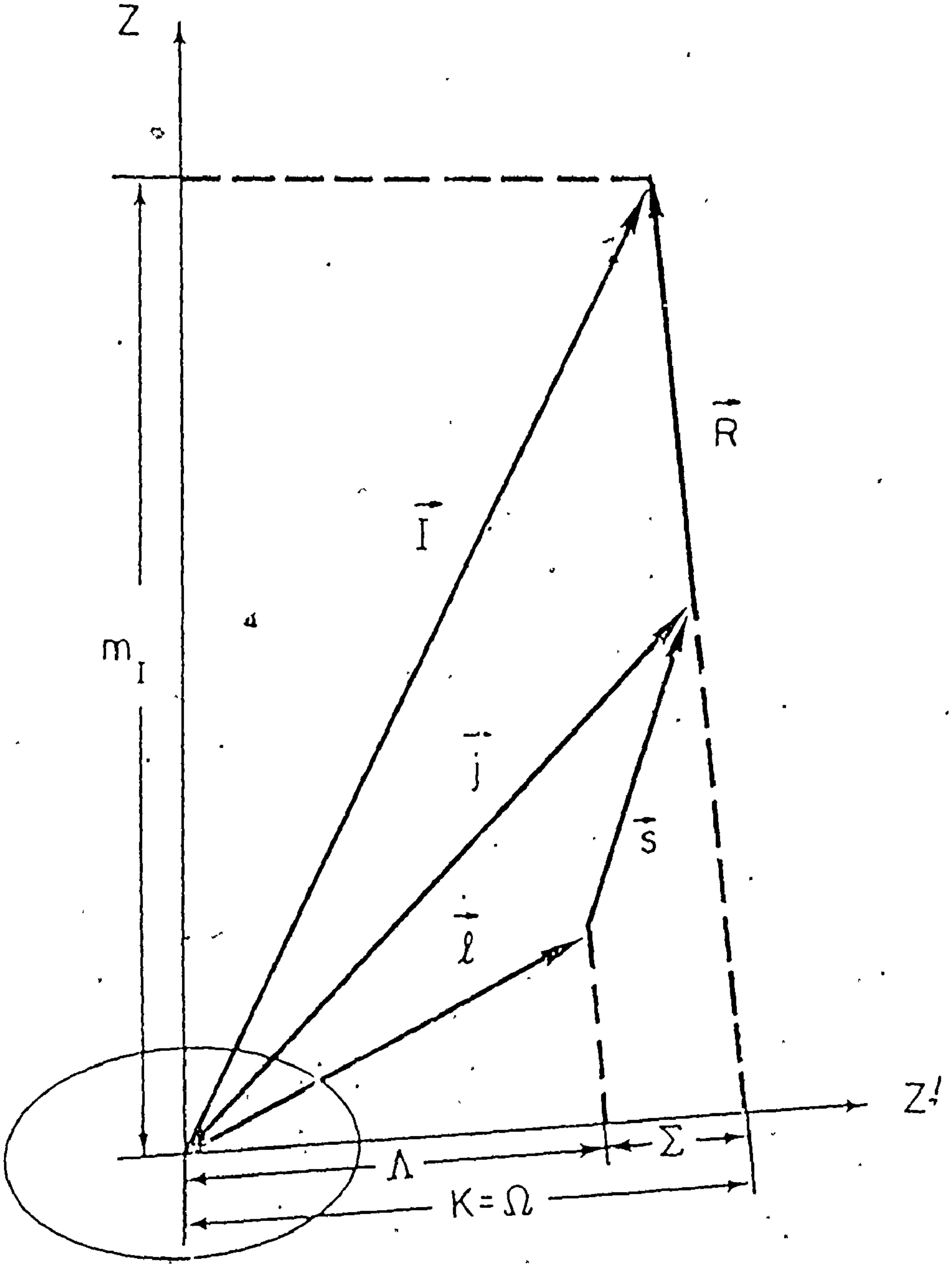

Figure 3-1

Angular momentum vector diagram for a deformed rotating nucleus.

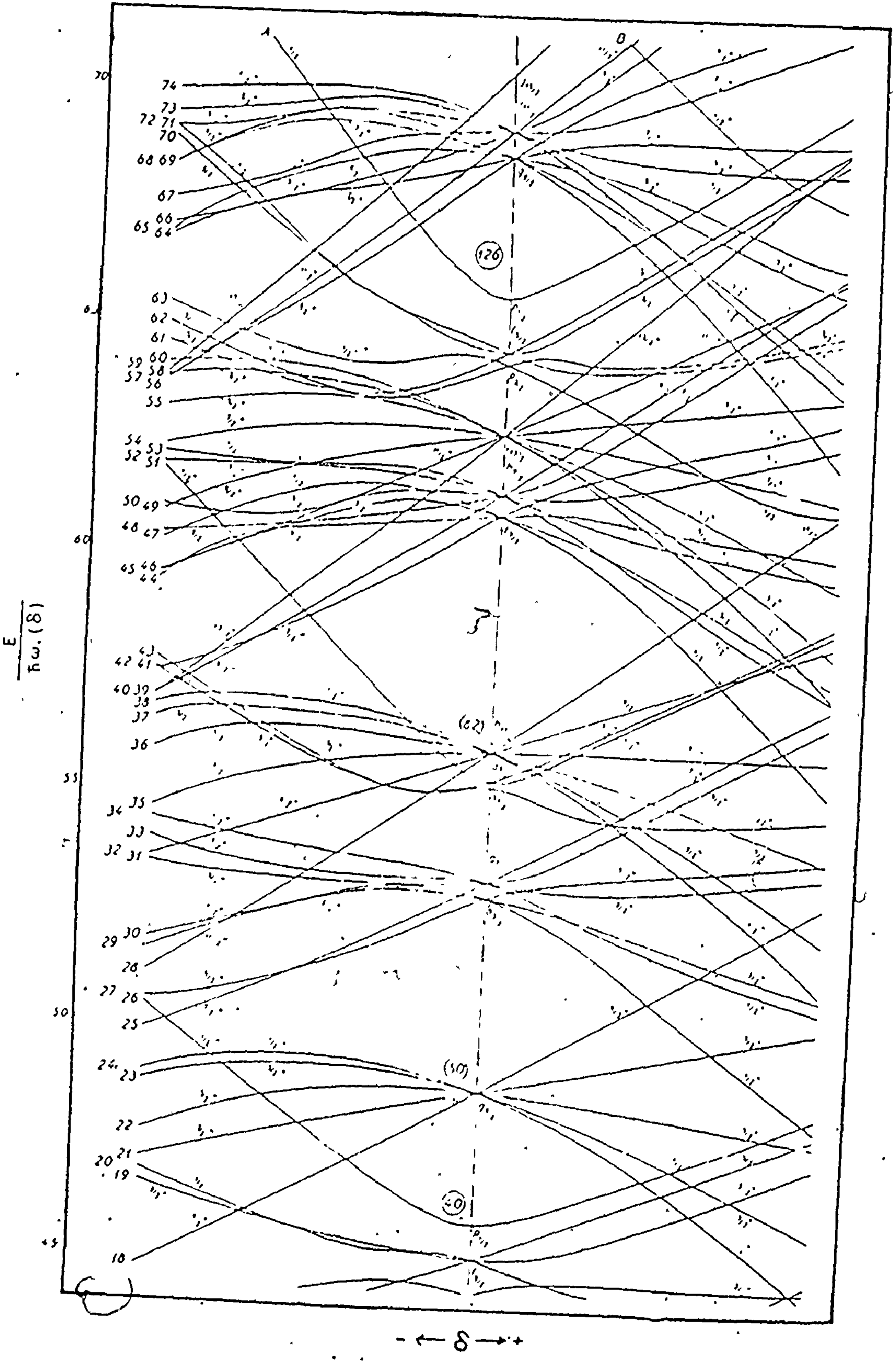

Figure 3-2

The Nilsson diagram for neutron states with neutron numbers between 40 and 126 showing the behaviour of the states as a function of deformation. (Reproduced from Nilsson,1955)

Figure 3-3 shows an expanded view of the region of interest in this study. The states are labelled as $\Omega\Pi[N,n_z,\Lambda]$ where N is the oscillator shell, n_z is the number of oscillator quanta along the z axis, Λ is the projection of ℓ on the symmetry axis, Ω is the projection of j on the symmetry axis and Π is the parity of the state, equal to $(-)^N$. The symbols inside the bracket which identify the state are called the asymptotic quantum numbers since they are constants of the motion only for large deformations.

3.2.6 The Unified Model

The concepts of the single particle moving in a deformed potential and the collective motion of the core particles are brought together in the Unified Model. The motion of the single particle is coupled to the rotational motion of the core as indicated in Figure 3-1 where R̲ represents the core's rotational angular momentum.

The Shroedinger equation for this system is of the form

$$H\psi = (T_{rot} + \sum_p H_p)\psi = E\psi \qquad [3\text{-}9]$$

where the summation p is over all particles outside the core.

The wave equation is a separable function of the form

$$\psi = \chi_{particle}\ \phi_{vib}\ \nu_{rot}$$

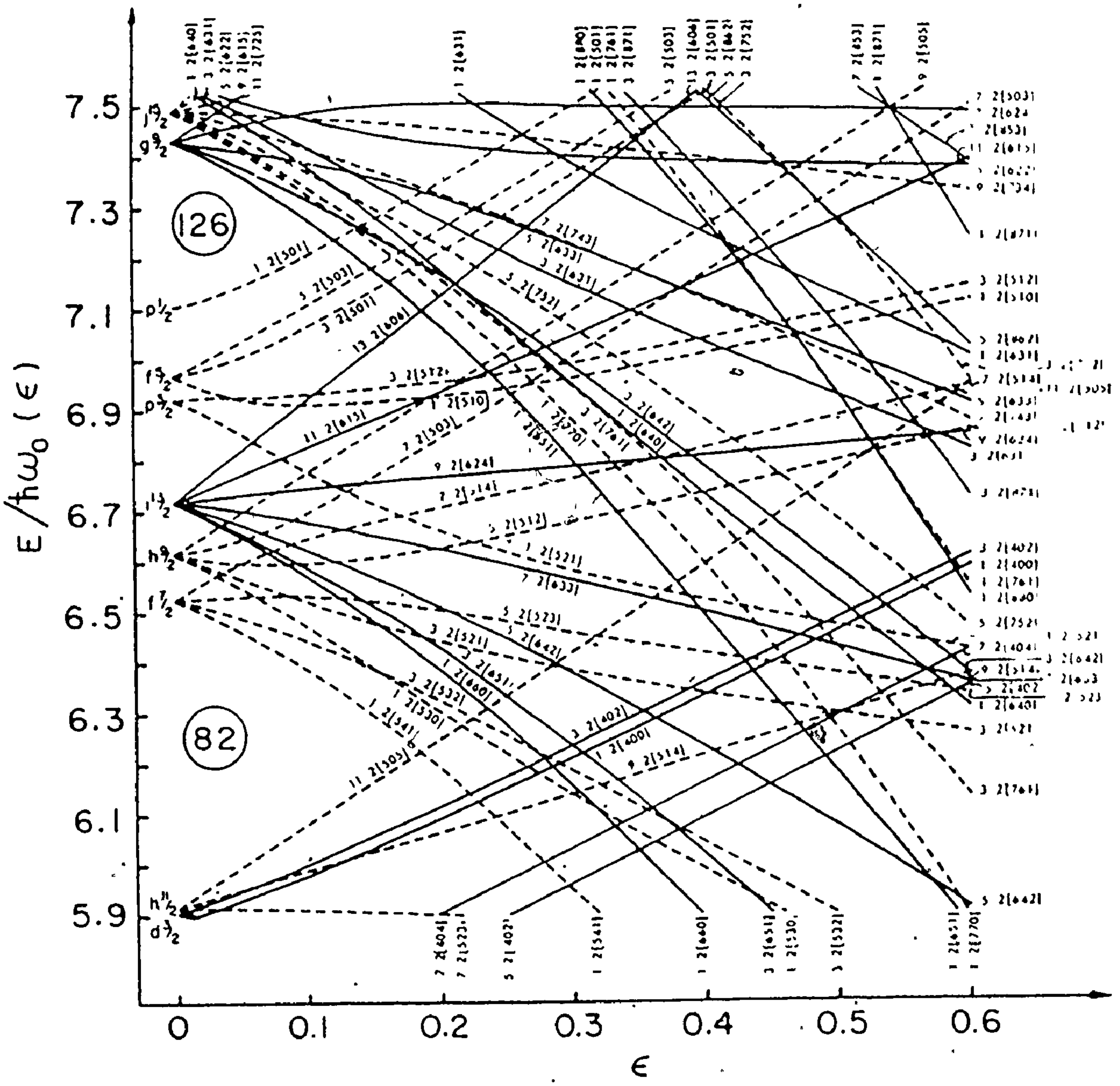

Figure 3-3

Nilsson diagram for neutron states, with neutron numbers between 82 and 126. (Note: In this diagram the deformation parameter $\epsilon = \delta + \frac{1}{6}\delta^2 + \ldots$, where δ is defined in the text.)

(Reproduced from Lederer et al 1968)

implying that the intrinsic motion of the nucleons is generally independent of the collective motion. The total Hamiltonian can then be written as a sum of Hamiltonians, each representing the various motions but including a small term, H_{coup}, so that the Rotation-Particle coupling (RPC) is not lost. Hence,

$$H = H_{rot} + H_{int} + H_{vib} + H_{coup}$$

The wave functions ν_{rot} are the standard rotation matrices $D^{I}_{M,K}$. The various symmetries of the spheroid require that the total wave function be expressed as:

$$|IMK\Omega\rangle = \sqrt{\frac{2I+1}{16\pi^2}}\, \phi_{vib}[\chi_{\Omega} D^{I}_{MK} + (-)^{I-j} \chi_{-\Omega} D^{I}_{M-K}]$$

Using these wave functions to solve the Shroedinger equation 3-9 one obtains the following expression for the rotational kinetic energy:

$$T_{rot} = \sum_{i=1}^{3} \frac{\hbar^2}{2\mathcal{I}_i} \langle R_i{}^2\rangle = \sum_{i=1}^{3} \frac{\hbar^2}{2\mathcal{I}_i} \langle (I_i - j_i)^2\rangle \qquad [3\text{-}10]$$

where the indices i refer to the body fixed axes. For the case of axial symmetry where $\mathcal{I}_1 = \mathcal{I}_2 = \mathcal{I}$ we may rewrite equation 3-10 as:

$$\langle T_{rot}\rangle = \frac{\hbar^2}{2\mathcal{I}} [\langle(\underline{I} - \underline{j})^2\rangle - (I_3 - j_3)^2] + \frac{\hbar^2}{2\mathcal{I}_3} (I_3 - j_3)^2$$

$$= \frac{\hbar^2}{2\mathcal{I}}[I(I+1) + \langle j^2\rangle - 2\langle \underline{I}\cdot\underline{j}\rangle - (K-\Omega)^2] + \frac{\hbar}{2\mathcal{I}_3} (K-\Omega)^2 \qquad [3\text{-}11]$$

Using the relation:

$$\underline{I}\cdot\underline{j} = I_3 j_3 + I_2 j_2 + I_1 j_1 = K\Omega + (I_+ j_- + I_- j_+)/2 \qquad [3\text{-}12]$$

we may finally write equation 3-10 as:

$$T_{rot} = \frac{\hbar^2}{2\mathcal{I}}[I(I+1) - K^2 - \Omega^2] + \frac{\hbar^2}{2\mathcal{I}_3}(K-\Omega)^2 - \frac{\hbar^2}{2\mathcal{I}}(I_+ j_- + I_- j_+) + \frac{\hbar^2}{2\mathcal{I}}\langle j^2\rangle . \qquad [3\text{-}13]$$

The fourth term involves only the particle motion and is usually included in H_{int}. The first two terms contain the diagonal contributions to the rotational energy. The remaining term expresses the coupling of the particle motion and the rotational motion of the core.

The only non-zero off-diagonal matrix elements are those between states which differ in K value by ±1. H_{coup} has a diagonal contribution only if $K = \frac{1}{2}$, in which case the rotational energy has the explicit form:

$$T_{rot} = \frac{\hbar^2}{2\mathcal{I}}[I(I+1) - K^2 - \Omega^2 + \langle \underline{j}^2\rangle] + \frac{\hbar^2}{2\mathcal{I}_3}(K-\Omega)^2 + \frac{\hbar^2}{2\mathcal{I}}[\delta_{K\frac{1}{2}}\, a(-1)^{I+\frac{1}{2}}(I+\tfrac{1}{2})]$$

where 'a', the decoupling parameter is given by:

$$a = -\Sigma(-1)^{j+\frac{1}{2}}(j+\tfrac{1}{2})|c_{j\frac{1}{2}}|^2$$

The coefficients $c_{j,\frac{1}{2}}$ are defined in equation 3-8.

For the states of interest to this study the decoupling parameter is shown as a function of deformation in Figure 3-4. The figure shows that the positive parity states have a large decoupling parameter at all deformations while the negative parity states will have a small decoupling parameter at large deformations and a large decoupling parameter at small deformations.

3.2.7 Residual Interactions

Even the unified model has shortcomings and the term 'Residual Interactions' is used to describe nuclear effects which cannot be described by means of the average field approach to nucleon interactions.

Residual interactions are separated into two classes: short range and long range. Thus the intrinsic Hamiltonian H_{int} may be written as:

$$H_{int} = H_{avg} + H_{short} + H_{long} \qquad [3\text{-}14]$$

The short range interaction is modelled as a pairing force to account for the fact that nucleons prefer to exist as correlated pairs which continuously scatter from one orbit to another. A mathematical description of this interaction was obtained as an adaptation of the theory of super-conductivity (Bardeen, Cooper,

Figure 3-4

The decoupling parameter 'a' as a function of deformation for the $1/2^+[660]$, $1/2^-[530]$ and $1/2^-[541]$ orbitals which originate in the $i_{13/2}$, $f_{7/2}$ and $h_{9/2}$ shell model states respectively.

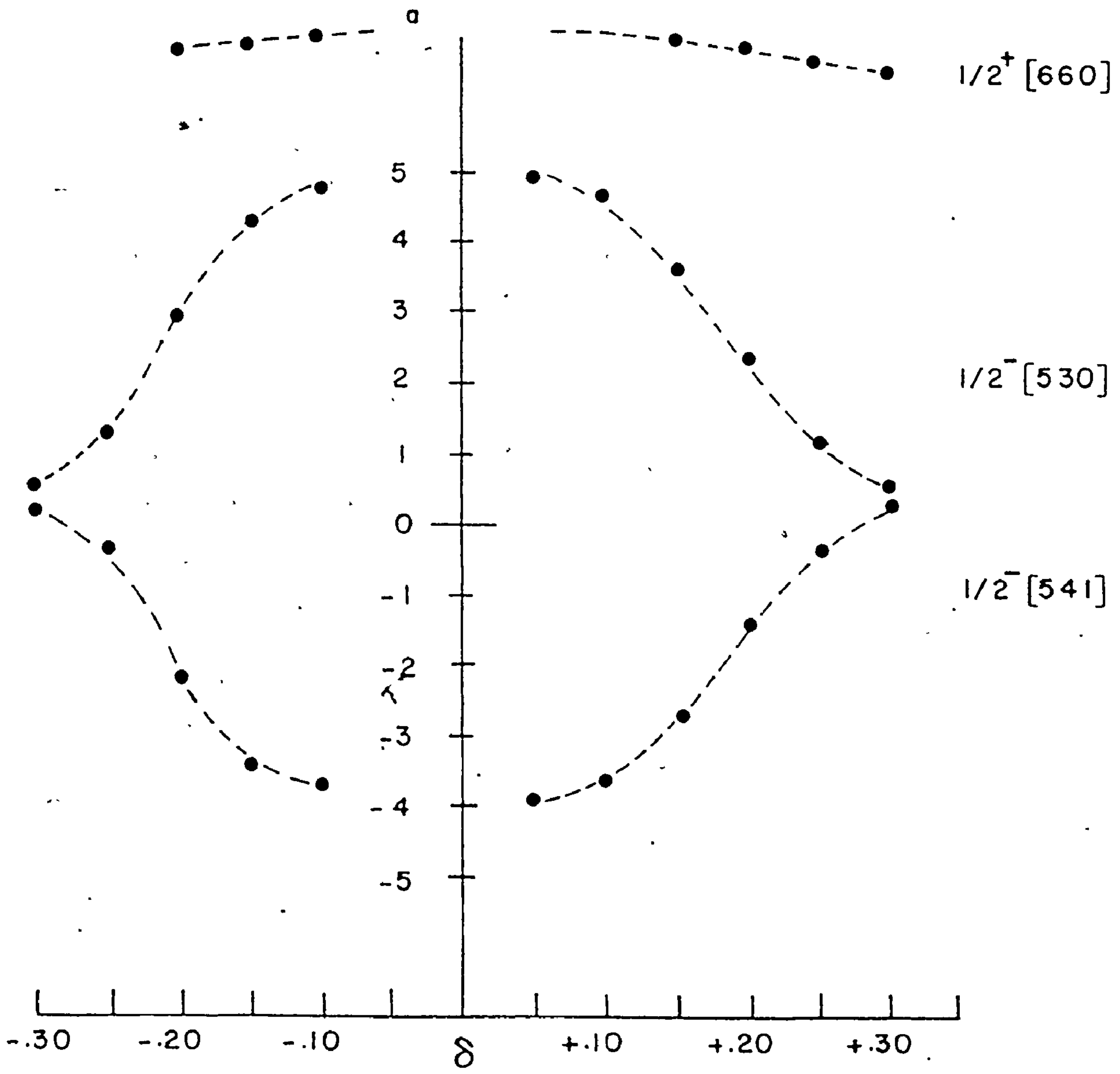

Figure 3-4

Schreiffer (1957)). Some of the important consequences of this description will be presented since they are incorporated in the calculations performed for this study.

The deepest lying states in an even-even nucleus are filled with nucleons which pairwise occupy the Ω degenerate orbitals. Near the Fermi level, however, the orbitals are only partially filled so that the Fermi surface is diffuse. Each level 'i' has a probability V_i^2 of being filled by a pair of nucleons, and a probability U_i^2 of being empty, hence:

$$U_i^2 + V_i^2 = 1.$$

In an odd nucleus, the extra nucleon occupies a definite level 'i'. This nucleon has the properties of a particle to the extent U_i^2 that the level was empty in the even-even nucleus and the properties of a hole to the extent V_i^2 that the level 'i' was filled in the even-even nucleus. This dual nature gives rise to the concept of a 'quasi-particle'. Consequently single particle excitations in an odd 'A' nucleus must be treated as quasi-particle excitations. When the excitations are far above the Fermi level the state becomes 'particle-like', for excitations far below the Fermi surface the state becomes 'hole-like'.

The observed intrinsic excitation in an odd 'A' nucleus is the difference between the ground state quasi-particle energy and the excited state quasi-particle energy.

The ground state quasi-particle energy is given by:

$$E_i = \sqrt{(\varepsilon_i-\lambda)^2 + \Delta^2} \qquad [3\text{-}15]$$

where ε_i is the Nilsson single particle energy, λ is the Fermi energy and 2Δ is the energy gap.

The quasi-particle excitation energy for level j is given by:

$$E_{exc.} = \sqrt{(\varepsilon_j-\lambda)^2 + \Delta^2} - \sqrt{(\varepsilon_i-\lambda)^2 + \Delta^2} . \qquad [3\text{-}16]$$

Usually $(\varepsilon_i -\lambda)$ is $<<\Delta$ and hence:

$$E_{exc.} = \sqrt{(\varepsilon_j -\lambda)^2 + \Delta^2} - \Delta . \qquad [3\text{-}17]$$

The general effect of pairing is to compress the levels near the ground state. The high lying states are lowered in energy by approximately Δ.

The gap parameter Δ, whose magnitude is determined by the strength of the pairing force, also provides a measure of the diffuseness of the Fermi surface. The gap parameter may be determined empirically from nucleon separation energies, S. Since in an odd'A' nucleus the odd nucleon has more energy, Δ, than if it were paired, it requires 2 Δ more energy to remove a nucleon from an even-even nucleus than from an odd-even nucleus.

The neutron gap is given by

$$\Delta_N = \frac{1}{4}\,[2S(Z,N) - S(Z,N+1) - S(Z,N-1)]. \qquad [3\text{-}18]$$

S(Z,N) refers to the separation energy in the even-even system. Energy gaps are typically of the order 700-900 keV in the rare earth region.

The quantities V_i^2 and U_i^2 referred to above are given by

$$V_i^2 = \frac{1}{2}\left[1 - \frac{\varepsilon_i-\lambda}{\sqrt{(\varepsilon_i-\lambda)^2+\Delta^2}}\right]$$

$$U_i^2 = \frac{1}{2}\left[1 + \frac{\varepsilon_i-\lambda}{\sqrt{(\varepsilon_i-\lambda)^2+\Delta^2}}\right]$$

The Nilsson model plus the residual interactions thus described provides a much more realistic prediction of transfer reaction cross sections, beta transition rates and gamma transition probabilities than is possible without pairing. This effect may be taken into account by a multiplicative pairing factor P_γ, such that

$$T_\gamma(i \rightarrow f) = P_\gamma\, T_{\gamma\ \text{single-particle}}$$

P_γ is defined as follows:

$P_\gamma \sim [U_iU_f \pm V_iV_f]^2$ where there is no change in the number of quasi-particles or

$P_\gamma \sim [U_iV_f \mp U_fV_i]^2$ where the number of quasi-particles changes by two. The upper sign is used for magnetic multipole transitions and the lower sign for electric multipole transitions.

Consequently for transitions between single quasi-particle states near the Fermi surface the electric transition rate may be reduced by two or three orders of magnitude below the Nilsson model estimates (Vergnes, Rasmussen (1965)), whereas the magnetic transition rates are only slightly affected.

The long range residual interaction is usually presented as a multipole - multipole expansion, each term of which may be written in the form

$$H = -\sum_{m} \sum_{a>b} k_{lm} (-)^{m} Q^{a}_{lm} \; Q^{b}_{lm} \qquad [3\text{-}19]$$

where

$$Q^{a}_{lm} = r_{a}^{\,l} \; Y_{lm} (\theta_{a} \; \phi_{a}) \; .$$

The single particles are represented by a and b, $k_{l,m}$ represents the strength of the force. Whereas the pairing force connects only pairs of nucleons in time reversed orbitals, the long range multipole-multipole force affects all pair combinations, with the nucleon pairs all acting coherently. The multipole - multipole force is, therefore, essential for a description of collective phenomena.

3.2.8 Rotation - Particle Coupling Effects and the Decoupled Band in Odd Mass Nuclei

In the light of recent theoretical developments (Stephens, Diamond and Nilsson (1973)), (Stephens (1975)) and the present experiments, it is pertinent to discuss Rotation - Particle Coupling in more detail.

The RPC (Coriolis) effects are not common in everyday experience and hence it is difficult to gain an intuitive grasp of this type of force.

One of the few common examples is the precession of a spinning top resulting from the interaction of the downward force of gravity and the angular momentum vector of the top. Another example which bears a closer relationship to the nuclear effect is the tendency of a gyroscope to align its axis with that of the earth when it is kept in a plane parallel to the earth's surface. This is clearly analogous to the interaction of the angular momentum vector of an orbiting nucleon and the rotation vector of a deformed nucleus.

The rigorous expression of the Coriolis energy is given by the fourth term in equation 3-13

$$E_{cor} = \frac{\hbar^2}{2I}\left(I_+ j_- + I_- j_+\right) \sim \frac{2\hbar^2}{2I}\, I.j \qquad [3\text{-}20]$$

It is simple to see from this expression that for rare earth nuclei, where the j = 11/2, 13/2 etc. orbitals are being populated and the rotation parameter ($\hbar^2/2I$) is 10 - 20 keV, that this term can be of the order of 0.5 MeV for moderate spin values of the core. Hence one may expect significant distortions of rotational band patterns. Nilsson (1955) derived the following result:

$$H_p = e'_j + k\beta \cdot \frac{3\Omega^2 - j(j+1)}{4j(j+1)} = e_j + C\,\Omega^2 \qquad [3\text{-}21]$$

where e'_j is the Nilsson single particle energy and e_j is this energy plus constants from the other term. In this model one assumes that j is a good quantum number and that the single particle Hamiltonian, Hp, is associated with a quadrupole field oriented along the symmetry axis.

Using equation 3-21, equation 3-13 becomes

$$T_{rot} = e_j + A\left[I(I+1) + j.(j+1)\right] + \left[C - 2A\right]\Omega^2 + H_c \qquad [3\text{-}22]$$

where $H_c = -A[I_+ j_- + I_+ j_-]$ [3.23]

and $A = h^2/2I$ is the rotation parameter.

For a given set of conditions (I,j,β) the first two terms of equation 3-22 are diagonal and the problem reduces to diagonalizing the last two terms. If H_c is negligible then the solutions are eigenfunctions of the Ω^2 term only which are obviously states with sharp Ω values. This situation represents the normal, strong, or deformation aligned coupling scheme shown vectorially below

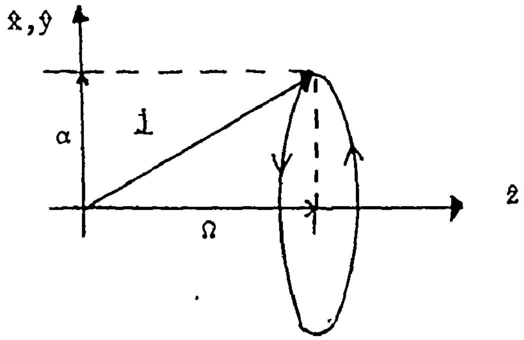

The vector $\underline{\alpha}$, the projection of $\underline{j}$ on the rotation axis is obviously not a good quantum number. However C and A are not functions of I whereas H_c increases with I. Therefore, one might expect that for sufficiently large I, the Ω^2 term will be negligible compared with H_c and the solutions will be eigenfunctions of H_c.

Stephens, Diamond and Nilsson (1973) showed that this situation can be described in terms of a new coupling scheme which they called rotation aligned coupling. This is represented vectorially below

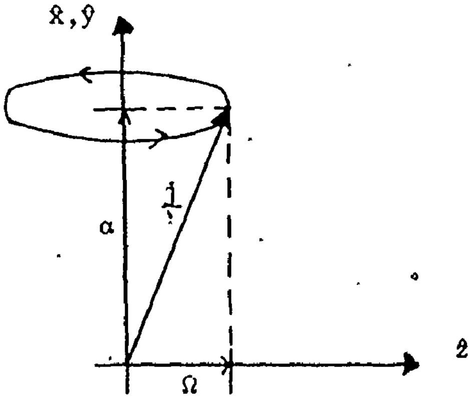

where α is now a good quantum number as $\underline{j}$ precesses around the rotation axis and Ω is not a good quantum number. This is to be contrasted with the normal interpretation of this situation below

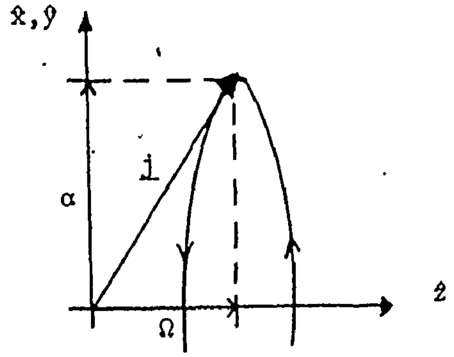

Assuming that the changeover to the rotation aligned coupling scheme does in fact take place, Stephens et al have derived some of the consequences.

They claim that the rotation aligned scheme is applicable even for low spin states when (C-2A), the coefficient of Ω^2 approaches zero. The rotation parameter A is always positive hence this occurs when C is positive which implies a prolate deformation in the one-particle Hamiltonian, 3-21. The one-hole Hamiltonian is obtained by reversing the sign of k in equation 3-21, hence cancellation occurs for oblate deformation.

When cancellation occurs, the eigenfunctions of T_{rot} are those of H_c and approximate wave functions are linear combinations of the single particle wave functions in the normal, strong coupling scheme, i.e.,

$$\psi^{I_j}_{M\alpha} = \sum_{\Omega} d^{j}_{\alpha\Omega}(\pi/2)\, \chi^{j}_{\Omega}\, D^{I}_{M\Omega}$$

where d is a rotation matrix and α is the projection of $\underline{j}$ on the rotation axis. Stephens et al originally derived the eigenvalues of H_c to be $-2I A\alpha$. However, they arbitrarily 'improve' them by substituting (I+1/2) for I. Hence we have

$$E_o(I,j,\alpha) = e_j + A\,[(I-\alpha)(I-\alpha+1) + j(j+1) - \alpha^2] \qquad [3\text{-}24]$$

By invoking symmetry and the restriction that $I \geq j$ they show one obtains a rotational band with $\alpha = j$ and spins $I = j, j+2, j+4$ .. etc. These states have the energy spacing of the core. The other spin members $j+1, j+3$ etc., the 'unfavoured' members, occur at much higher excitation energies. The collection of 'favoured' states they refer to as the Decoupled Band.

Superficially the energies of the states in the odd A bands look as if the ground state band of the even - even core had simply been superimposed on the odd mass bandhead state without major changes in the configuration of the particle or core states. In the extreme case the particle is effectively decoupled from the core and becomes essentially a spectator to the motion of the core. Thus the model is incapable of predicting states of spin $I < |R+j|$. However through the 'new' quantum number α which effectively modifies the rotation parameter according to the spin of each state, the model achieves some of the observed compression of the higher spin states thereby demonstrating somewhat better agreement between the observed and calculated energy spacings than the Nilsson calculations employing a rigid rotor (constant A) formulation.

3.2.9 The Asymmetric Rotor Model

Most calculations relating to the energy levels of deformed nuclei assume that the deformation possesses axial symmetry resulting in either the oblate or prolate spheroidal shape.

Davydov and Filipov (1958) have calculated the energy states and the electric and magnetic transition probabilities for rotational levels of even nuclei which do not possess axial symmetry. They consider the energy states of an even nucleus corresponding to rotation of the nucleus as a whole with no change of its internal state, and write the following operator for the rotational energy of the nucleus

$$H = \sum_{i=1}^{3} \frac{\hbar^2}{2\mathcal{I}_i} R_i^2 = \sum_{i=1}^{3} \frac{A R_j^2}{2 \sin^2 (\gamma - \frac{2\pi}{3} . i)}$$

where the explicit forms of the effective moments of inertia, I_i, have been substituted and the various constants collected into the constant A, which has the dimension of energy, and γ gives the deviation of the shape of the nucleus from axial symmetry and has values between 0 and $\pi/3$.

This simple model was extended to odd mass nuclei by Hecht and Satchler (1962). A single nucleon was coupled to an inert core of well stabilized asymmetric equilibrium shape. The state of the odd nucleon is described by single particle wave functions such as those calculated by Newton (1960) which were generalizations for the asymmetric case of the wave functions computed by Nilsson for axially symmetric nuclei.

The rotational energy spectrum for a given particle excitation is in general very rich in the number of levels and may consist of a complicated sequence of spin values. In many cases, however, particularly for small asymmetries, the rotational spectra may consist of several well separated sequences of spin states which resemble the rotational bands of axially symmetric nuclei, especially insofar as k (the projection of I on the body-fixed z-axis) may be approximately a good quantum number for each sequence.

In an initial survey of odd mass nuclei around A=190, Hecht and Satchler found no clear cut evidence for the existence of nuclei with a well defined asymmetric equilibrium shape. Their calculations showed that it would be difficult to distinguish between a symmetric and an asymmetric rotor model when the asymmetry is small. While observed energy level schemes could be reproduced by the model, electromagnetic transition rates could not.

In the intervening years experimental techniques have improved many fold and now yield data which is capable of providing more critical testing of the model. Recently Meyer ter Vehn et al (1974) have applied the model to levels in ^{187}Ir, ^{195}Au and ^{197}Tl. Their results indicate not only triaxial shapes but also show that the moments of inertia change like those of irrotational flow as the nucleus changes shape from oblate to prolate through a number of intermediate steps. Recently Khoo et al have shown that a similar set of states occur in ^{191}Pt.

3.2.10 The Variable Moment of Inertia Model

It has long been recognized (Bohr and Mottelson (1953) that the simple formula for the energy levels of a rotational band (equation 3-6) is inadequate, in most nuclei, for predicting the higher excitation states. Corrections of the form $B[\ I(I+1)\ ]^2$ as suggested by rotation-vibration coupling effects in molecules have been used to obtain the observed compression of the levels at high excitation energy. This resulted in an expression of the form

$$E_I = \varepsilon_k + AI(I+1) + B[\ I(I+1)\ ]^2 + C[\ I(I+1)\ ]^3 + \ldots$$

where ε_k is the excitation energy of the bandhead (Nathan and Nilsson (1965)). The fit to such a curve should improve with the addition of each successive term in the expansion but the parameters have little physical significance.

Recently 'stretching models' have been suggested by Mariscotti et al (1969), Scharff-Goldhaber and Goldhaber (1970) and Trainor and Gupta (1971) which lead to variable moments of inertia (VMI). This approach has more intuitive insight into the problem since it envisages a gradual stretching of the nucleus at higher rotational frequencies with a resultant increase in the moment of inertia and a reduction in the excitation energy required. The moments of inertia for each state can be determined by a variational procedure.

In the case of Mariscotti et al (1969) the following expression was found to give the best fit to experimental levels in an extensive survey of nuclear data of even - even nuclei:

$$E_I(\mathcal{I}) = C/2\ (\mathcal{I}-\mathcal{I}_0)^2 + \frac{I(I+1)}{2\mathcal{I}}$$

where $\mathcal{I}$ and $\mathcal{I}_0$ are the moments of inertia of the nucleus in state I and the ground state of the nucleus respectively.

The moment of inertia, $\mathcal{I}$, must be determined for each energy E_I by satisfying the variational condition

$$\frac{\partial E_I(\mathcal{I})}{\partial \mathcal{I}} = 0. \qquad [3\text{-}25]$$

This procedure results in a two parameter formula (C and $\mathcal{I}_o$) for the moments of inertia.

Volkov (1971) gave a theoretical foundation to this work which was extended by Gregory and Taylor (1972) to even - odd nuclei for cases where Coriolis mixing between bands generated by different odd particle valence states was not important.

Their modification of the model yielded the following expression for the excitation energies of the members of a rotational band built on a particle in state K:

$$E_I(\mathcal{I}) = C/_2 \, (\mathcal{I}-\mathcal{I}_K)^2 + \hbar^2/_{2\mathcal{I}} \, [I(I+1) - K(K+1)] \qquad [3\text{-}26]$$

where $\mathcal{I}$ and $\mathcal{I}_K$ represent the moments of inertia of the nucleus in state I and the bandhead state respectively. The first term of equation 3-26 expresses the increase in potential energy associated with increasing angular momentum and consequent stretching, while the second term is the usual rotational kinetic energy. This extension of the model was also subsequently justified theoretically by Volkov (1972).

Since the bandhead energy is defined by experiment, there remain only two adjustable parameters in this model, $\mathcal{I}_K$ and C to fit all the levels. Using equation 3-26 with the condition 3-25 the moment of inertia may be defined as a function of the spin of each level. The result is the following expression

$$\mathcal{I} = \mathcal{I}_K \left[1 - \frac{[I(I+1) - K(K+1)]\hbar^2}{2C\mathcal{I}^3}\right]^{-1} \qquad [3\text{-}27]$$

3.3 BAND MIXING

One of the effects of the Coriolis force is to cause a mixing of states. Below some effects are presented for a general case involving two orthogonal states ψa and ψb. A more detailed picture applicable to the case under study is presented in section 6.2.1.

The wave function of the mixed state may be written as

$$\psi = C_1\psi_a + C_2\psi_b \qquad [3\text{-}28]$$

where C_1 and C_2 are the mixing amplitudes, assumed to be normalized, i.e.

$$C_1^2 + C_2^2 = 1.$$

The Schroedinger equation may then be written as

$$H(C_1\psi_a+C_2\psi_b) = E(C_1\psi_a+C_2\psi_b). \qquad [3\text{-}29]$$

This yields the secular equations

$$\begin{aligned} C_1(E_a-E) + C_2H_{ab} &= 0 \\ C_1H_{ba} + (E_b-E)C_2 &= 0. \end{aligned} \qquad [3\text{-}30]$$

where H_{ab} represents the matrix element $<\psi_a|H|\psi_b>$, and E_a and E_b are the unperturbed energies. For non trivial solutions to exist, the determinant

$$\begin{vmatrix} (E_a-E) & H_{ab} \\ H_{ba} & (E_b-E) \end{vmatrix} = 0$$

or

$$E^2 - E(E_a+E_b) + E_aE_b - H_{ab}^2 = 0 \qquad [3\text{-}31]$$

assuming

$$H_{ab} = H_{ba}.$$

The solutions to 3-31 are:

$$E\pm = \frac{1}{2}\left\{(E_a+E_b) \pm (E_a-E_b)\left[1 + \left(\frac{2H_{ab}}{E_a-E_b}\right)^2\right]^{1/2}\right\} . \qquad [3\text{-}32]$$

If the notation is chosen such that $E_a > E_b$, then the + and − signs signify the higher and lower perturbed energies respectively. The ratio of the differences of the perturbed and unperturbed energies may be given by

$$\frac{E_+ - E_-}{E_a - E_b} = \left[1 + \left(\frac{2H_{ab}}{E_a-E_b}\right)^2\right]^{1/2} .$$

By substituting 3-32 into 3-30 the amplitudes C may be obtained

$$C_{1\pm} = \left[1 + \left(\frac{E_a-E_\pm}{H_{ab}}\right)^2\right]^{-1/2} .$$

and

$$C_{2\pm} = \left(\frac{E_\pm-E_a}{H_{ab}}\right)C_{1\pm}$$

and the corresponding eigenfunctions may be written as

$$\psi_\pm = C_{1\pm}\,\psi_a + C_{2\pm}\,\psi_b .$$

It may be simply shown that

$$C_{1+} = C_{2-}$$

and

$$C_{1-} = -C_{2+}$$

Hence the eigenfunctions may be written as

$$\psi_+ = C_{2-}\psi_a - C_{1-}\psi_b$$

$$\psi_- = C_{1-}\psi_a + C_{2-}\psi_b \quad .$$

The ratio of the amplitudes may be defined as

$$\alpha_I = \frac{C_{1-}}{C_{2-}} = -\frac{2H_{ab}}{E_a - E_b} \Big/ \{1 + \sqrt{1 + (\frac{2H_{ab}}{E_a - E_b})^2}\}$$

where any possible spin dependence is implicitly included.

The wave functions may be written in the form

$$\psi_u(I) = \psi_+ = \frac{1}{(1+\alpha_I^2)^{1/2}} [\psi_a - \alpha_I\psi_b]$$

$$\psi_\ell(I) = \psi_- = \frac{1}{(1+\alpha_I^2)^{1/2}} [\psi_b + \alpha_I\psi_a] \ ,$$

where $\psi_u(I)$ and $\psi_\ell(I)$ have been introduced to denote the upper and lower states respectively. With this notation the E2 and M1 transition matrix elements may be written as

$$Q_{u\ell}(I'I) = <\psi_u(I) \, |O(E2) \, | \, \psi_\ell(I) >$$

$$= \{ \alpha_I Q_{aa} - \alpha_{I'} Q_{bb} + Q_{ab} \ (1 - \alpha_I\alpha_{I'})\} / \sqrt{(1+\alpha_I^2) \ (1+\alpha_{I'}^2)}$$

and

$$M_{u\ell}(I'I) = <\psi_n(I') \, |O(M1)| \, \psi_\ell(J) > .$$

$$= \{ \alpha_I M_{aa} - \alpha_{I'} M_{bb} + M_{ab} \ (1 - \alpha_I\alpha_{I'})\} / \sqrt{(1+\alpha_I^2) \ (1+\alpha_{I'}^2)}$$

where Q and M are the E2 and M1 matrix elements respectively.

3.4 ELECTROMAGNETIC TRANSITION RATES

In this section only the selection rules that govern photon emission will be presented since the general theory of photon radiation may be found in many standard textbooks, e.g., Preston (1962).

Consider a system wherein a state characterized by spin and parity I_i and Π_i , $|I_i \pi_i>$, decays via emission of photon radiation to a state $|I_f \pi_f>$. The spin value of the photon, called the multipolarity λ, is such that

$$|I_i - I_f| \leq \lambda \leq I_i + I_f$$

and the parity of the photon is such that

$$\pi_i \pi_f = (-)^{\lambda} \quad \text{for an electric radiation}$$

$$(-)^{\lambda+1} \quad \text{for a magnetic radiation.}$$

The transition probability for emission of a photon of energy and angular momentum λ is given by

$$T(\lambda, I_i \rightarrow I_f) = \frac{8\pi(\lambda+1)}{\lambda[(2\lambda+1)!!]^2} \frac{1}{\hbar} \left(\frac{\omega}{c}\right)^{2\lambda+1} B(\lambda, I_i \rightarrow I_f) \text{ sec.}^{-1} \qquad [3\text{-}33]$$

where $B(\lambda, I_i \rightarrow I_f)$, the reduced transition probability is given by

$$B(\lambda, I_i \rightarrow I_f) = \sum_{\mu M_f} | < I_f M_f | O(\lambda,\mu) | I_i M_i > |^2 . \qquad [3\text{-}34]$$

$O(\lambda,\mu)$ is the μ-component of the electric or magnetic multipole transition operator of order λ .

For the first few values of λ , equation (3-33) gives the following decay rates

$$
\begin{aligned}
T(E1) &= 1.59 \times 10^{15} \ (E)^3 \ B(E1) \\
T(E2) &= 1.22 \times 10^{9} \ (E)^5 \ B(E2) \\
T(E3) &= 5.67 \times 10^{2} \ (E)^7 \ B(E3) \\
T(M1) &= 1.76 \times 10^{13} \ (E)^3 \ B(M1) \\
T(M2) &= 1.35 \times 10^{7} \ (E)^5 \ B(M2)
\end{aligned}
$$

where E is the photon energy in MeV, $B(E\lambda)$ is in units of $e^2 R^{2\lambda}$ and $B(M\lambda)$ in units of $(e\hbar/2Mc)^2 R^{2\lambda-2}$ (R is the nuclear radius given by $R = R_o A^{1/3}$, $R_o = 1.07$ f and $e\hbar/2Mc$ is the nuclear magneton, μ_N).

A crude estimate of the ratio of magnetic and electric transition rates of the same order resulting from these relations is $\sim 10^{-2}$. Similarly, the ratio of successive multipole orders λ and λ+1 (of the same type) is $\sim 10^{6}$. Thus, it is usually only the lowest multipole order which contributes to a given transition. One common exception to this rule occurs in cascade transitions within rotational bands in deformed nuclei, where enhanced E2 transitions compete with the otherwise faster M1 transitions.

The reduced transition probability defined in equation 3-34 can be evaluated explicitly in the unified model and may be written as a product of a geometrical factor, governed by angular momentum coupling rules and a factor depending only on the intrinsic wave functions of the initial and final states:

$$B(\lambda) = < I_i \lambda K_i \ K_i - K_f | I_f K_f >^2 < K_f | O(\lambda) | K_i >^2 \qquad [3\text{-}35]$$

where i and f refer to the initial and final states respectively. For transitions from the same initial state to two different final states in the same rotational band, the ratio of the reduced transition probabilities is given by

$$\frac{B(\lambda \ I_i K_i \rightarrow I_f K_f)}{B(\lambda \ I_i K_i \rightarrow I'_f, K'_f)} = \frac{< I_i \ \lambda \ K_i \ K_f - K_i | I_f K_f >^2}{< I_i \ \lambda \ K_i \ K'_f - K_i | I'_f, K'_f >^2} \qquad [3\text{-}36]$$

(Alaga et al (1955)).

Equations 3-35 and 3-36 are applicable for transitions between states for which K is a good quantum number.

The Clebsch-Gordan coefficients in the expression for the reduced transition probability 3-35 create a K selection rule.

$$\Delta K = K_i - K_f \leq \lambda . \qquad [3\text{-}37]$$

This rule is not strictly obeyed since transitions of reduced intensity can still occur because of small admixtures of other K values. However it should be obeyed by the main components of the wave functions. To the first order, transitions proceed through admixtures of the type $|K_i - K_f| = \lambda$ and branching ratios (for transitions from the same initial state) will follow the Bohr-Mottelson (1963) rule. Higher order corrections, taking into account admixtures of the type $|K_i - K_f| = \lambda - 1$ and $|K_i - K_f| = \lambda - 2$, have been derived by Mikhailov (1966). For these admixed cases the quantity υ defined by $\upsilon = |K_i - K_f| - \lambda$ where K_i and K_f refer to the main components of the wave functions, is referred to as the degree of K-forbiddenness.

It is also customary to define a retardation factor which is the ratio of the observed half life to that predicted by the Weisskopf (1952) single particle estimate (3-33) or sometimes the Nilsson model estimates i.e.,

$$F_W = T_{1/2}\,(\text{expt.})/T_{1/2}(\text{SP})$$

Using explicit forms of 3-35 it is possible to derive a comparison of crossover-to-cascade branching ratios in a rotational band which yields the mixing ratio, δ^2 in a cascade transition. The expression for an unmixed (only one K value) band is

$$\frac{1}{\delta^2} = \frac{T_\gamma'\,(M1)}{T_\gamma'\,(E2)} = \left[\frac{1}{\lambda}\left(\frac{E_\gamma}{E_\gamma'}\right)^5 \cdot \frac{(I+1)\;(I-1+K)\;(I-1-K)}{2K^2(2I-1)}\right] - 1 \qquad [3\text{-}38]$$

(Alexander, Boehm and Kankeleit (1964)), where

$$\lambda = \frac{T_{\gamma}(E2)}{[T\gamma'(E2) + T\gamma'(M1)]} \qquad [3\text{-}39]$$

and γ and γ' denote the crossover I → I-2 and cascade I → I-1 transitions respectively. According to the rotational model the quantity $(g_K - g_R)$ is a constant for all rotational states of an unperturbed band and is given by

$$[(g_K - g_R)/Q_o]^2 = \frac{8.71\text{x}10^{-1}\ E_{\gamma'}^{2}}{(I+1)\ (I-1)}\ \frac{1}{\delta^2} \qquad [3\text{-}40]$$

where Q_o is the intrinsic quadrupole moment in barns and $E_{\gamma'}$ is in MeV. The sign of $(g_K - g_R)$ is the same as that of δ which may be found from angular distribution measurements.

Chapter 4

EXPERIMENTAL TECHNIQUES

4.1 Introduction

This chapter will describe the apparatus and the techniques employed to obtain and analyse the data in these experiments. Since many of the items have been described in detail elsewhere only a brief account of each will be given.

4.2 The Beam Transport System

Negative helium ions are produced by a duoplasmatron ion source using a lithium adder gas. The ions are then extracted, focussed and accelerated to the high voltage terminal of the tandem Van de Graaff accelerator. The machine is capable of maintaining 9.3 megavolts for useful periods of time but is more comfortable at 8.3 megavolts. At the terminal the beam passes through a foil stripper, becomes doubly positively charged (He^{++}) and is thereby subjected to a further acceleration. This results in an equivalent charge state of three units giving the beam particles an energy of 3V eV, where V is the terminal voltage. On leaving the high energy end of the tank the beam is defined by a set of object slits and focussed by a triplet of quadrupole lenses before entering the analyzing magnet which transmits only particles of preselected energy.

The beam is refocussed beyond the magnet and passes through a set of defining slits whose jaws are connected via a feed back amplifier to the high voltage source. This feed back device controls the terminal voltage to ∿0.5 keV. The beam is then directed to one of the experimental areas by the switching magnet.

A number of quadrupole lenses and magnetic steerers are strategically placed to guide the beam and focus it at the target position. A number of quartz plugs are located at foci along the beam line to enable one to steer the beam down the axis of the beam line. These are viewed by closed circuit TV cameras through viewing ports. After the beam is suitably focussed on the quartz it can be rotated out of the way.

The gamma ray and electron experiments were performed on the 33° line which terminated in a graphite Faraday cup about 3 meters from the target. The current collected by this cup can be used as a monitor of the beam strength. To prevent the intense neutron and gamma ray fluxes created at this beam stop from increasing the background at the target position, the cup was surrounded by paraffin and shielded with concrete and lead.

4.3 Targets and Beam Intensities

The targets used for the gamma ray and electron experiments were self supporting foils of isotopically enriched ^{149}Sm. They were prepared by evaporating the metal from a mixture of samarium oxide and lanthanum filings onto a tantalum plate. The lanthanum served as a reducing agent. The small globule of evaporated samarium was removed from the plate and cold rolled to the desired thickness.

The enriched samarium oxide was obtained from the Oak Ridge National Laboratories, Tennessee. Its composition is given below.

Sm Isotope	Atomic %
144	0.08
147	0.33
148	0.55
149	97.46
150	0.65
152	0.70
154	0.30

4.3.1 Electron Experiments

For the electron experiments a target of 1.5 mg/cm^2 was used. A thinner target (∿.5 mg/cm^2) would have been preferable but could not be fabricated by the cold rolling technique. For thicknesses less than ∿1.5 mg/cm^2 the foil suffered multiple fractures. The alpha beams used in the electron measurements varied from 500 to 2000 na.

4.3.2 Gamma Ray Experiments

For the direct gamma ray measurements, foils of thickness 3 mg/cm^2 to 8 mg/cm^2 were used and the beam current and detector-target distance adjusted to give the maximum counting rates consistent with good resolution. Since in the gamma-gamma coincidence measurements, one must maximize the solid angle subtended by each detector at the target, the detector-target distance is no longer a free variable. For these experiments it was necessary to use 3 mg/cm^2 targets and beam currents of <1 na, despite the fact that the accelerator does not stabilize well on such small currents. For the direct measurements, the beam currents varied from 10 to 20 na.

4.4 Ge(Li) Detectors

The following Ge(Li) detectors were used for the gamma ray experiments.

Detector	Resolution
1cc Planar	1.48 keV at 706 keV
14cc Planar	1.77 keV at 706 keV
37cc Coaxial	2.60 keV at 1330 keV
42cc Coaxial	2.46 keV at 706 keV
50cc Coaxial	3.99 keV at 706 keV

4.4.1 Choice of Detector

The choice of detector depended on the experiment. The high resolution of the 1cc detector made it the best choice for direct spectra below 700 keV. The good resolution of the 14cc detector made it the preferred choice for angular distribution measurements and other direct spectra in the range 500 keV to 1.5 MeV. The 42cc and 50cc detectors were used for the gamma-gamma coincidence experiments because of their high efficiencies.

4.4.2 Energy Calibration

Calibration lines in the spectra were obtained by simultaneously recording the (α,2n) spectrum from the target and radiations from a number of IAEA standard sources. The positions and areas of the gamma ray peaks were determined by the computer peak fitting program described in section 4.5

The positions of the gamma ray peaks from the standard sources and the positions of the various x-ray peaks were used to define the coefficients in the expression

$$E = a + bx + cx^2 + dx^3 \qquad [4\text{-}1]$$

which relates the photon energy (E) to the channel number (x). The Nuclear Data 4096 channel ADC's were found to be very close to linear except for the lowest 1000 channels. The differences between accepted and fitted values were of the order of 0.05 keV. Spectra were usually fitted in two overlapping sections using a cubic energy fit for the first 1000 channels and a linear fit for the rest. The calibration functions so defined were then used to generate the energies of the unknown gamma ray peaks in the spectrum.

4.4.3 Efficiency Calibration

Efficiency curves were determined in one of two ways for each detector each time it was used. This was necessary because of the gradual deterioration of the detectors induced by neutron damage.

The first method required the use of a set of absolutely calibrated IAEA standard sources. In this method it was important that the sources be placed in the same position as the beam spot on the target. Since this was not practicable with the actual beam line, the section containing the target was replaced by a "dummy" section with a slot in it which permitted the standard sources to be reproducibly located at the precise position of the target in the real beam line. Spectra were collected for each standard source for a preset length of time. The IAEA source strengths were corrected for decay since the calibration date was known and for the gamma ray branching in the source to yield a photon intensity for each standard line. A comparison of this with the counting rate in the corresponding peak of the spectrum yielded the absolute efficiency. This was repeated for standard sources covering the entire energy range of interest.

A much more convenient method for determining relative intensities became available later in the project, as a result of the detailed study carried out in this laboratory on the decay of ^{151}Pm to levels in ^{151}Sm (Cook et al, 1973). As a result of this work, spectra containing a wealth of lines of accurately known relative intensities and energies covering the entire range from 25 keV to 1 MeV could be recorded in a very short time to produce a well defined calibration curve.

4.5 Direct Gamma Ray Experiments

4.5.1 Geometric Arrangment

In performing gamma ray experiments it is important to minimize the amount of material between the detector and the source and to be able to calculate accurately the effect of the material which cannot be removed. Furthermore it is necessary to monitor the position of the beam at a point fairly close to the target position to ensure that the beam cannot wander off the target and create undesired background radiation.

These aims were accomplished by the beam line which is shown schematically in Fig. 4-1. Two pairs of separately insulated tantalum slits were used to define a 3 x 3 mm aperture for the beam, 20 cm from the target. This design permitted the current on each jaw to be monitored separately, thereby simplifying the steering and focussing of the beam. Under ideal conditions it was possible to focus the beam so that ∿99% of the current passed through the jaw. The lead plug behind this device shielded the detectors from gamma rays originating in the slits. The tantalum shield, with a 7 mm aperture placed 50 cm upstream from the target was installed to ensure that scattered alpha particles did not reach the aluminum beam line.

The thin foils were mounted on lead frames, attached to the target holder and oriented at 45° to the beam. Since the detectors were located at 90° to the beam direction, this orientation minimized the gamma ray attenuation in the target and frame.

4.5.2 Pulse Analysis

For the direct gamma ray experiments, pulses from the detectors were amplified by commercial FET preamplifiers (Ortec) and linear amplifiers (Ortec 452 or Tennelec TC203). A time constant of 2 μsec was used in the linear amplifiers and care was taken to adjust the pole zero compensation to optimize energy resolution. A baseline restorer coupling the signals to the ADC's was found to provide further improvement in resolution at high counting rates.

The data were collected using either the ND3300 multichannel

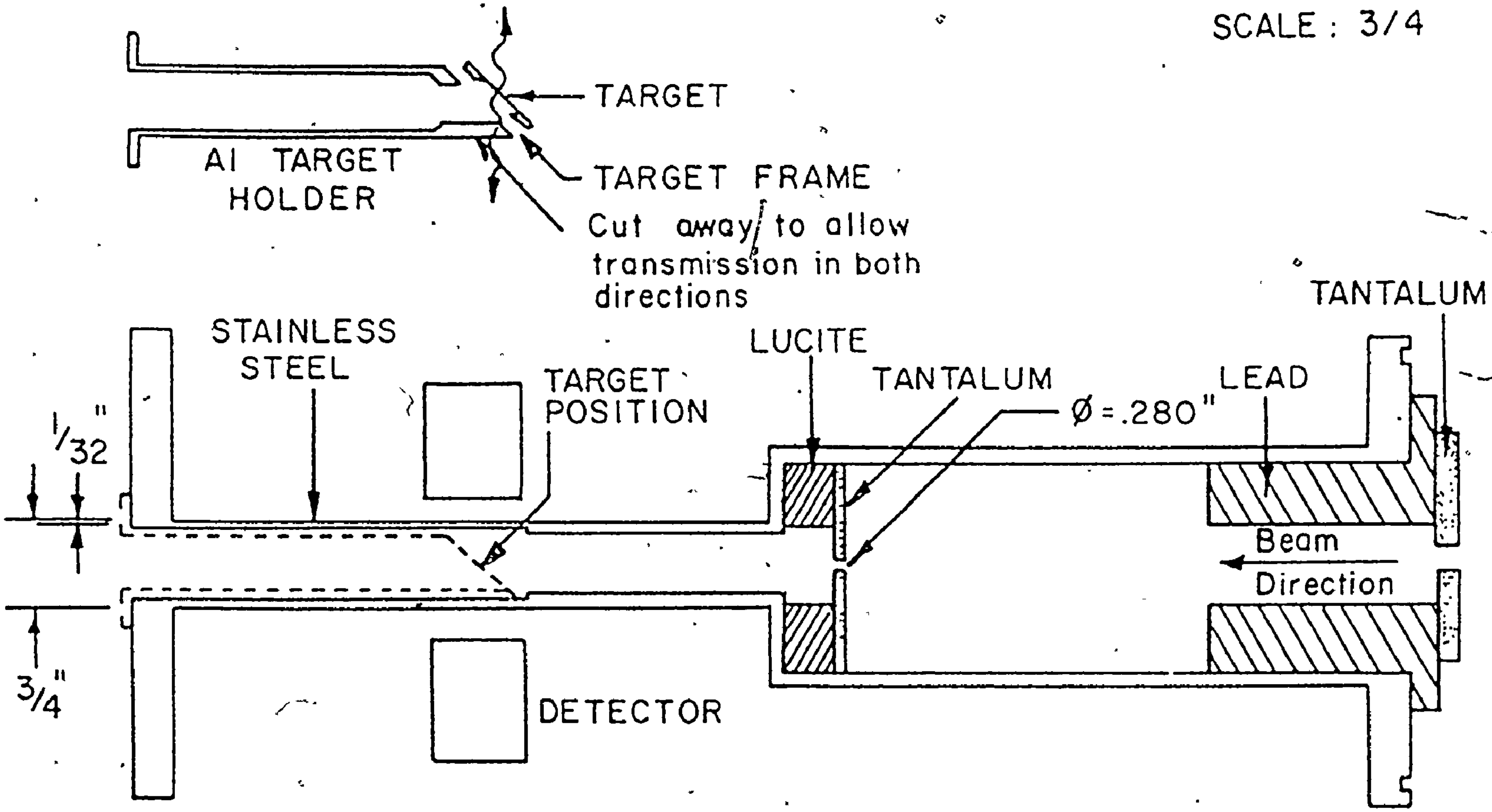

Figure 4-1

Target chamber and target holder.

analyzer or a PDP-9 computer interfaced to the ADC's. The spectra were stored on magnetic tapes and analyzed on the CDC6400 computer using the program JAGSPOT described by Cook (1972). Briefly, the program performs a least squares fit to the peak shape which is a convolution of a decaying exponential curve and a Gaussian curve, and which can be mathematically expressed as follows:

$$I(x) = \alpha + \beta x + \sum_{j=1}^{N} \gamma_j \int_{-\infty}^{x_{pj}} e^{\varepsilon(y-x_{pj})} \, e^{-\delta(x_{pj}-y)^2} \, dy \qquad [4\text{-}2]$$

where:

x = channel number

$I(x)$ = counts in channel x

N = number of peaks in window ($N \leq 6$)

$\alpha+\beta x$ = linear background term

γ_j = intensity of the Gaussian located at x_{pj}

ε = constant determining the exponential fall-off of Gaussian intensities

x_{pj} = peak position of Gaussian in peak j.

Several strong peaks spanning the spectrum were used to determine the width and tailing parameters as functions of channel number. For the weaker peaks the parameters used were determined from these functions.

4.6 Excitation Functions

The excitation functions of individual lines were determined by recording the spectra at a series of beam energies from 15 to 24 MeV in the geometry of section 4.5.1. The ratio of the peak area corresponding to a selected gamma ray to the area of the strong 108 keV peak was determined in each spectrum. A plot of this ratio as a function of beam energy represents the excitation function of the gamma ray relative to that for the 108 keV ground state transition from the first excited state.

4.7 Gamma-Gamma Coincidence Experiments

4.7.1 Geometric Arrangement

For the gamma-gamma coincidence experiments the Ge(Li) detectors were oriented at 90° to each other and to the beam line. A lead shield was placed between them to reduce scattering from one detector to another. In order to maximize the solid angle the detectors were positioned as close to the target as this geometry would allow. In practice this meant that the front surface of the detector was about 5 cm from the centre of the target (i.e. 3 cm to the front surface of the detector housing.

4.7.2 Pulse Analysis

A block diagram of the circuitry used is shown in Fig. 4-2. Pulses from the detectors were processed by Ortec 454 timing filter amplifiers. The output signals were then fed into Ortec 453 constant fraction timing discriminators to produce timing pulses which were

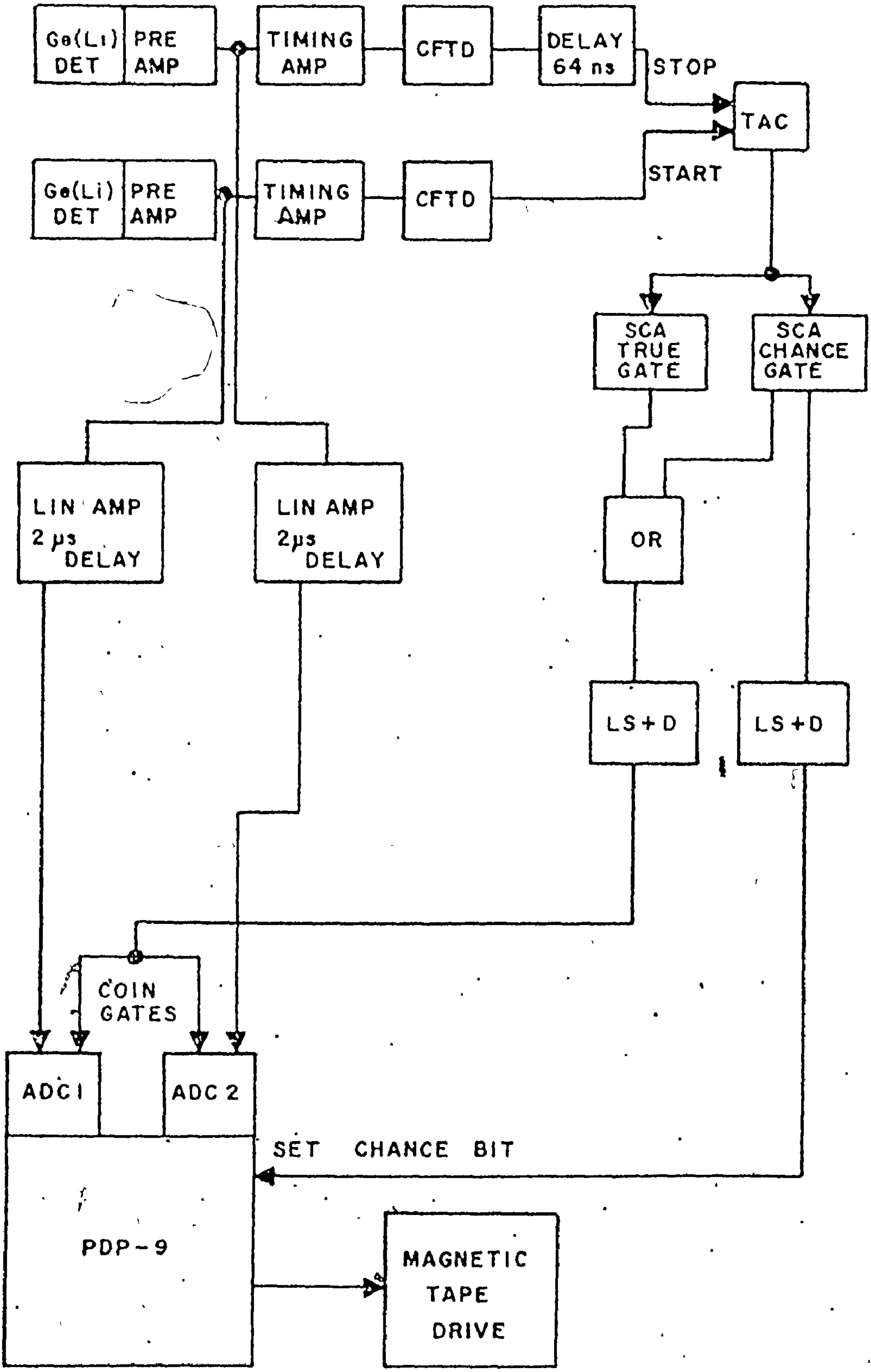

Figure 4-2

Block diagram of circuitry used in γ-γ coincidence experiments.

appropriately compensated for variations in pulse height and rise time. The timing pulses from both detectors were then fed into an Ortec time to amplitude converter (TAC) to produce the spectrum of the timing pulses. The width of the TAC peak (30 ns FWHM) provides a direct measure of the system timing resolution. In order not to discriminate unduly against coincidences involving low energy transitions a wide gate of 100 ns was set on this peak by means of a single channel analyzer (Canberra 1436). A 100 ns gate was also set on the flat background portion of the spectrum in order to collect the spectrum of chance events. The output of either of these SCA's opened the gates of both ADC1 and ADC2. By scaling the outputs of both SCA's the true to chance rate could be determined. Typically the true to chance rate was ∿70 to 1.

The pulses from the detectors were also amplified by Ortec 452 linear amplifiers, which had been adjusted to optimize the energy resolution, and presented to the ADC's. If the time relation between the pulses was such that the gates were open the linear pulses were admitted to their respective ADC's and analyzed. The digital outputs of the ADC's were stored in the PDP-9 computer as pairs of 18 bit words in two alternating buffers each 1000 words long. When a buffer was full it was dumped sequentially onto magnetic tape while the other buffer was being loaded. Each word contained not only the digital representation of the pulse height but also bits which identified

(i) the ADC from which the word originated

(ii) whether the timing pulse came from the true or chance SCA and

(iii) a sequencing bit which designated a valid word pair.

This sequencing bit was necessary since occasionally a timing pulse opened the ADC gate when one of the pulses presented to the ADC was outside of the range acceptable to its upper and lower discriminators. Under such circumstances only one 18 bit word was written and the sequencing bit enabled the computer to recognize and reject this as an incomplete pair rather than trying to couple it to the next word on the tape. A detailed description of the word structure is given by Cook (1972).

4.7.3 Coincidence Data Analysis

It was usual to collect 20 x 10^6 coincidence events during an experiment. The data was sorted on the McMaster CDC6400 computer using a code which made use of the large mass storage available. All tapes were initially unloaded onto the disks of the computer using a routine which removed the 3 unused bits in each 18 bit word and packed four of the resulting 15 bit words into one 60 bit word which was compatible with the 60 bit word structure of the CDC6400 computer. The program searched the record for all the coincidence events for which the ADC output of one detector (the so-called gating detector) fell within a prescribed range of channels. The computer collected these events and plotted them to give the spectrum in coincidence with the prescribed gate. Gates could be set at will on either peaks or background regions in the "gating" detector and subtractions performed so that the output represented a pure spectrum of events in coincidence with the photopeak of the gamma ray selected by the gate without any contribution from the Compton distributions associated with higher energy transitions. The chance contribution was also obtained and subtracted in the same manner.

The areas of the peaks observed in the coincidence spectra were used in the manner described below to obtain the coincidence probabilities between the gating transition and the gamma rays observed in its coincidence spectrum.

The number of coincidence events between the two full energy peaks γ_i and γ_j is given by,

$$N(\gamma_i,\gamma_j,\theta) = N_o\varepsilon_1(\gamma_i)\varepsilon_2(\gamma_j)\varepsilon_{ij}f_g\omega_1\omega_2C_{ij}W(\theta_{ij}). \qquad [4\text{-}3]$$

In this expression N_o is the number of nuclei of the type under study produced during the course of the experiment, $\varepsilon_1(\gamma_i)$ and $\varepsilon_2(\gamma_j)$ are the intrinsic detector efficiencies, ε_{ij} is the coincidence efficiency of the circuit, ω_1 and ω_2 are the geometric solid angles of the two detectors, C_{ij} is the coincidence probability or the probability of finding γ_i in coincidence with γ_j, f_g is the fraction of the photopeak of the gating transition in the gate and $W(\theta_{ij})$ is the angular distribution function for the pair of transitions under study.

As long as one knows the energy dependence of ε_1 and ε_2 it is not necessary to measure $(\varepsilon_1\omega_1)$ and $(\varepsilon_2\omega_2)$. The coincidence efficiency ε_{ij}, is unity except when low energy gamma rays are being detected. In the present experiments, ε_{ij} began to decrease rapidly when γ_i or γ_j fell below 100 keV and it was not possible to make quantitative use of coincidence probabilities for cascades involving transitions below

80 keV. The value of f_g in the analysis was unity except when narrow gates were set to separate close lying doublets. In these cases graphical means were used to estimate f_g.

Since the (α,2n) reaction transfers a large amount of angular momentum to the target nucleus, the product nucleus in its initial highly excited state is aligned with a strong population in the m=0 substate referred to a quantization axis along the beam direction. As a consequence the function W(θ) may show a strong angular dependence which is dependent on both the spins and population parameters of the states involved in the γ-γ cascade. Since the function W(θ) cannot be readily evaluated, all that one can do is to minimize its effect by keeping ω_1 and ω_2 as large as possible and assuming that W(θ) = 1. Absence of knowledge concerning W(θ) provided the largest uncertainty in the values of C_{ij} derived for strong cascades, limiting the reliability of these measurements to ±25%.

With the approximations suggested above the value of C_{ij} can be expressed as

$$C_{ij} = \frac{N(\gamma_i\gamma_j)}{K\varepsilon_1(\gamma_i)\varepsilon_2(\gamma_j)} \qquad [4-4]$$

where the K factor includes all terms not dependent on the energies of the gamma rays. Since in practice C_{ij} is known for some of the strong cascades involving low lying levels in the nucleus under study, these cascades can be used to determine K. In the case of ^{151}Gd a mean value of K was determined by considering the 406-379 keV cascade with C_{ij} = 39.2. This mean was used for all the other coincidence probabilities.

The experimental C_{ij} values determined in this fashion were compared with those predicted from the level structure and photon intensities and used as a critical test of the level scheme.

4.8 Angular Distributions

4.8.1 Geometric Arrangement

The target-detector geometry of Fig. 4-1 was not well suited for the determination of the gamma ray yield as a function of the angle between the direction of emission and the beam direction since it was impossible to obtain measurements for $\theta<30°$. In order to make measurements at smaller angles to the forward direction the arrangement shown in the accompanying sketch was constructed.

In this arrangement the beam line terminates in a cylindrical steel chamber with a vertical axis and the target is mounted on the axis of the cylinder. In order to reduce the attenuation of the gamma rays emitted in the forward direction ($\theta<90°$), the cylinder wall in the equatorial plane was reduced to 0.1 cm. The interaction region on the target was defined by a circular tantalum aperture 7 mm in diameter, located 2 cm in front of the target. Alignment was monitored by reading the current intercepted by this aperture. The beam was stopped in a lead absorber 0.02 cm thick located immediately behind the target. While this arrangement allowed one to obtain spectra from $\theta = 0$ to $90°$, the spectra suffered from contamination contributed by the lead absorber and the tantalum aperture. In order to identify this contamination a spectrum of the chamber without the target present was also taken.

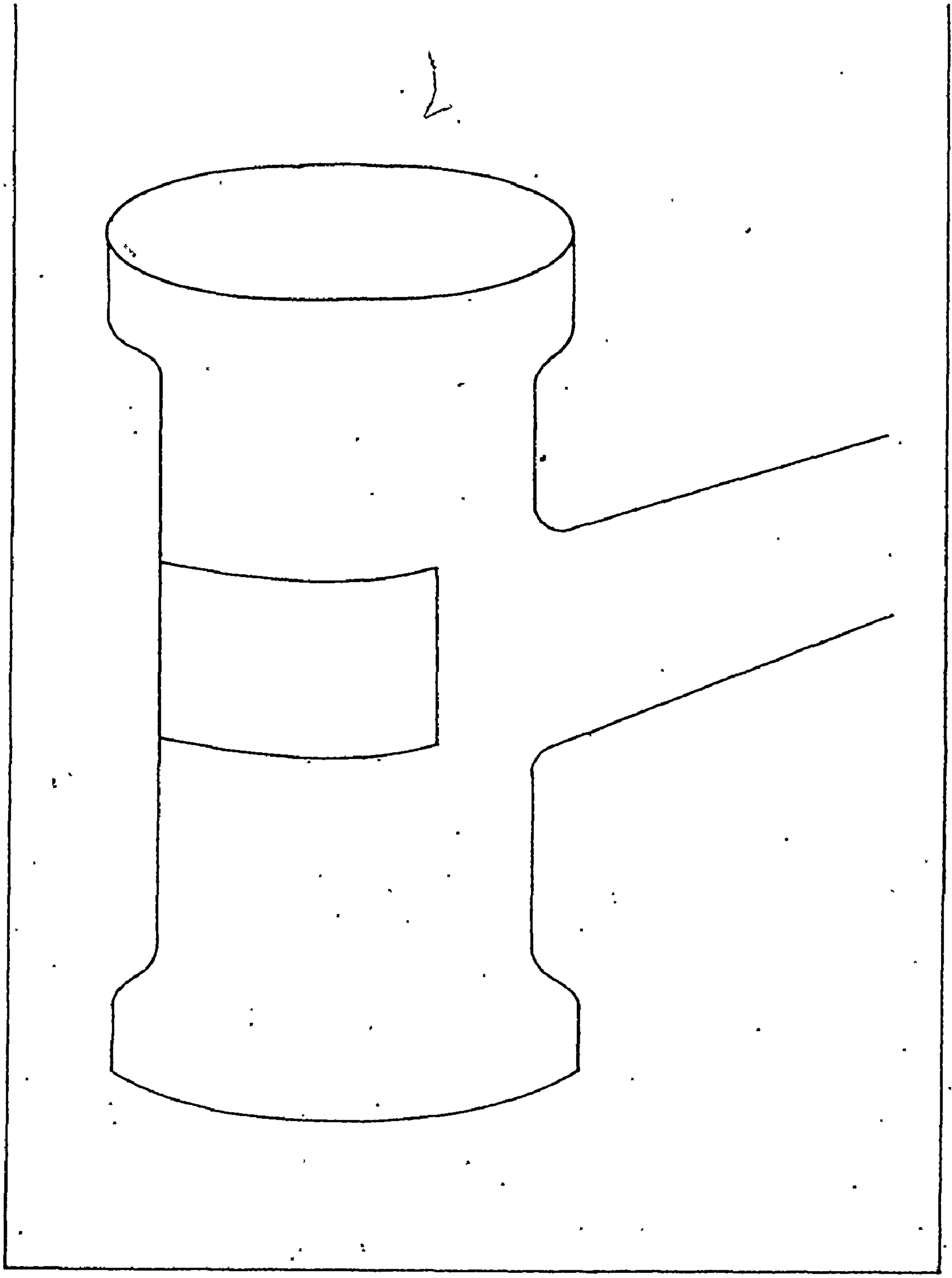

Figure 4-3

A sketch of the target chamber used for taking angular distribution measurements. With this chamber it was possible to take measurements at angles less than 30°.

Angular distribution measurements were carried out using this chamber, with the front surface of the Ge(Li) detector housing 17 cm from the target.

4.8.2 Normalization

In order to obtain angular distributions which were independent of beam current, the counting rate in the movable Ge(Li) detector for each peak was compared with the total counts in a fixed Ge(Li) detector mounted on the opposite side of the beam from the movable detector.

Because the counting rates were large, counting losses in the two ADC's ranged from 20 to 30% depending on the beam current. Moreover, because the counting rate in the movable detector varies significantly with angle, the counting losses were angle dependent. To correct for these variations, the output pulses from each of the Ge(Li) detectors were fed both to a scalar and to the ADC and the counts accumulated in the scalar over the 3 or 4 hour period, required to obtain good statistics at a given angle, were recorded. A comparison of this scalar count with the total number of counts in the spectrum from the ADC gave the required correction factor.

In the experiment carried out with a lead backing behind the target material, it was necessary to correct for the differential absorption in the lead as the angle was moved from 0° to 90°. The plane of the target was set at 45$\pm$ 2° to the beam direction so that the thickness of the lead backing varied from t at 45° to $t\sqrt{2}$ at

0° or 90°. With the backing thickness of 165 mg/cm^2 of lead, the change in attenuation of the lead backing in moving over this 45° range varied from 36% at 65 keV to 0.8% at 800 keV. The uncertainty in the magnitude of this correction creates a significant uncertainty in the angular distribution of gamma rays below 100 keV.

Angular distributions were obtained in this experiment at seven angles equally spaced from 0° to 90° to the beam direction.

A second set of angular distributions was carried out in a geometry where the beam was stopped in the beam dump. The spectra in this experiment were relatively free of contamination lines but it was not possible to make measurements at small values of θ. The data in this experiment, accumulated at angles of 30°, 60°, 70° and 90°, were inferior to the seven angle distributions because of a breakdown in the monitoring procedure and because the absence of data at small angles makes the data insensitive to the A_4 term in the polynomial expansion. The data were used to obtain information on lines masked by contaminant peaks in the spectra of the seven angle distribution experiment.

4.9 Conversion Electron Experiments

4.9.1 The Orange Beta Ray Spectrometer

The 7 gap "orange" beta ray spectrometer located on the 33° line was patterned after the Chalk River version of Geiger (1965) (Fig. 4-4). It consists of seven 1/r sector magnets arranged symmetrically about a vertical axis. Six of these focus electrons originating from the

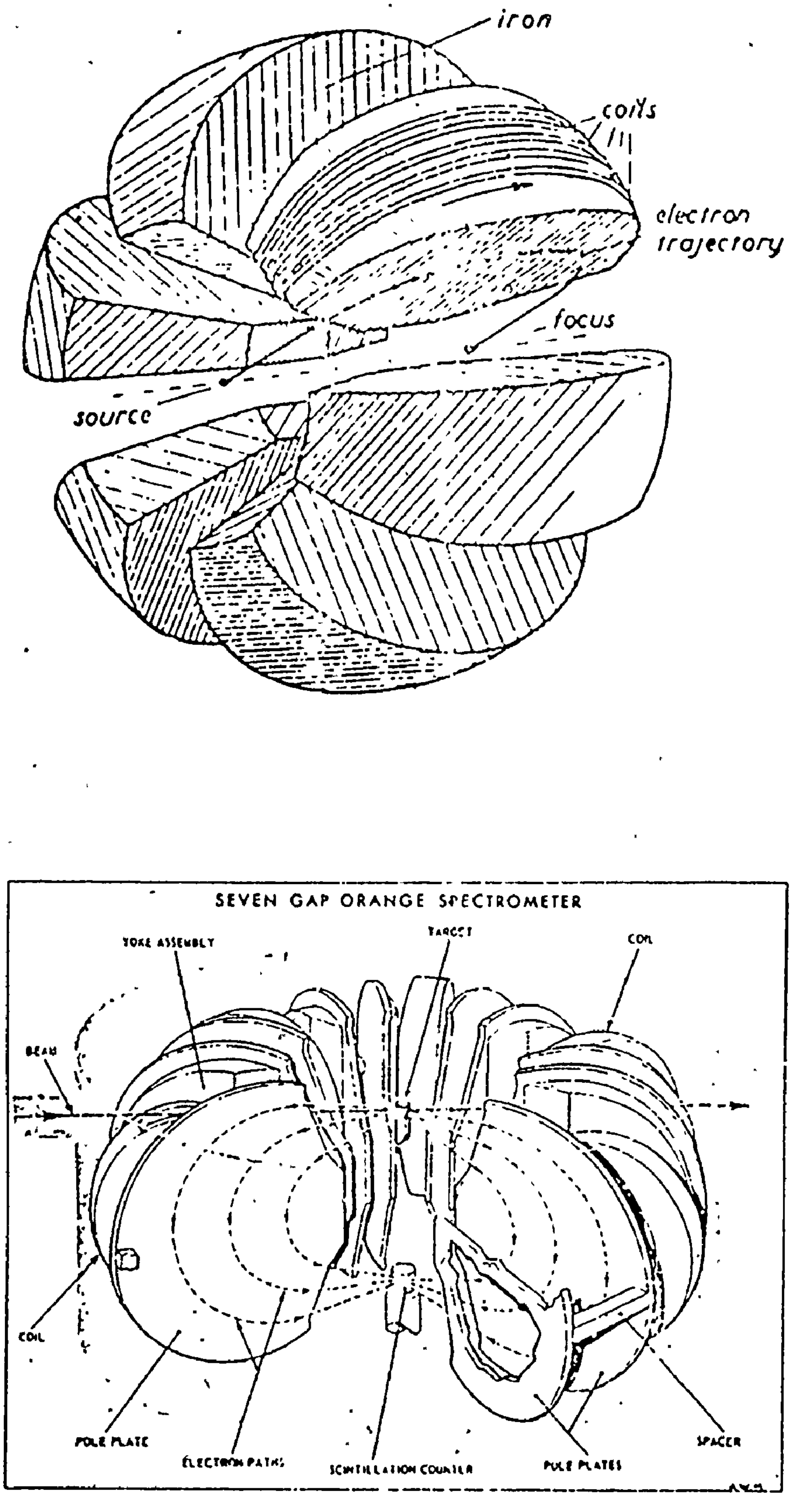

Figure 4-4

Schematic illustration of the "Orange" beta ray spectrometer. (From Geiger 1965).

common source or target located on the symmetry axis at the top of the apparatus. The seventh gap is reserved for the Rawson probe which measures the field intensity in the gaps. A current feedback system using the signal from the Rawson probe maintains the field constant to 5 parts in 10^5. The magnetic fields focus the electrons on a small cylindrical plastic detector at the lower end of the symmetry axis. The transmission of the spectrometer is defined by an annular ring located in the Z=0 plane. For a given baffle width the resolution is defined by the source dimensions. With the normal baffle settings and a source 3 mm x 5 mm a momentum resolution of $\Delta P/P = 0.5\%$ can be achieved. In practice, the energy loss of the electrons in passing through the target increased the resolution to ∿0.9%.

4.9.2 Beam Definition

It is very important that the interaction area of the beam with the target lie on the axis of the spectrometer. The procedure used to achieve this is outlined below.

A set of four separately insulated tantalum jaws forming an aperture 2 mm x 4 mm was located at the target position and a beam of 24 MeV alphas was focussed to pass through this aperture. When properly adjusted it was possible to reduce the beam current to each jaw to ∿1 na. when the total beam current was 500 na. Under such circumstances less than 1% of the beam fell outside the axial interaction area. Not only was a small well defined interaction area necessary for good resolution but it was also required when using non uniform targets. After the beam had been focussed in this way, a second set of jaws was inserted 60 cm upstream from the target position and adjusted until the beam passed through both sets of jaws. The upstream set of jaws was then locked in place and the target slits replaced by the target. The current to the upstream slits was monitored constantly and the steerers adjusted if the beam wandered. An effect on the electron background was observed if the fraction of the beam intercepted by the upstream jaws became as great as 5% of the total beam.

4.9.3 Anti Scattering Devices

As a result of the efforts of many workers before these experiments were done, the background at the electron detector had been reduced to the point where it was almost entirely due to electrons from the interaction region of the target. A detailed description of the steps taken is given by Khoo (1972). Among these were

(i) the construction of an enlarged pipe (Fig. 4-5) and beam line to ensure that alpha particles which had undergone small angle scattering in the target did not reach the beam line until they were within the shielded beam dump.

(ii) the introduction of heavy lead shielding between target and detector.

(iii) the installation of aluminum absorbers over the lead shields to reduce the number of scattered electrons and x-rays from the inner surfaces of the spectrometer.

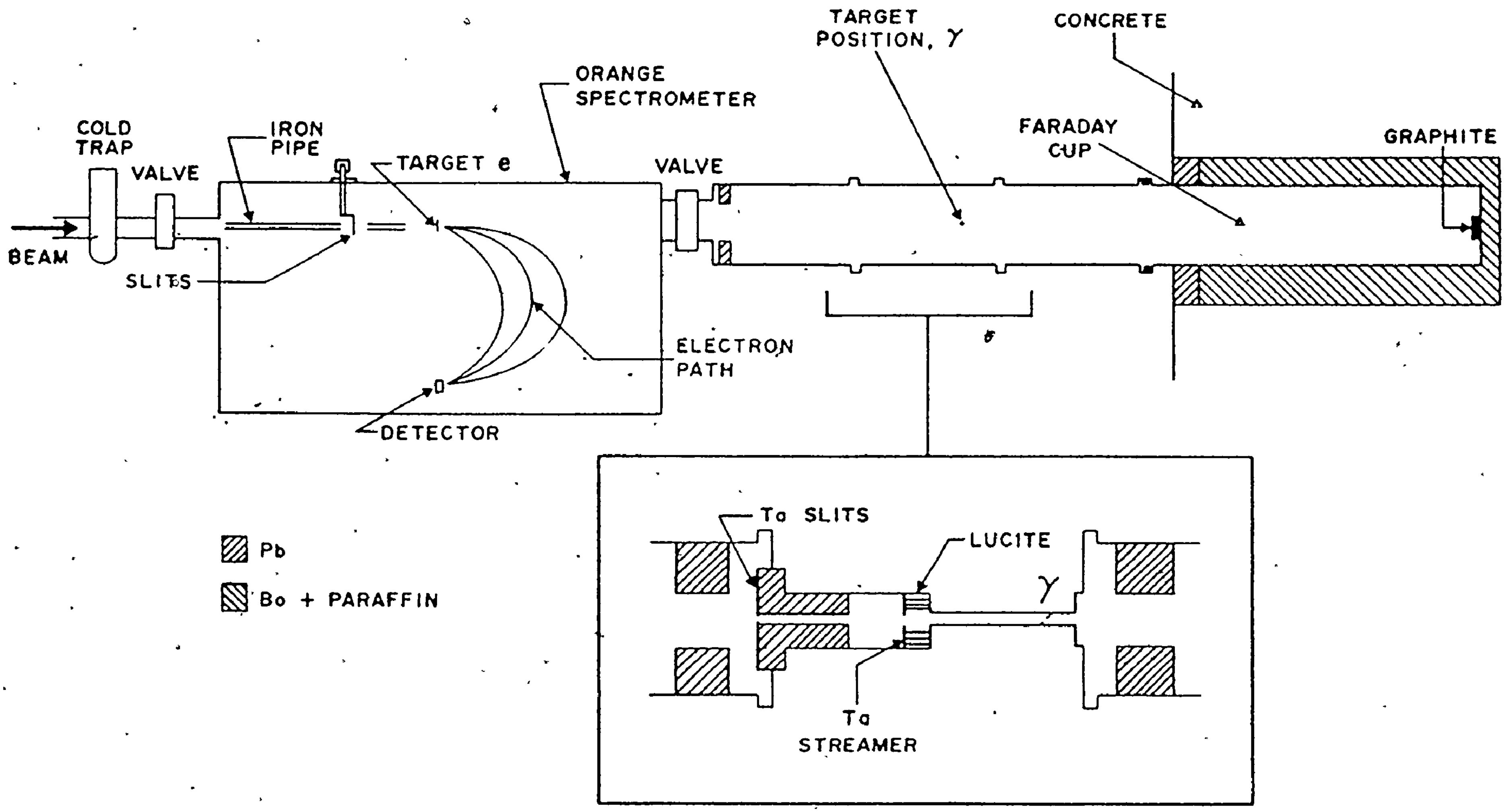

Figure 4-5

Target area of the 33° beam line. The target positions for electron and gamma ray measurements are indicated by e and γ, respectively

(iv) the introduction of anti scattering baffles on the inner surfaces of each of the gaps to prevent low energy electrons from reaching the detector by multiple scattering.

The most serious limitation on the usefulness of the spectrometer is the presence of the electrons (δ-rays) created by the interaction of the alpha beam with the atomic electrons of the target. The intensity of the continuous δ-ray spectrum falls off as a high power of the electron energy and is unimportant above 200 keV. At energies up to ~75 keV these electrons are so intense as to mask all but the very strongest conversion lines.

4.9.4 Data Recording

By automatically stepping the magnetic field, electrons of various energies were brought to focus on the detector. Due to variations in beam current and stability, measurements of the elapsed time or the charge collected by the Faraday cup are not very reliable measures of the number of nuclear interactions. Because the Rutherford scattering cross section increases as Z^2, low Z impurities in the target contribute very little to Rutherford scattering. Thus the number of Rutherford scattered alpha particles detected at a fixed angle to the beam direction provides a very good measure of the reactions of concern. The scattered alphas were detected by a 1 cm diameter plastic scintillator with a 7764 RCA photomultiplier, located on the side of the spectrometer at an angle of 52° to the beam direction. Thus the number of electron counts at each $B\rho$ value was recorded for a preset number of scattered alphas. For diagnostic purposes both the integrated current and the elapsed time were also recorded.

The following automatic stepping cycle was followed. At the termination of a counting period a command pulse from the master scalar caused all of the scalar readings to be recorded on the teletype. While this was going on, the magnetic field was increased by a preset amount, which corresponded to an increment in Bρ of 1,2,5 or 10 gauss-cm, and allowed to stabilize for 4 sec before the scalars were reset and counting was resumed.

4.9.5 Pulse Analysis

A single channel analyzer was set on the output of the alpha detector to discriminate between the alpha particles scattered by the Sm atoms in the target and those scattered by the lighter impurity atoms.

A single channel analyzer was also used on the electron detectors in order to reject the low energy background which contributed nothing to the electron peaks of interest but served only to increase the background. Because the pulse height corresponding to the focussed electrons increases linearly with the electron energy, it was necessary to place a very wide window on the electron output or to move the window upward in energy as the scan from low to high energy proceeded. The situation is illustrated in Fig. 4-6

In order to establish the efficiency for a selected portion of the electron spectrum, a plot of electron energy vs peak position was first constructed. This enabled us to determine the zero position of the ADC (lower part of Fig 4-6). Hence we could estimate the portion of the low energy tail lost by the electronics. This low energy tail results from

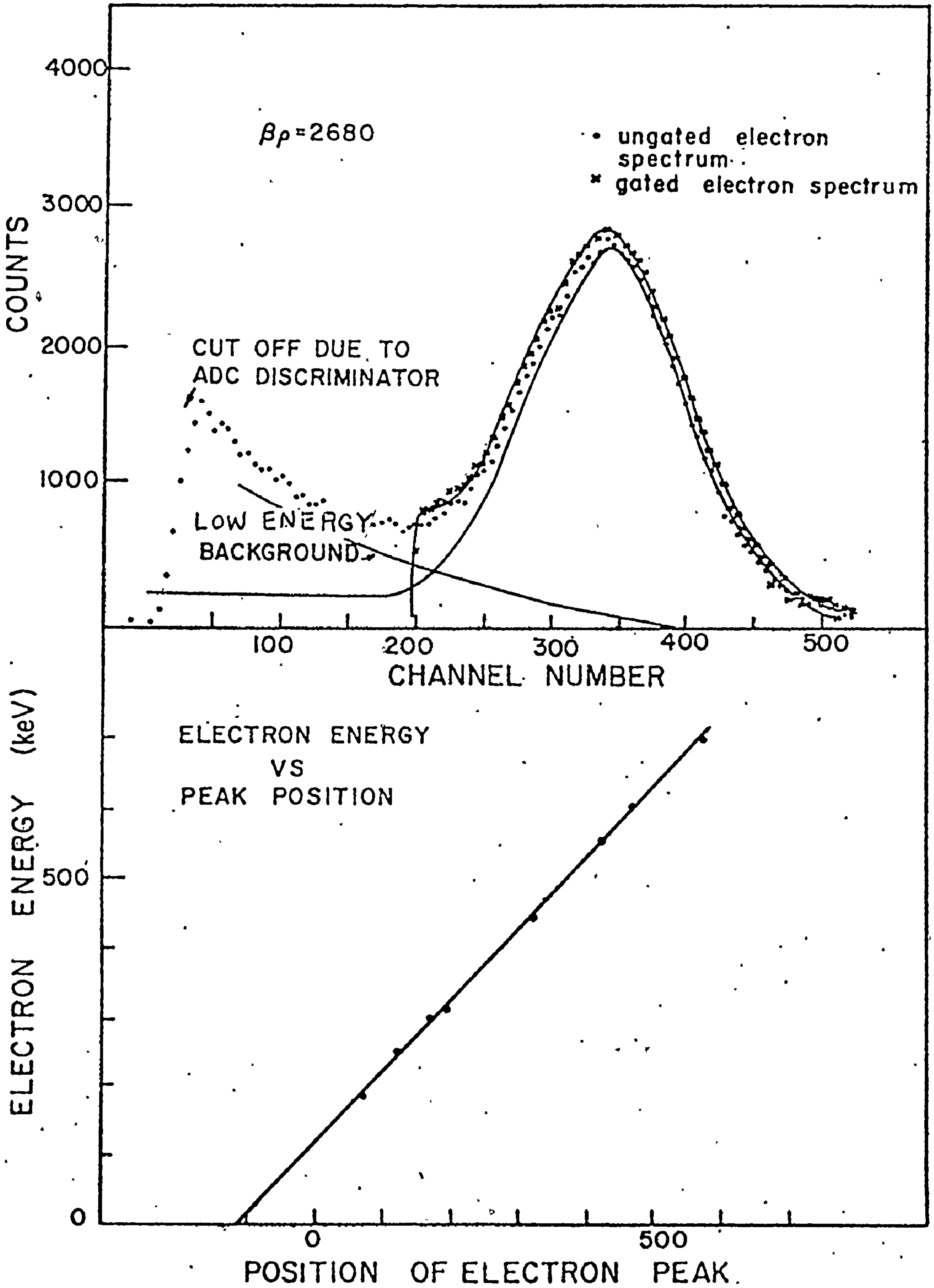

Figure 4-6

Energy and efficiency calibration considerations for the conversion electron analysis.

focussed electrons backscattered from the detector and the height was determined from electron spectra at higher values of Bρ where the electron peak does not merge with the low energy background. The low energy background results from the unfocussed electrons ejected from structural materials by gamma rays which have scattered into the detector chamber despite the shielding. From previous work (Khoo,1972) it is known that neutrons contribute very little to the background.

The ungated spectrum shown in the upper part of Fig. 4-6 allowed us to estimate the low energy contribution to the spectrum and correct for it. Knowing the position of the gate and the height and extent of the low energy tail it was possible to calculate the efficiency of the gated system.

Uncertainties in the efficiency may be as high as 10% in unfavourable cases such as the lower energy electrons where the peak starts to merge with the low energy background. For the higher energy electrons the efficiencies can be determined to 5%. They ranged from 80% to 95% and wherever possible calibration peaks were recorded with the same efficiency.

4.9.6 Calibration

Prior to the present experiments the beta ray spectrometer had been calibrated using the K conversion line of the 411.8 keV transition in ^{198}Au (Bρ=2222.5 gauss-cm) as a standard. With the spectrometer focussed on the peak, the digital Bρ readout had been adjusted to 2222.5 to make the spectrometer direct reading. In practice, however, the beam does not always strike the target at exactly the same height so that calibration shifts of ∿1% can occur from one experiment to another. In fact, the energies of all the electron peaks observed could be calculated more precisely from the known gamma ray energies and the K and L shell binding energies than they could be measured with the spectrometer, and the data were used to establish conversion line intensities rather than transition energies.

4.9.7 Data Analysis

The areas of the various peaks were determined by a peak fitting program which is similar in many respects to that used for gamma rays (Jagspot). Since the energies of the peaks to be expected, in a region extending over ~100Bρ were known from the gamma ray experiments, a major peak in the region to be fitted was selected as a reference peak and the positions of all others placed relative to it. Thus, in the least squares fitting process, only the position of the major peak was treated as a free parameter. The other free parameters were the width and tailing parameters (assumed the same for all peaks in the region) and the heights of the individual peaks. Otherwise relatively weak peaks would be eliminated by a slight shift in the position and a small alteration in the shape of a larger peak.

Experimental conversion electron intensities were obtained by dividing the measured electron peak areas by Bρ and by the efficiency of the electron detector in the beta spectrometer. The division by B_ρ is necessary because the response function of the spectrometer for monoergic electrons has a Gaussian shape whose "width" is proportional to Bρ. After this division has been carried out, all electron peaks acquire the same width, except for differential effects caused by the finite thickness of the target.

To obtain internal conversion coefficients, the true electron intensities were divided by the corresponding intensities of the gamma rays measured with a 24 MeV alpha beam at an angle of 55° to the beam direction. Normalization between the electron and gamma ray intensity scales was achieved by using a number of pure E2 transitions in ^{152}Gd and ^{151}Gd.

Several experiments were needed to cover the energy range of interest. Unfortunately on the last of these the shape of the peak was altered by a malfunction of the apparatus. However by selecting several simple groups it was found that the peak shape could be represented as the sum of two skewed Gaussian curves. The secondary peak was 13 units of Bρ higher than the parent curve at Bρ = 1600 and 15 units of Bρ higher at Bρ =3500. It contained 23% of the area of the parent curve. The program was modified to reproduce these peak shapes which were then used to fit the data.

Chapter 5

EXPERIMENTAL RESULTS FOR ^{151}Gd

5.1 Introduction

The low spin states in ^{151}Gd populated in the electron capture decay of ^{151}Tb have been studied by several workers (Kormicki (1967), Vilskii (1967) and Gonsior (1971) and Hammaren et al (1975)). The first reaction study to be made was that of Tjøm and Elbeck (1967) who used the (d,p) and (d,t) reactions to survey the particle states of the odd mass gadolinium nuclei. This was followed in 1968 by the work of Ejiri et al who studied the conversion electrons following the (α,3n) reaction on ^{150}Sm. These authors identified conversion lines associated with some of the strong transitions in ^{151}Gd but were unable to obtain useful internal conversion coefficients. Ekstrom (1973) used atomic beam techniques to establish the ground state spin of ^{151}Gd as 7/2, a value consistent with shell model predictions.

A critical survey of the literature up to December 1975 has recently been published by Harmatz et al (1976).

In the summer of 1973, it was discovered at a Gordon Research Conference that a group of workers at Berkeley were also studying ^{151}Gd using the (α,3n) reaction on a target of ^{150}Sm. These workers had carried out almost the same measurements as the author and agreement between the two sets of data was excellent. Following this the McMaster group published its results on the $11/2^-$ band (Smith et al, 1973) and the Berkeley group concentrated on the positive parity states in the context of the decoupled band theory (Kleinheinz et al. 1974).

Subsequent to these events, a more detailed analysis of our very complete coincidence data revealed serious inconsistencies with the assumptions both groups had made with respect to the spins and parities of a number of states. This led us to make a study of the conversion electron spectrum in order to resolve the problem. The radical consequences of this decision to the decoupled band interpretation will be described in due course.

There is very little overlap between the gamma rays observed in the electron capture studies and those found in the present work. This is not surprising, since the electron capture preferentially populates low spin states (<7/2) while the (α,2n) reaction preferentially populates high spin states. The particle transfer data of Tjøm and Elbek (1967) and more recent measurements (Løvhøiden and Burke (1975)) from this laboratory have provided very important spectroscopic information concerning the character of a number of the particle states populated in our work. As has already been indicated, the measurements of Kleinheinz et al. (1974) agree well with those in this thesis. However, because they had more excitation energy available they observed more intensity in the high spin band members.

5.2 Gamma Ray Singles Measurements

The gamma ray spectrum produced by a beam of 24 MeV alphas on a ^{149}Sm target is shown in Figs. 5-1 and 5-2. The spectrum of Fig. 5-1 which extends up to ∿730 keV was recorded with a high resolution 1cc Ge(Li) detector while that of Fig. 5-2 extending up to ∿1.5 MeV was

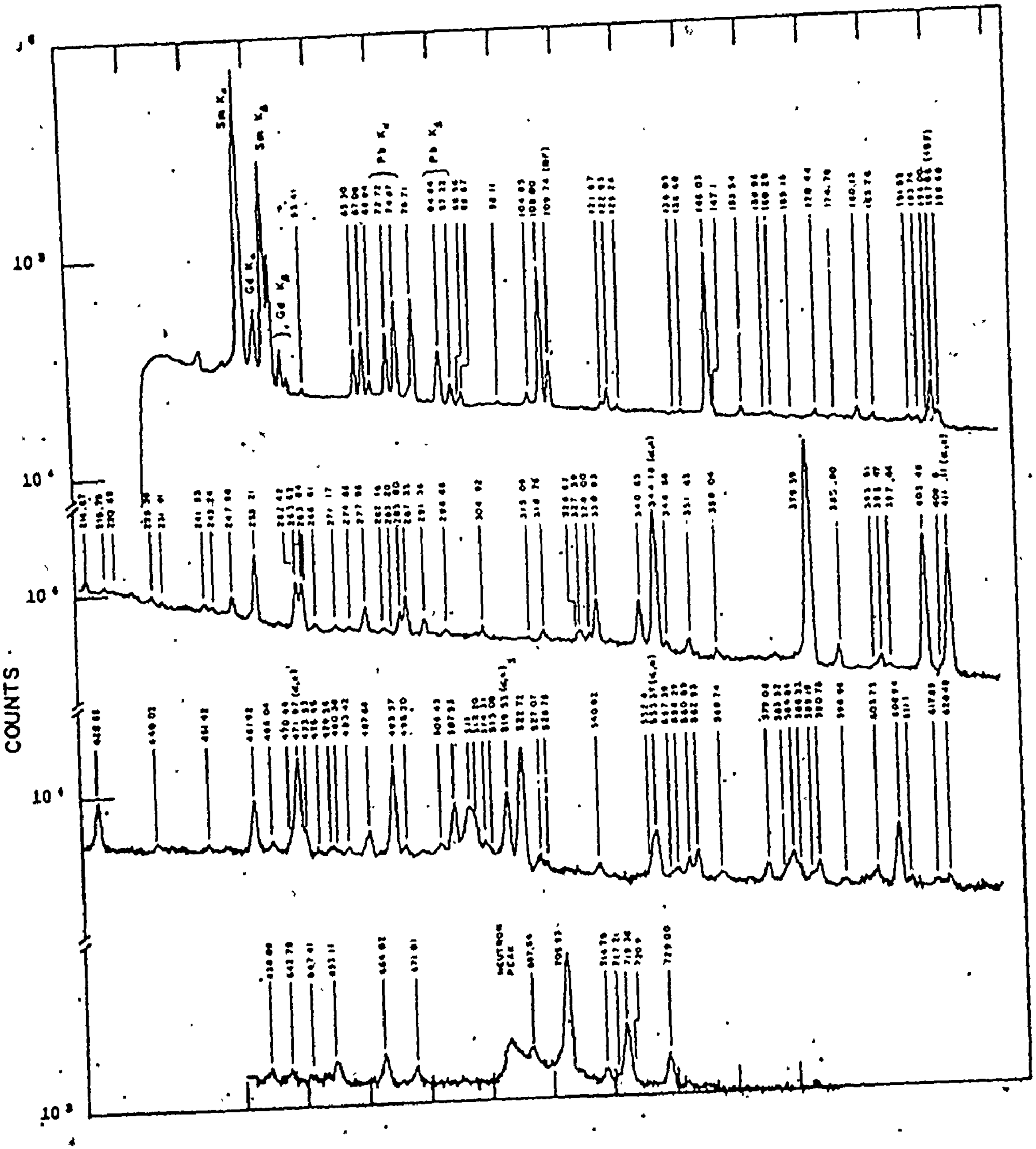

Figure 5-1

Gamma ray spectrum of ^{151}Gd as recorded with a 0.9 cm^3 Ge(Li) detector with a resolution of 1.5 keV at 706 keV. The strong ^{152}Gd peaks from the (α,n) reaction are identified in the figure. Some of the labelled weak peaks are due to ^{149}Sm, ^{153,154}Gd.

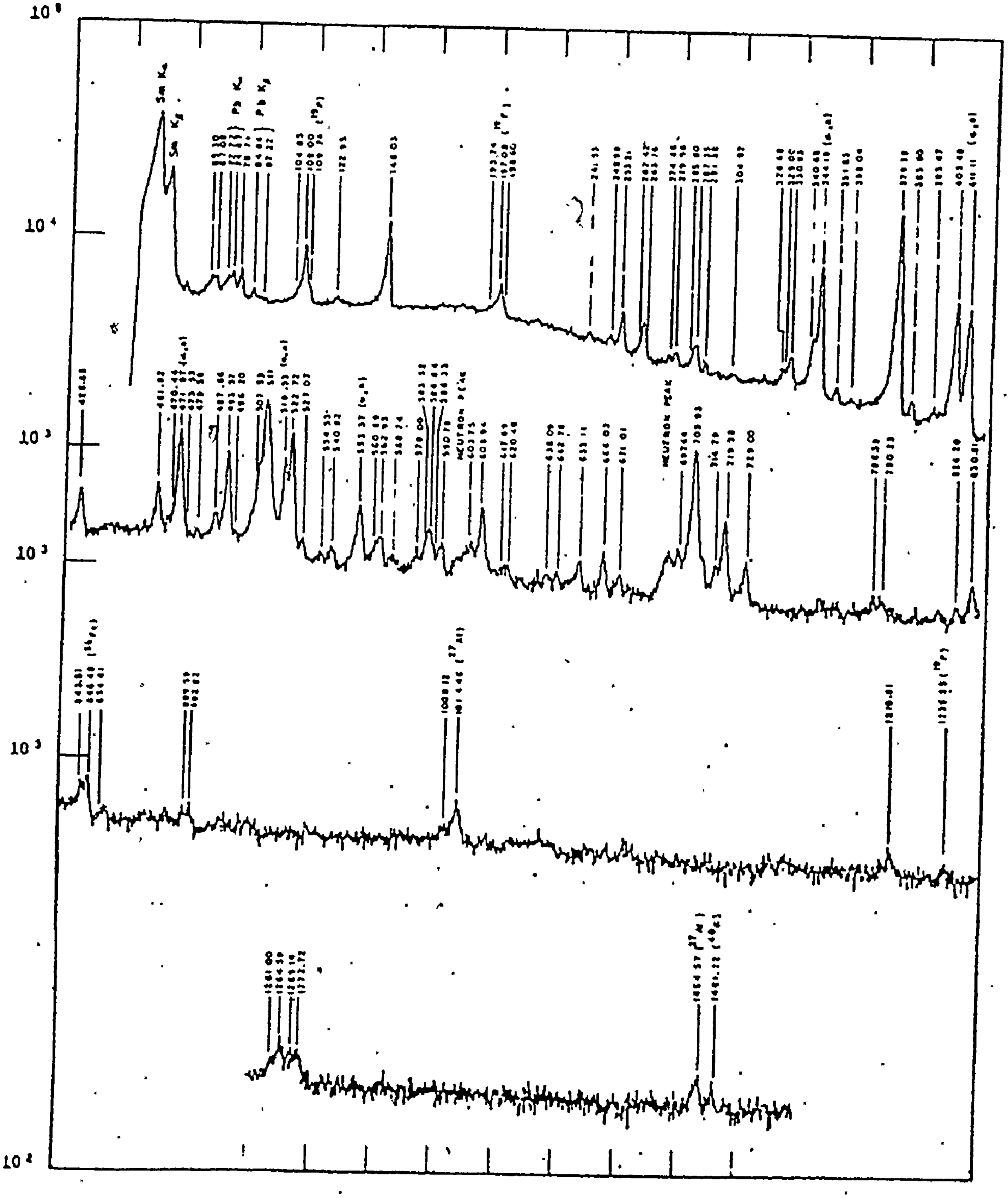

Figure 5-2

Gamma ray spectrum of ^{151}Gd as recorded with a 37 cm^3 Ge(Li) detector with a resolution of 2.6 keV at 1330 keV.

recorded with a 37cc Ge(Li) of somewhat poorer resolution. Transitions in ^{152}Gd and ^{151}Gd arising from the (α,n) and (α,2n) reactions are present in both spectra in addition to a number of impurity lines. In general the position has been taken that coincidence evidence is required before a transition is assigned to ^{151}Gd. A few exceptions to this rule have been made. The energies and intensities of transitions in ^{151}Gd are given in Table 5-1. These represent weighted averages of three separate determinations. The gamma ray intensities have been normalized to the value 100 for the 379 keV transition. Table 5-1 also presents the angular distribution coefficients and the place of each transition in the level scheme. The coincidence data showed that several transitons which appear to be single in the direct spectra are actually multiplets. In these cases the total intensity has been apportioned among the various components on the basis of coincidence probabilities. The agreement between the results from the 1cc and 37cc Ge(Li) spectra was particularly gratifying since in the latter spectra the program Jagspot was often required to unravel up to 10 partially resolved peaks. The tabulated errors in the gamma ray energies are those obtained from the program or ±0.04 keV, whichever is larger.

The errors in the measured intensities are approximately 10-15% for well resolved strong transitions although for weaker and partially resolved lines the errors may be much larger. These errors are a combination of the fitting errors from the program and a 10% allowance for the errors inherent in the efficiency curves. Errors due to

Table 5-1

EXPERIMENTAL								MODEL CALCULATIONS						
Eγ keV	Iγ	Classification	A_2 x100	A_4 x100	α_K (x 10^3)	Multipole	%(L+1) pole	$J_i \to J_f$	A_2 x100	A_4 x100	δ x100	%(L+1) pole		$(J^{\pi})_1$
65.30(4)	4.2(3)	785→719	+16(6)	+4(10)		E1[a]		$11/2\to9/2^-$	+17	+1	-27	6.7	Qu	$11/2^+$
67.08(4)	5.8(1)	852→785	-19(11)	+17(15)		M1[a]		$13/2\to11/2^+$	-7	+0.3	-10	1.1	Qu	$13/2^+$
78.71(4)	9.1(1)	785→706	+6.9(5)	+1.0(7)[a]		E1[a]		$11/2\to11/2^-$	+8	-3	+46	18	Qu	$11/2^+$
88.96(23)	0.15(4)													
108.00(4)	11.0(4)	108→0	+5.2(9)	+9.3(9)	1036[c]	M1E2	85(50,100)	$5/2\to7/2^-$	+10	+0	+170	75.0	Qu	$5/2^-$
121.70(6)	0.3(1)													
146.03(4)	16.0(2)	852→706	-20.2(7)	+4.9(9)				$13/2\to11/2^-$	-18	0	-3	0.09	Qu	$13/2^+$
147.1(2)[d]	1.4(3)	1511→1364												
180.13	0.69(4)	575→395	+0(10)	+14(12)	289[c]	M1E2	40(10,70)	$1/2\to3/2^-$	0	0				$1/2^-$
191.65(13)	0.31(6)	587→395			238[c]	M1E2	40(0,80)							
193.74(8)	0.36(6)	589→395												
196.00(9)	0.5 (1)	902→706												
214.67(15)	0.6(2)	1116→902[e]	-17(8)	+10(10)				$13/2\to13/2^-$	-5	-10	+80	40	Qu	
229.59(7)	0.4(1)	1346→1116	+0(30)	-16(40)[f]				$17/2\to13/2^+$	-26	-19	+8	0.7	Oc	$17/2^-$
247.98(5)	1.0(1)	1364→1116	+15(13)	-13(17)	130(15)	M1E2	17(<42)	$15/2\to13/2^+$	+7	+1	-17	3.1	Qu	$15/2^+$
253.21(4)	6.6(1)	1463→1210	-57(2)	-1(2)	113(12)	M1E2	33(10,55)	$13/2\to11/2^-$	-57	+1	+23	5.0	Qu	$13/2^-$
262.42(4)	3.5(1)	1726→1463	-54(2)	+2(3)	128(13)	M1	<8	$15/2\to13/2^-$	-53	+1	+17	3.0	Qu	$15/2^-$
263.76(4)	5.1(1)	1116→852	+36(2)	-1(2)	125(13)	M1	<14	$13/2\to13/2^+$	+37	-0	+3	0.07	Qu	$13/2^+$
266.61(11)	0.4(1)	-												
271.17(24)	0.7(1)	379→108	-2(28)	+14(28)				$9/2\to5/2^-$	+21	-8	+9	0.8	Oc	$9/2^-$
274.66(13)	0.4(1)	671→395												
277.96(5)	2.0(1)	2004→1726			110(15)	M1	<16	$17/2\to15/2^-$						$17/2^-$
287.35(4)	3.9(1)	395→108	+6(2)	+4(2)	86(9)	M1E2	17(<40)	$3/2\to5/2^-$	+5	+0	+4	41	Qu	$3/2^-$
291.38(8)	1.3(1)	2295→2004	-54(6)	+6(8)	110(20)	M1	<2	$19/2\to17/2^-$	-50	+1	+13	1.7	Qu	$19/2^-$
296.66(8)	0.7(1)													

EXPERIMENTAL								MODEL	CALCULATIONS				
Eγ keV	Iγ	Classification	A_2 x100	A_4 x100	α_K ($\times 10^3$)	Multipole	%(L+1) pole	$J_i \to J_f$	A_2 x100	A_4 x100	δ x100	%(L+1) pole	$(J^\pi)_i$
304.92(8)	0.8(1)	2600→2295	-12(41)	-48(59)[f]				$21/2\to19/2^-$	+11	+2	-19	4 Qu	$21/2^-$
315.09(12)	0.4(1)	2915→2600	-1(14)	-20(20)				$23/2\to21/2^-$	-4	+1	-12	1.5 Qu	$23/2^-$
318.76(7)	1.1(1)	427→108	+4(10)	-9(11)	9(3)[c]	M1E2	0(<50)	$5/2\to5/2^-$	-0.3	-0.1	+40	15 Qu	5/2
326.68(18)	0.9(2)	(706→379)			51(20)	M1E2	50(0,100)						
330.93(4)	4.3(2)	1116→785	-51(4)	-0(4)	70(15)	M1	<26E2	$13/2\to11/2^+$	-52	+1	+20	3.9 Qu	$13/2^+$
331.1(1)[d]	0.5(2)	1677→1346											
340.65(4)	6.2(2)	1852→1511	-27(5)	+4(6)	10(2)	E1	<1M2	$19/2\to17/2^-$	-26	0	-1.7	0.03 Qu	$19/2^+$
345(1)[d]	2.0(5)	2197→1852											
346.58(14)	0.9(2)	1511→1164[g]	+24(20)	-13(30)				$17/2^-\to13/2$	26	-19	+8.7	0.7 Oc	$13/2^-$[a]
358.04(9)	1.3(2)	1210→852	-0(20)	+4(22)	<9	E1	<1M2	$11/2\to13/2^+$	+1.1	+0.1	+13	1.7 Qu	$11/2^-$
379 (1)[d]	~1.0	1164→785[g]											
379.39(4)	100.0(4)	379→0	-9.1(4)	+1.4(5)	44(4)	M1	0(<20)	$9/2\to7/2^-$	-8.7	-0.1	-7.5	0.6 Qu	$9/2^-$
395.47(8)	1.4(2)	395→0			20(10)	M1E2	100(>52)						
397.44(15)	0.6(2)												
405.48(4)	35.6(1)	785→379	-20(1)	+3(1)	7.4(0.9)	E1M2	0.8(<1,5)	$11/2\to9/2^-$	-17	+0	-3.5	0.1 Qu	$11/2^+$
409.8(5)[d]	1.4(5)	1116→706											
426.65(4)	6.9(2)	427→0	-2(9)	-3(11)	41[c]	M1	<12E2	$5/2\to7/2^-$	+3	+0	0	0 Qu	$5/2^-$
461.92(4)	6.1(2)	1364→902	-19(2)	+7(3)	6(2)	E1M2	1.5(<4)	$15/2\to13/2^-$	-16	+0.1	-5	0.3 Qu	$15/2^+$
466.04(8)	1.3(2)	575→108			20[c]	M1E2	48(7,90)						
473.53(6)	4.3(3)	2325→1852	+36(6)	-12(8)	18(8)	M1E2	60(>0)	$23/2\to19/2^+$	+36	-11	0	0 Oc	$23/2^+$
476.46(19)	0.6(2)	585→108											
479.56(13)	1.0(3)	587→108			21[c]	M1E2	27(0,55)						
480.38(22)	0.7(3)	589→108											
483.42(15)	1.2(3)				15(7)	M1E2	80(>15)						
487.77(6)	5.1(3)	1852→1364	+35(4)	-2(5)	13(4)	M1E2	95(>38)	$19/2\to15/2^+$	+41	-9	-3.5	0.1 Oc	$19/2^+$

EXPERIMENTAL								MODEL CALCULATIONS						
E_γ keV	I_γ	Classification	A_2 x100	A_4 x100	α_K ($\times10^3$)	Multipole	%(L+1) pole	$J_i\to J_f$	A_2 x100	A_4 x100	δ x100	%(L+1) pole		$(J^\pi)_i$
493.57(6)	25.6(3)	1346→852	+35(1)	-11(1)	14(2)	M1E2	80(60,100)	$17/2\to13/2^+$	+36	-11	0	0	Oc	$17/2^+$
496.20(22)	1.3(3)													
504.43(18)	1.5(6)	1210→706	+58(39)	+27(47)[f]	12(7)	M1E2	90(>20)	$11/2\to11/2^-$	+39	-1	-27	7	Qu	$11/2^-$
506.08(15)[d]	3(1)	1852→1346												
507.53(4)	9.6(5)	1853→1346	+7(8)	-34(10)[f]	10(2)	M1E2	(>90)	$21/2\to17/2^+$	+7	-35	+27	7	Oc	$21/2^+$
512.20(20)[d]	2.4(9)	1364→852			8(3)	M1E2	(>98)							
515.1(4)	1.1(5)	1726→1210												
520(1)[d]	1.0(5)	2197→1677												
522.77(4)	39.2(4)	902→379	+30(1)	-2(1)	11.0(1.5)	M1E2	91(>76)	$13/2\to9/2^-$	+34	-9	0	0	Oc	$13/2^-$
528.78(28)	0.9(2)													
✓ 540.82(10)	1.9(3)	2004→1463	26(26)	-19(33)[f]				$17/2\to13/2^-$	+26	+19	+8	0.6	Oc	$17/2^-$
✓ 552.4(5)[d]	2.3(5)	2406→1853	+7(22)	-30(33)[f]				$25/2\to21/2^+$	+5	-36	+29	8	Oc	$25/2^+$
✓ 560.89(7)	3.5(3)	1677→1116	-31(17)	-11(21)[f]	8(3)	M1E2	100(>69)	$17/2\to13/2^+$	+30	-16	+7	0.5	Oc	$17/2^+$
562.93(7)	5.0(3)	671→108	-28(27)	-32(35)[f]	13(4)	M1E2	43(0,90)	$7/2\to5/2$	-25	+0	+13	1.7	Qu	$7/2^-$
568.74(15)	1.6(5)	2295→1726			20(10)	M1E2	<75							$19/2^-$
579.08(10)	3.5(3)	1364→785	+41(37)	-9(34)[f]				$15/2\to11/2^+$	+43	-5	-8	0.6	Qu	$15/2^+$
583.52(11)	3.5(4)	1435→852	+14(7)	-16(9)				$15/2\to13/2^+$	+7	+1	-17	3	Qu	$15/2^-$
584.84(12)	4.9(4)	585→0	-16(6)	+5(7)				$9/2\to7/2^-$	-15	0	-5	0.3	Qu	$9/2^{\pm}$, $7/2^-$, 5/
589.19(18)	1.8(4)	589→0												
596.66(16)	1.4(2)	2600→2004												
603.75(14)	2.5(4)	1506→902	-7(39)	+26(49)[f]				$15/2\to13/2$	-22	0	0	0	Qu	$11/2^{\pm}$ $13/2^-$,1
✓ 608.94(4)	15.6(3)	1511→902	+26(1)	+2(2)	7(2)	M1E2	98(>70)	$17/2\to13/2^-$	+32	-14	+1.7	0.03	Oc	$17/2^-$
617.89(12)	1.3(2)	618→0	+34(13)	+13(17)	12(3)	M1E2	17(0,65)	~~$5/2\to7/2^-$~~	+13	0	+84	40	Qu	$5/2^-$
								~~$7/2\to7/2$~~	+28	-1	-40	14	Qu	$(7/2^-)$

EXPERIMENTAL								MODEL CALCULATIONS					
E_γ keV	I_γ	Classification	λ_2 x100	λ_4 x100	α_K (x 10^3)	Multipole	%(L+1) pole	$J_i \to J_f$	λ_2 x100	λ_4 x100	δ x100	%(L+1)-pole	$(J^\pi)_i$
620.48(16)	1.8(4)	2915→2295	+62(32)	±63(37)^f	7(3)	M1E2	94(>50)	23/2→19/2$^-$	37	-12	0		
638.09(12)	1.5(5)	3237→2600	+16(42)	+0(50)^f				25/2→21/2$^-$	+6	-35	+27	7	∝ 25/2$^-$
✓ 642.78(10)	2.5(3)	2078→1435	+22(28)	-16(39)^f				19/2→15/2$^-$	18	-26	+16	2.5	∝ 19/2$^-$
671.01(11)	2.5(4)	671→0	+6(32)	+24(43)^f				7/2→7/2$^-$	-7	-1	+70	33	∝ (7/2$^-$)
697.64(11)	5.3(6)	1077→379	+38(36)	-12(48)^f	5(2)	M1E2	100(>60)	13/2→9/2$^-$	+41	-5	-8	0.6	∝ 13/2$^-$
✓ 705.93(4)	46.5(4)	706→0	+25(1)	-3(1)	5.2(1.0)	M1E2	95(>70)	11/2→7/2$^-$	+28	-9	+1.7	0.03	∝ 11/2$^-$
✓ 719.38(5)	8.0(3)	719→0	-35(4)	+10(5)	5.2(1.1)	M1E2	90(>65)	9/2→7/2$^-$	-35	+10	300	92	∝ 9/2$^-$
719(1)^d	2.0	1425→706											
721.0(5)	2.2(9)	1506→785											
✓ 729.00(6)	6.8(3)	1435→706	+16(6)	+7(6)	5.2(1.1)	M1E2	85(>60)	15/2→11/2$^-$	+26	-3	+1.7	0.03	∝ 15/2$^-$
✓ 786.4(6)	0.5(1)	2297→1511	+35(10)	+24(11)				21/2→17/2$^-$	+54	+3	-18	3	∝ 21/2$^-$
824.2(4)	1.5(3)	1677→852											
✓ 830.81(14)	4.4(2)	1210→379	+12(7)	+25(8)				11/2→9/2$^-$	+16	+18	-630	97	∝ 11/2$^-$
835.2(3)	1.7(3)												
839.0(4)	1.6(3)												
854.6(5)	1.2(2)												
1210.8(4)	1.8(3)	1210→0	+30(8)	-6(2)^f				11/2→7/2$^-$	+28	-9	1.7	.03	∝ 11/2$^-$

a) Multipolarity from γ-γ coincidence measurements.

b) Peak poorly resolved from x-rays; angular distribution difficult to analyze.

c) Internal conversion data from Gonsior et al (1971) or Hammaren et al (1975).

d) Energy and intensity from γ-γ coincidence measurements.

e) Energy fit poor; classification doubtful.

f) Four point angular distribution.

g) The 347 - 379 keV coincidence data define a level at 1132 or 1164 keV depending on the order of the transitions. The evidence slightly favours the latter.

angular distribution effects are expected to be negligible since the spectra were recorded at 55° to the beam direction where the value of $P_2(\cos\theta)$ vanishes. Furthermore the solid angle subtended by the detector at the target was large enough to smear out a large part of the anisotropy.

A number of lines in the spectra of Figs. 5-1 and 5-2 are due to impurities or other competing reactions. The stronger of these have been labelled. There will of course be other impurity lines which we have been unable to distinguish from those originating in ^{151}Gd. A more detailed discussion of these contaminants follows in section 5.4.

5.3 Excitation Functions

Excitation functions were determined in order to distinguish between gamma rays originating in the (α,n) and $(\alpha,2n)$ reactions. Two sets of excitation data were obtained, a three point excitation curve for gamma rays up to 730 keV using the 1cc Ge(Li) detector and a four point excitation curve for gamma rays up to 1.5 MeV using a 37cc detector. A spectrum was also accumulated at a beam energy of 15 MeV, which is below the $(\alpha,2n)$ threshold, in order to aid in the identification of impurity lines. Fig. 5-3 presents excitation curves for a number of prominent transitions in the spectrum. Each experimental point represents a ratio of the intensity of the gamma ray to that of the 108 keV transition in the same spectrum.

In agreement with the expectations of the statistical theory, it

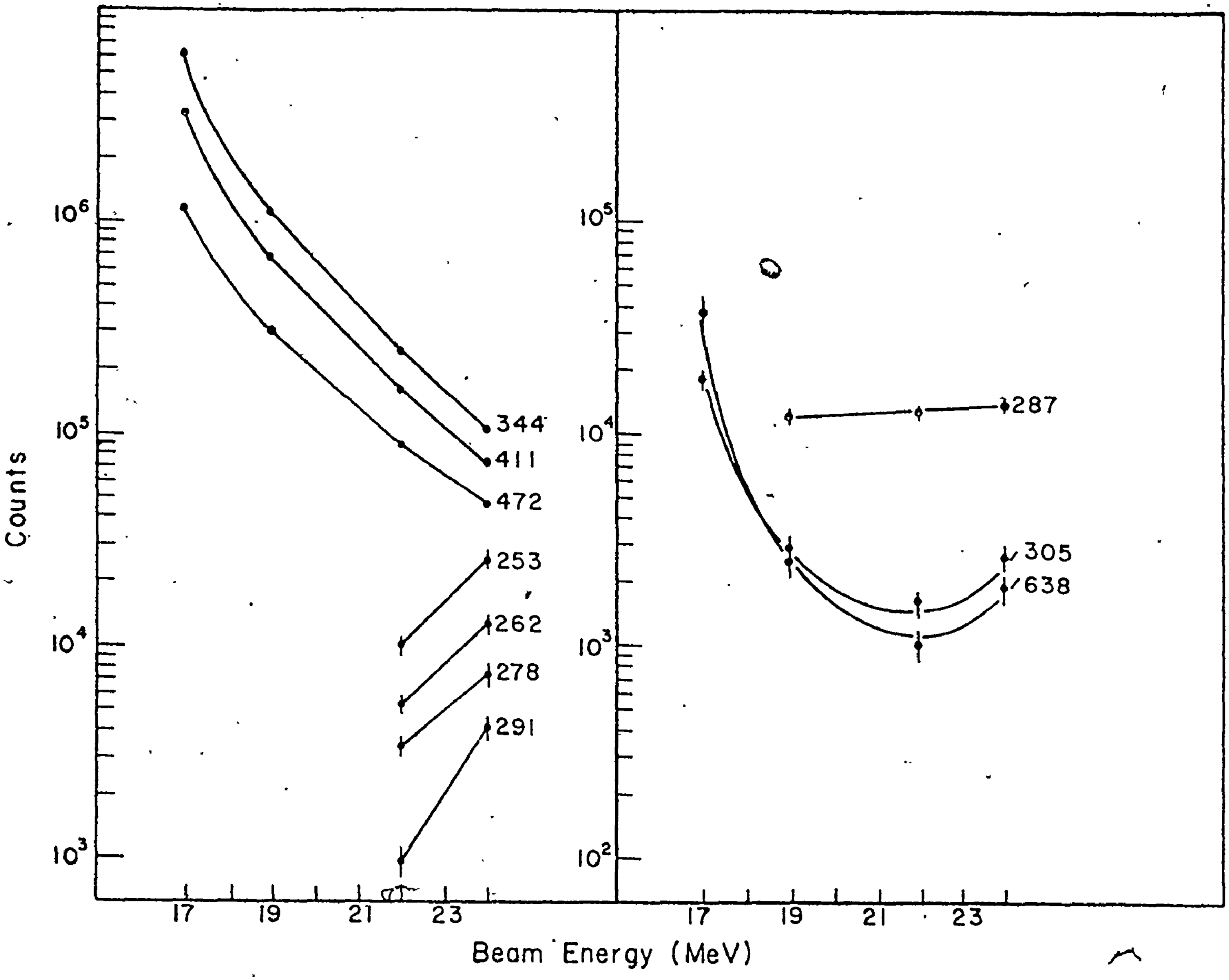

Figure 5-3

Excitation curves for a number of prominent gamma rays in the spectrum.

is evident that the higher the spin of a state the more rapidly its yield increases with alpha energy. However, since the yield curves are not completely determined by the statistical theory, the shape of the excitation curve can only be used as a rough guide to the spin. Within a given rotational band the excitation curves offer an additional check on the ordering of the members. This shows somewhat in the increase in slope of the excitation curves as one proceeds up the $11/2^-$ band via the 253, 262, 278 and 291 keV transitions.

The negative slopes of the excitation curves for the 344, 411 and 472 keV transitions of the g.s.b. of ^{152}Gd are typical of gamma rays from the (α,n) reaction. The gentle slope of the 287 keV gamma ray illustrates the slow increase in yield typical of transitions between low spin states. The peculiar excitation curves for the 305 and 638 keV transitions indicate that these gamma rays are present in both the (α,n) and $(\alpha,2n)$ reactions. For the transitions between high spin states (>9/2) the yields at 17 and 19 MeV were in general so small that they could not be detected.

5.4 Contaminant Lines

At a beam energy of 24 MeV the ^{149}Sm$(\alpha,n)^{152}$Gd and ^{149}Sm$(\alpha,2n)^{151}$Gd reactions compete strongly. In fact, the lowest member of the ^{152}Gd ground state band at 344 keV is 35% of the intensity of the 379 keV ground state transition in ^{151}Gd. Thus ^{152}Gd is a major contaminant in these experiments. An analysis of coincidence gates set on its ground state transitions was used to pick out the transitions associated

Table 5-2

Gamma Rays Identified as Impurities

Energy (keV)	Relative Intensity	Origin	Energy (keV)	Relative Intensity	Origin
53.41 ± 0.06	0.4	AuK$_{\alpha 1}$	283.20 ± 0.29	0.20	
68.84 ± 0.05	0.3		285.80 ± 0.11	2.00	^{149}Sm
72.72 ± 0.04	2.35	PbK$_{\alpha 2}$	327.39 ± 0.50	0.70	^{153}Gd, ^{149}Sm
74.87 ± 0.04	4.28	PbK$_{\alpha 1}$	329.00 ± 0.08	0.93	
84.84 ± 0.06	1.37	PbK$_{\beta 1}$	344.18 ± 0.05	34.8	^{152}Gd
87.22 ± 0.06	0.52	PbK$_{\beta 2}$	351.63 ± 0.07	1.9	^{152}Gd, ^{149}Gd
89.67 ± 0.12	0.9	^{149}Sm	385.80 ± 0.12	3.18	^{152}Gd
98.11 ± 0.14	0.1		393.81 ± 0.21	0.40	
104.85 ± 0.05	0.42	†	411.11 ± 0.07	31.5	^{152}Gd
109.74 ± 0.05	2.70	^{19}F(n,n')	440.02 ± 0.13	0.81	
122.95 ± 0.03	0.96	^{154}Gd	451.42 ± 0.15	0.89	
125.52 ± 0.08	0.27	^{149}Sm	461.92 ± 0.04	3.1	^{149}Sm
136.05 ± 0.05	0.06		470.44 ± 0.18	2.44	
138.60 ± 0.05	0.10		471.97 ± 0.06	24.1	^{152}Gd
153.54 ± 0.06	0.90		511.0 ± 0.1	28.7	$e^{+}e$
158.96 ± 0.11	0.15		514.31 ± 0.34	1.9	^{152}Gd
160.29 ± 0.09	0.16		519.53 ± 0.07	15.1	^{152}Gd
165.16 ± 0.11	0.16	^{149}Gd	527.07 ± 0.33	1.59	^{152}Gd
170.44 ± 0.06	0.37	^{153}Gd	553.37 ± 0.15	∿11	^{152}Gd
174.78 ± 0.14	0.15	^{153}Gd	557.39 ± 0.41	0.5	^{152}Gd
183.76 ± 0.06	0.39	^{153}Gd	558.32 ± 0.32	1.0	^{149}Sm, ^{154}Gd
197.08 ± 0.08	6.07	^{19}F(n,n')	586.33 ± 0.32	2.67	^{152}Gd
198.60 ± 0.11	1.17	^{149}Sm	590.73 ± 0.12	3.7	^{149}Sm
218.79 ± 0.11	0.32		597		^{74}Ge(n,n')
220.69 ± 0.15	0.25		611.10 ± 0.30	1.3	^{149}Sm
231.91 ± 0.10	0.33		653.11 ± 0.10	3.51	^{152}Gd
241.53 ± 0.09	0.44		664.02 ± 0.06	4.63	^{149}Sm
243.24 ± 0.14	0.17	†	714.79 ± 0.10	2.3	†
282.19 ± 0.10	0.37				

Table 5-2 (continued)

Energy (keV)	Relative Intensity	Origin
717.20 ± 0.15	0.87	
790.23 ± 0.42	0.62	
843.51 ± 0.22	1.24	^{27}Al(n,n') (α,α')
846.48 ± 0.13	2.07	^{56}Fe(n,n') (α,α')
889.59 ± 0.48	1.14	
892.82 ± 0.35	1.85	^{154}Gd
1008.12 ± 0.75	0.96	^{154}Gd
1014.41 ± 0.19	4.22	^{27}Al(n,n') (α,α')
1235.55 ± 0.44	1.16	^{19}F(n,n')
1261.00 ± 0.84	0.89	†
1264.59 ± 0.26	3.23	†
1269.14 ± 0.40	2.00	†
1272.72 ± 0.27	3.01	†
1454.57 ± 0.23	2.22	^{27}Al(α,n)
1461.22 ± 0.34	1.43	^{40}K

† These transitions are seen in the 15 MeV spectrum below the (α,2n) threshold. As such these lines are regarded as impurities of unknown origin. All other lines which do not have a designated origin are included as impurities as a result of the criterion that they were not observed in coincidence with a line known to belong to ^{151}Gd.

with this nuclide. Because several of the strong ^{152}Gd transitions are very close in energy to ^{151}Gd gamma rays, the ^{152}Gd contaminant was somewhat troublesome in the analysis.

Isotopic impurities in the target led to weak activities due to ^{153}Gd and ^{154}Gd. Some of the weaker lines observed could be attributed to these nuclei on the basis of previous work carried out in other laboratories.

Contaminant lines from the (α,n) and (α,α') reactions on the aluminum and iron of the beam line and target chamber were easily identified since they are always present. Included among these are the well known 'oddly' shaped peaks at 597 keV and 693 keV arising from the (n,n') reaction on germanium. These were present in all the singles

The 110, 197 and 1235 keV lines are due to ^{19}F produced by the ^{19}F(n,n') reaction on the teflon in the Ge(Li) detector mounting and by the ^{16}O(α,n) reaction on the oxygen which has oxidized the surface of the target.

the teflon in the Ge(Li) detector mounting.

Coulomb excitation of the ^{149}Sm target also creates a number of lines. Since this nucleus is presently under study at McMaster it was easy to identify the lines from this reaction.

The energies and intensities of the observed impurity lines are listed in Table 5-2. Some of the weaker gamma rays in this table may well turn out to be due to ^{151}Gd.

5.5 Gamma-Gamma Coincidence Results

A small sample of the coincidence spectra associated with the gates studied in the present work are presented in Figs. 5-4 to 5-9. These will serve to illustrate the quality of the data and support the major features of the decay scheme. As described earlier each gate shows the spectrum in one detector in coincidence with a full energy peak in the other after contributions from chance and from the Compton distributions of other gamma rays in the gate have been subtracted. The rather large background in some of these spectra is created by true coincidences with the Compton distributions of the many unresolved high energy gamma rays which deexcite high lying states populated in the reaction. Partial level schemes have been attached to each figure to aid the reader in interpreting the spectra.

Table 5-3 presents the coincidence probabilities derived from the analysis of the coincidence spectra. In this table, the first two columns present the energies E_i and E_j involved in a coincidence, the following two columns give the coincidence probabilities C_{ij} and C_{ji} derived from the spectra where E_i and E_j were the gating transitions. One expects $C_{ij} = C_{ji}$ within the limits of experimental error. The final column gives the value of C_{ij} expected from the proposed level structure. For weaker transitions, it was not always possible to determine both C_{ij} and C_{ji}. The coincidence probabilities generally agree within ∿30% and discrepancies of the order of 100% or more for well defined lines have to be taken as serious indications of inadequacy of the level structure.

Table 5-3

Coincidence Probabilities for Gamma Rays in ^{151}Gd

E_i (keV)	E_j	C_{ij}	C_{ji}	$C_{expected}$
108	180	0.16		0.25
	192	0.16		0.11
	263	∿0.1	∿0.15	
	287	1.0	1.0	1.4
	512	0.5		
	563	0.9	0.25	1.8
146	253	0.3	0.15	0.26
	262.4	1.6	1.4	0.17
	263.7			1.4
	358	0.2		0.35
	494	6.3	5.3	7.3
	507	2.8	2.3	3.4
	512	0.4		0.8
	520	∿0.3		∿0.1
	552	1.1	0.6	0.6
	561	0.6	0.3	0.6
	583.5	0.5	0.4	1.0
	706	12.7	9.2	16
147	341	0.3	0.9	0.4
	379	0.9	0.3	0.6
	462	0.6	0.6	0.6
	473	∿0.5	0.6	0.2
	523	0.35		0.6
180	287	0.5	0.6	0.7
192	287		0.3	0.3
214	561		0.37	0.24

Table 5-3 (continued)

E_i (keV)	E_j	C_{ij}	C_{ji}	$C_{expected}$	
230	331		0.4	0.2	
	380	0.4		0.4	
	406	0.1		0.1	
	506 + 507	0.1	0.3	0.2	
248	331	0.6	0.4	0.45	1364 1116
	347	0.6			
	379	0.1		0.28	
	406	0.3		0.28	
	488	0.2		0.25	
253	262	3.8	3.7	3.5	
	278	1.9	1.0	1.5	
	291	1.3	0.7	1.1	
	305	0.4	0.6	0.6	
	315	0.25		0.3	
	358	0.5		0.8	
	379	4.9	4.4	4.0	
	406	1.0	0.6	0.6	
	504	1.1	1.0	1.0	
	541	1.0	1.3	1.9	
	569	0.8	0.6	1.2	
	706	1.1	1.0	1.1	
	830	4.0		3.6	
	1210	0.9		1.1	
262.4	278	1.0	1.0	1.5	
	291	0.3	0.5	0.5	
	305	0.1	0.2	0.4	
	315	0.3		0.2	
	358	0.2		0.4	

Table 5-3 (continued)

E_i (keV)	E_j	C_{ij}	C_{ji}	$C_{expected}$
262	379	5.7	4.4	4.5
	406	2.1	3.1	2.3
	504	0.3	0.5	0.5
	569	∿0.8	0.5	1.2
	597	0.4		0.5
	706	1.8	1.9	2.8
	830	2.2		1.9
	1210	0.5		0.6
264	341		0.4	0.5
	561	1.0	0.9	1.4
278	291	0.6	0.8	0.7
	305	0.15		0.2
	315	0.2		0.2
	379	1.3	1.0	1.2
	504		0.4	0.3
	597	0.3		0.7
	830	1.2		1.1
287	377	0.5	1.0	
291	379	0.7	1.0	0.8
	515	0.2		0.2
	541	0.4	0.4	0.6
305	315	∿0.2		0.15
	541		∿0.3	0.2
327	494		1.2	
331	379	4.7	4.5	3.3
	406	4.5	4.6	3.0
	494	0.47	1.2	0.47
	520	∿0.3		.1
	561	2.0	2.1	2.1
	706	1.9	1.4	1.2
	719	0.7	0.8	0.7

Table 5-3 (continued)

E_i (keV)	E_j	C_{ij}	C_{ji}	$C_{expected}$
341	345 347	2.0	0.5	1.0 0.3
	379	10.5	5.8	6.0
	406	1.8		0.3
	461	1.2		0.4
	473	1.6		2.1
	512	1.7	2.0	0.4
	523	4.9	5.2	5.1
	609	6.1	5.6	6.0
	706	1.8		0.2
	719	1.0		.1
345	488	0.6	0.4	0.5
347	379	3.7	1	2.0
	406	$\sim$1.0	1.2	1.0
	705	0.5		0.3
	719	0.2		0.1
358	406		0.8	0.6
379	406	40	44	36
	462	9.1	9.1	9.2
	473	3.8	4.5	4.3
	488	4.6	2.3	3.8
	494	10.7	9.2	12.0
	506	2.2		$\sim$3
	508	6.2	5.4	4.9
	512	2.6	2.8	1.5
	523	39	43	39
	541		1.1	1.0
	552	1.0		1.0
	561	1.8	1.7	1.8

Table 5-3 (continued)

E_i (keV)	E_j	C_{ij}	C_{ji}	$C_{expected}$
379 (con'd)	569	0.7		0.8
	579	1.4	3.3	2.2
	604	2.5	2.3	2.5
	609	13	16	16
	620	0.8	∿1.3	1.0
	638		1.5	
	643	0.8	∿1.1	
	697	3.8	2.5	5.3
	721	1.4	1.5	1.4
	786	1.3	2.7	0.5
	790			0.6
	824	1.2		
	830	4.2		5.4
	839	1.6		
	854	1.5		
406	488	1.6	0.9	1.9
	494	9.0	10.4	12.0
	506	1.2	5.1	1.3
	508	3.5		4.4
	512	1.0	1.2	1.1
	552	1.0	1.1	1.0
	561	2.8	2.1	1.8
	579	2.3	2.5	2.2
	638		0.5	0.3
	721	∿1.0	1.7	1.4
462	473	1.7	1.2	0.8
	488	2.1	1.5	2.2
	523	7.6	9.6	6.1

Table 5-3 (continued)

E_i (keV)	E_j	C_{ij}	C_{ji}	$C_{expected}$
473	488	1.0	0.7	1.4
	506	1.1		1.1
	523	1.5	1.2	1.7
	609	0.9	1.6	1.1
488	512	1.2		1.0
	523	1.5	0.9	2.2
	579	0.4	0.8	1.3
	706	0.3	0.6	0.4
494	508	6.2	5.4	10
	552	1.3	1.1	2.0
	706	6.0	6.1	7.4
	719	2.1	2.0	2.6
504	706	1.0	1.0	1.5
508	553	1.6	2.1	2.0
	706	2.6	3.7	2.5
	719		1.0	1.0
520	561	1.1	0.8	1.0
	604	1.8	2.2	2.5
	609	11.8	12.3	15.6
	786	1.0	1.4	1.8
561	410	0.5	1.1	0.6
	706	0.8	1.2	0.8
579	706	0.9		0.7

Table 5-3 (continued)

E_i (keV)	E_j	C_{ij}	C_{ji}	$C_{expected}$
609	786	0.9	$\sim$1	0.5
638	706	0.6	1.4	
643	729	$\sim$1.0	1.7	2.5
706	719	1.9	2.5	$\sim$2
	729	3.9	3.5	6.8
719	721	0.15	0.15	0.3

Fig. 5-4 shows gates set on the 253 and 262 keV transitions, the two lowest members of the band based on the 1210.8 keV state. The level structure of Fig. 5-4 could equally well have been established by several other choices of gates. The bandhead at 1210.8 keV deexcites by four transitions, the two strongest of which are the 830.8 and 1210.8 keV gamma rays. The coincidence probabilities derived from these spectra are in excellent agreement with those expected from the singles intensities and the postulated band structure. The coincidence evidence for the 2600 keV state is relatively weak in these spectra. However, it is much stronger in the (α,3n) measurements of Kleinheinz et al. (1974) who were able to transfer more angular momentum to their target than was possible for us in the (α,2n) reaction.

The spectrum in coincidence with the 830 keV gate shown in Fig. 5-4 was recorded in an early experiment and cannot be directly compared with the other spectra shown. In this experiment, an electronic failure made the spectra unreliable for the purpose of determining coincidence probabilities. Nevertheless, it demonstrates unequivocally that the bandhead is located at 1210 keV.

The 262 keV gated coincidence spectrum provides clear evidence that the 262 keV peak is a doublet. In this spectrum the 146 and 706 keV transitions are not only much stronger than in the 253 keV gate but are much too intense to be supported by the 358 keV transition which connects the bandhead to the 852 keV level. Analysis shows that ∿40% of the multiplet intensity belongs to the band member. The location of the second component in the level structure is clearly

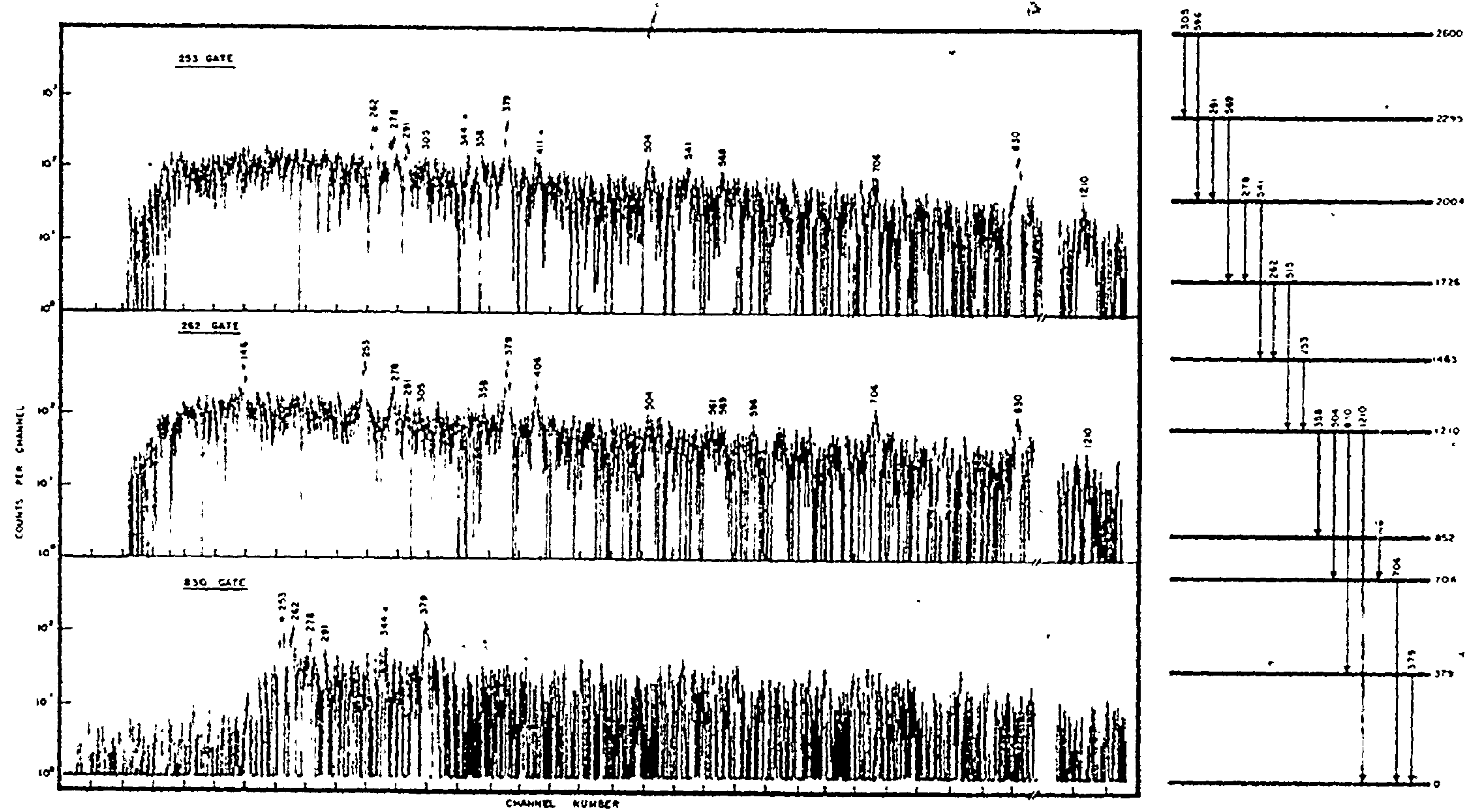

Spectra in coincidence with the 253.2,262.4+263.8 and 830.8 keV gates. These illustrate the structure of the 11/2$^-$[505] band and its connection to lower lying states.. The role of the 263.8 keV state is illustrated in the partial level scheme of Figure 5-5.

revealed in Fig. 5-5.

Fig. 5-5 presents the 331 and 561 + 563 keV gated spectra. The partial decay scheme shows all the transitions present in the 331 and 561 keV gated spectra but does not show those associated with the 563 keV component of the latter spectrum. The 563 keV gamma ray is responsible for the 108 keV peak. The three low energy transitions (below 80 keV) do not appear because of the poor efficiency of the coincidence circuit for these energies. The 523 keV peak in the 561 + 563 keV gate has not been explained. Although the existence of the 410 keV peak in the 561 gate is marginal, much stronger evidence is found in the 411 keV gate. This gate which brings up the ground state band of ^{152}Gd is not shown.

The coincidence data suggest that the 1116 keV state is a doublet. The intensities of the 561-410, 561-263 and 561-331 keV cascades (see Table 5-3) account for ~40% of the 263 keV singles intensity. The balance has been accounted for through the 341-395-263 keV cascade as shown in Fig. 5-6 and the coincidence probabilities of Table 5-3.

The 462 and 609 keV gated spectra support the partial decay scheme of Fig. 5-6, with most of the intensity associated with the 341-609-523-379 or the 473-488-462-523-379 keV cascades. The 286 keV peak in the 462 keV gate is due to Coulomb excitation of the ^{149}Sm target. The 496 keV peak in the 609 keV gate is unaccounted for.

The 341 keV gated spectrum shows the features expected from the cascades indicated above but it also contains several unexplained features. The 341 keV transition is only partially resolved from the much

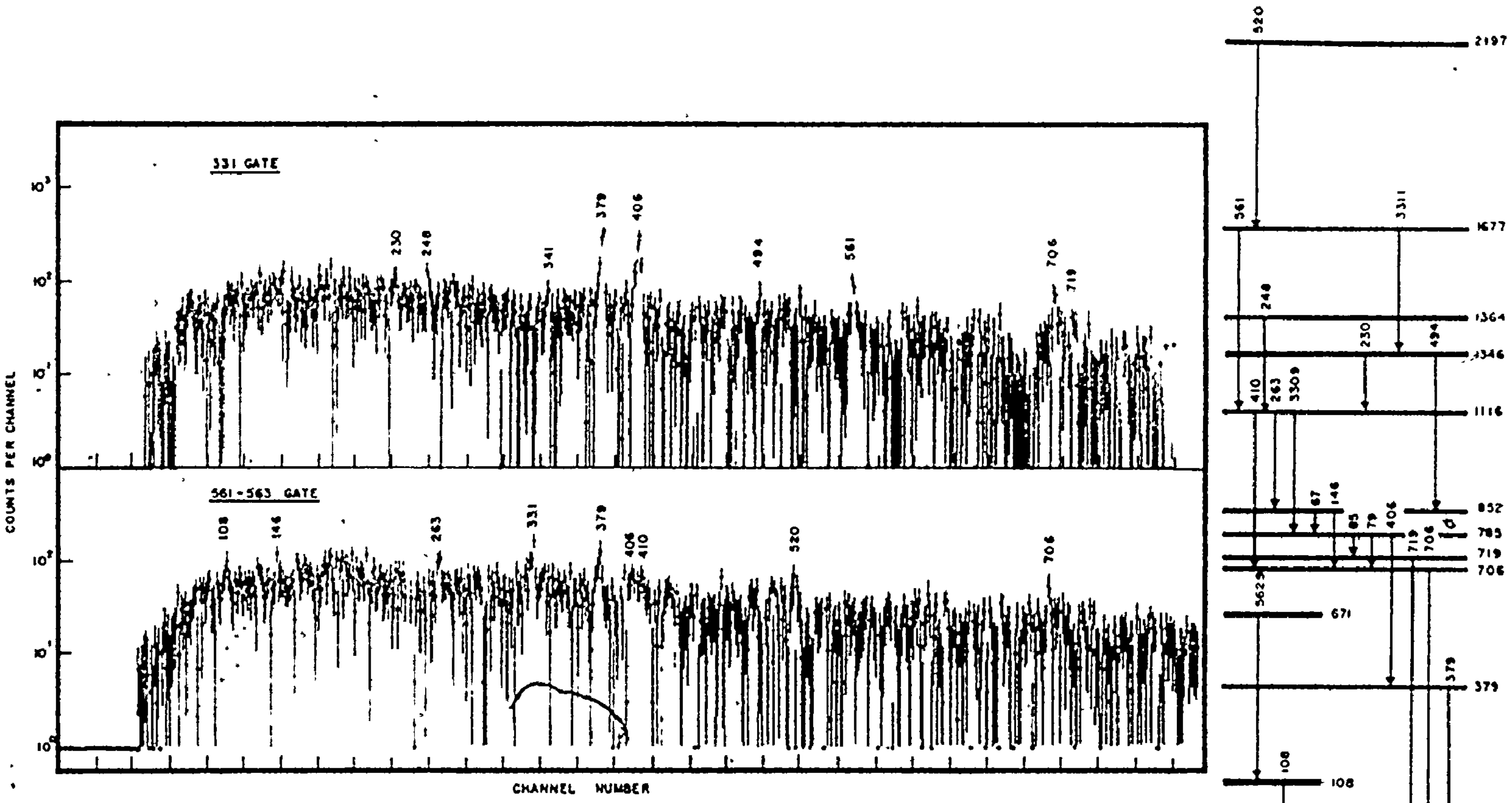

Figure 5-5

Spectra in coincidence with the 330.9+331.1 and the 560.9+562.9 keV transitions.

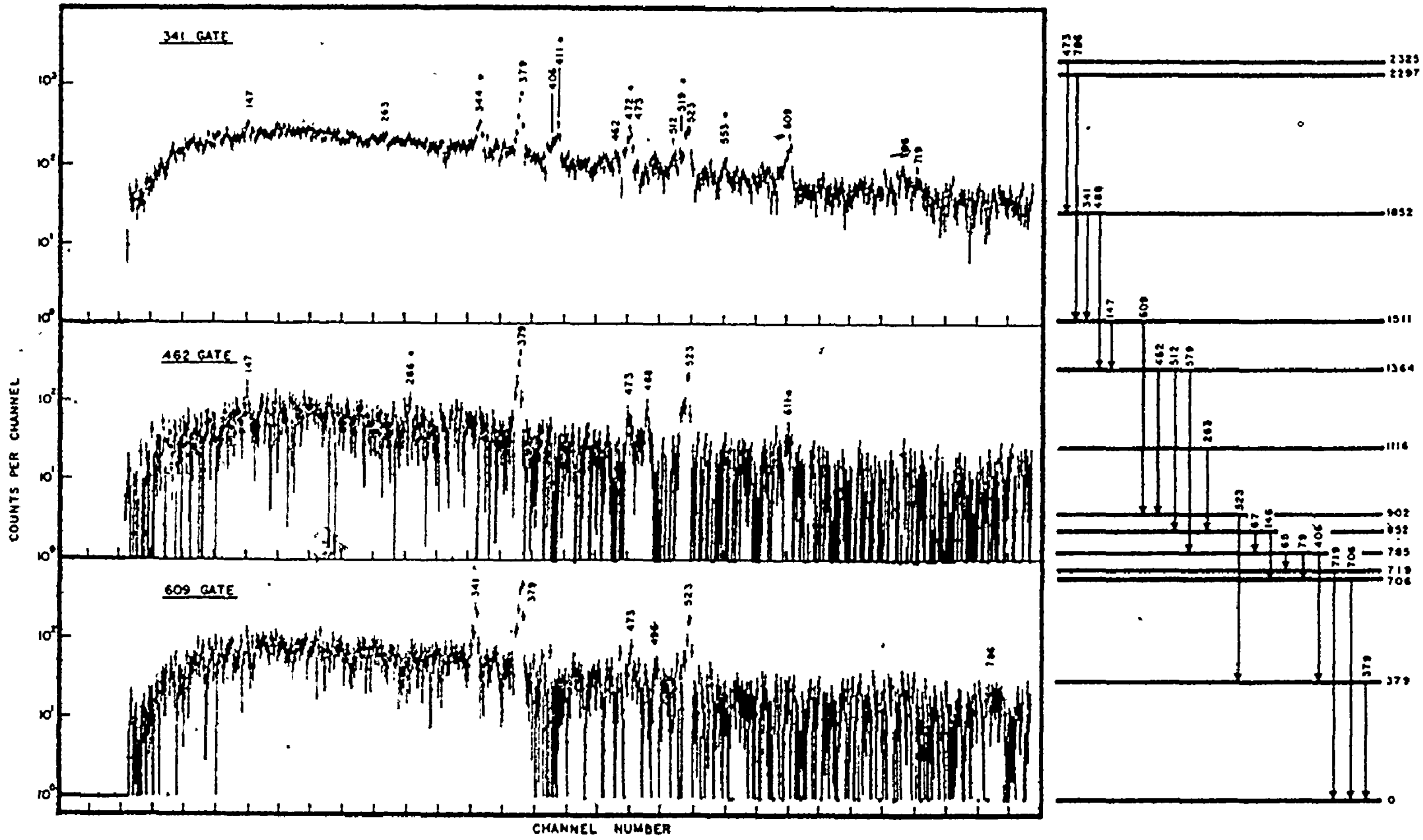

Figure 5-6

Spectra in coincidence with the 340.6,461.9 and608.9 keV transitions.

stronger 344 keV gamma ray in the ground state band of ^{152}Gd. This component in the gate is responsible for the 411, 472, 519 and 553 keV peaks in the spectrum. The 344 keV peak is inexplicably strong and gives a C_{ij} much greater than that seen in the reverse gate. The strengths of the 379, 406, 462, 512, 706 and 719 keV peaks are also unexpectedly strong, as shown in Table 5-3. The only serious discrepancies in Table 5-3 are related to the 341 keV and 344 keV transitions, and we do not feel very confident of our interpretation of some of the states related to this gate.

The 494 keV gate (see Fig. 5-7) shows a strong 552-507-494-67-406-379 keV cascade. The 552 keV transition is masked in the singles by the strong 552 keV transition in ^{152}Gd. The fact that it was much stronger in the measurements of Kleinheinz et al. which used the (α,3n) reaction supports its assignment as a transition involving high spin states.

The 146 keV transition is a doublet and the corresponding gate (Fig. 5-7) shows evidence of both components. The strong component brings up the 552-507-494-146-706 keV cascade. It also brings up the 358 keV transition from the 1209 keV state, the 248 keV and two 263 keV transitions. This γ-ray is also in coincidence with the 121-585 keV cascade. The weak component is in coincidence with peaks at 461, 523 and 379 keV. The 488 keV gate brings up only the peaks expected from the partial decay scheme.

The 719 keV gate (see Fig. 5-8) contains 3 transitions, the strong 719 keV gamma ray, a weak one of nominally the same energy and a third

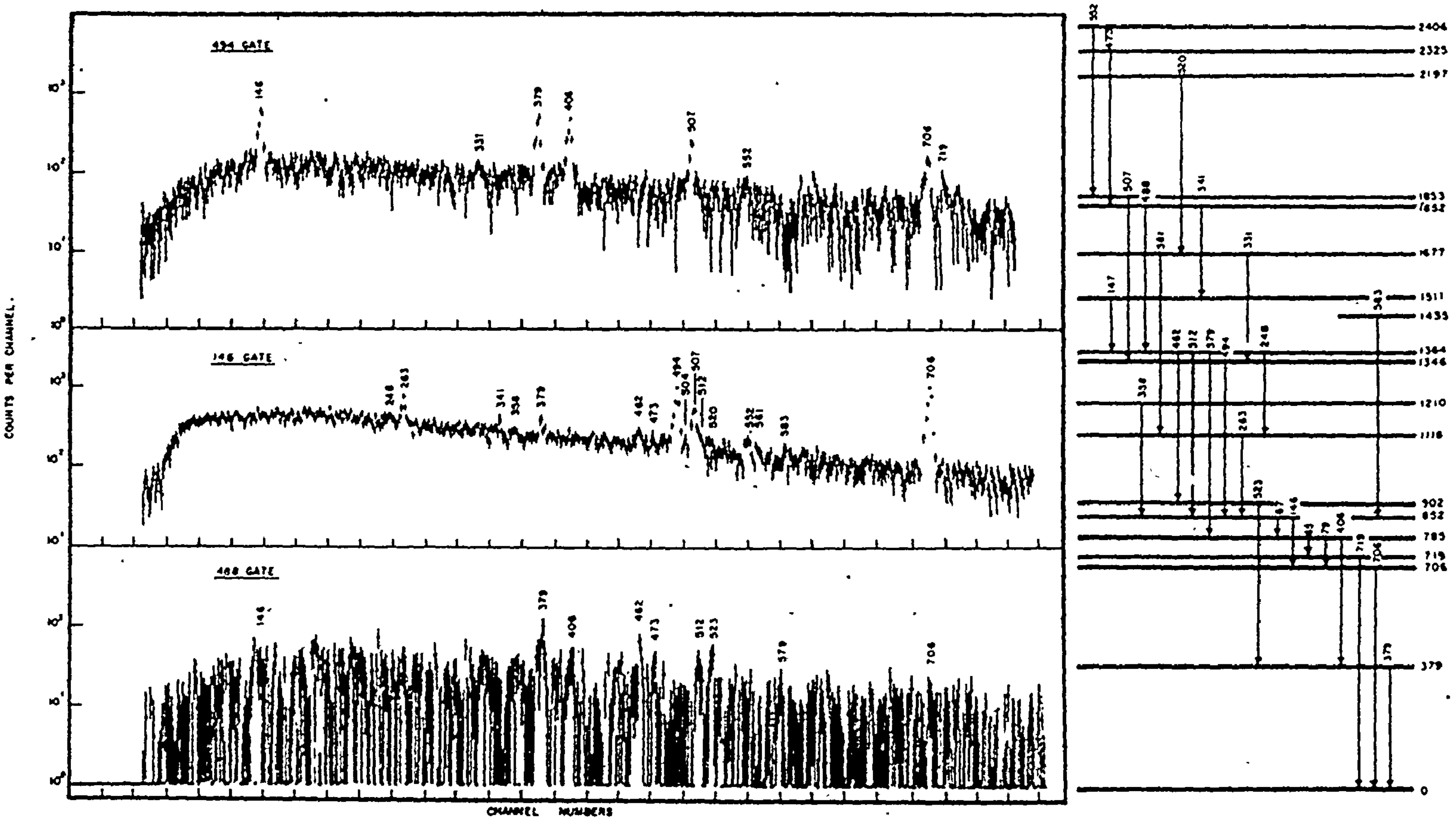

Figure 5-7

Spectra in coincidence with the 493.6,146.0+147.1 and 487.8 keV transitions.

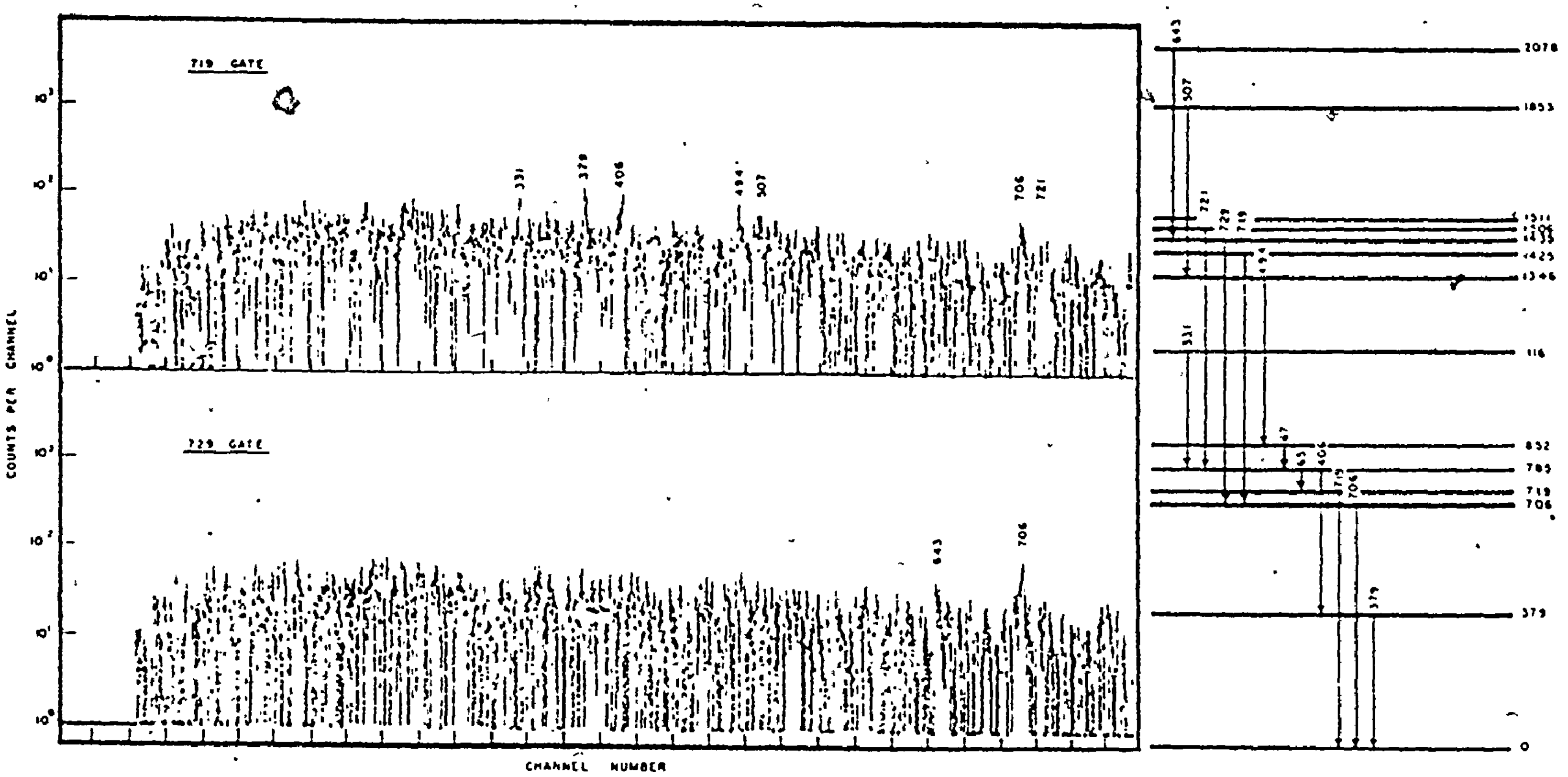

Figure 5-8

Spectra in coincidence with the 719.4 and 729 keV transitions.

whose energy must be 721 keV from energy fit. The strong 719 keV component is responsible for the peaks at 331, 494, 507 and 721 keV. The weak 719 keV line (intensity ∿2 from coincidence data) is responsible for the 706 keV peak. The 721 keV transition (intensity 2.2 from the coincidence data) accounts for the 379 and 406 keV peaks.

The 729 keV gate of Fig. 5-8 defines the 643-729-706 keV cascade.

The 406 keV gate (Fig. 5-9) brings up all the peaks from the level schemes with the coincidence probabilities expected. The coincidence probability for the 512-406 keV cascade was used to define the 512 keV intensity.

The 523 keV gate also contains some of the 579 keV transition in ^{152}Gd. This component brings up the 344, 411 part of the 473 and the weak 579 keV peak. The other peaks are all accounted for with the expected C_{ij} values.

The level scheme of Fig. 5-18 has been deduced from the data of Tables 5-1 and 5-3 in such a way as to require consistency on the part of both the energy fits and coincidence probabilities. The cases discussed below represent the exceptions to this rule.

Since the strong 426.7 and 584.8 keV do not produce any coincidences, we have assumed that they are the ground state transitions depopulating levels at 426.6 and 584.8 keV seen in the particle transfer experiments (Tjøm and Elbek, 1967 and Burke et al., 1975). The 617 keV state is identified in the same way but since the de-exciting transition is much weaker, the assignment is less secure.

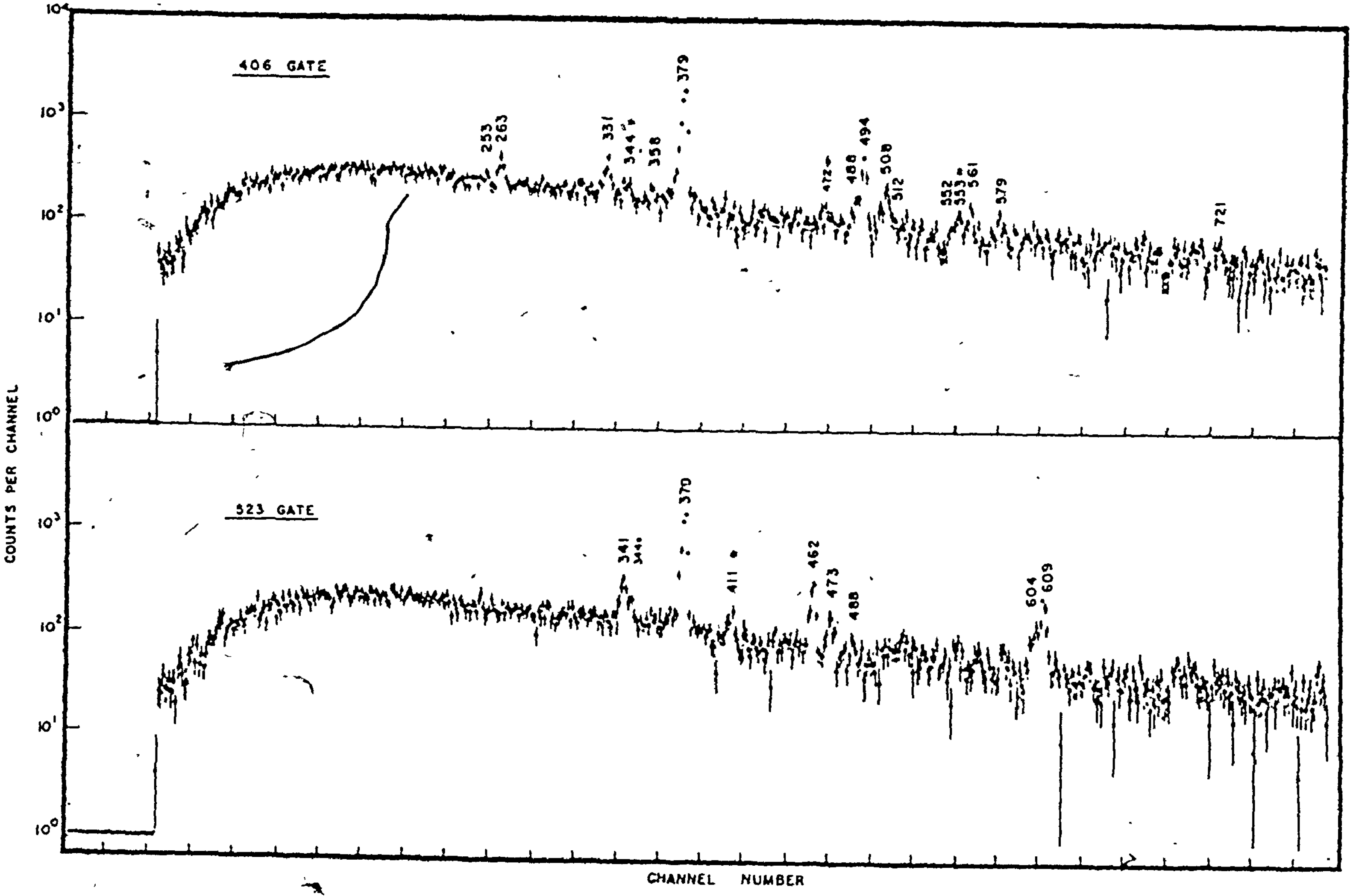

Figure 5-9

Spectra in coincidence with the 405.5 and 522.8 keV transitions.

5.6 Transition Multipolarities Deduced from Coincidence Probablilities

For low energy transitions, where the internal conversion intensity is comparable to the photon intensity, the branching in the decay pattern and hence the coincidence probabilities is strongly dependent on the multipolarities of the transitions. This property has been used in ^{151}Gd to deduce the multipolarities of the group of strong transitions with energies 65, 67 and 79 keV.

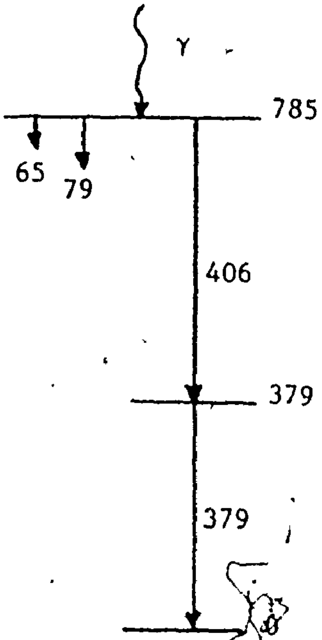

Consider the portion of the decay scheme shown in the accompanying sketch. It can readily be shown that

$$T_{65} + T_{79} = I_{\gamma i}\{\frac{I_{\gamma}}{C_{\gamma-\gamma i}} - 1\}$$

where T is the total transition strength (gamma plus conversion electron), I is the gamma ray intensity, γ is any transition feeding the 785 keV state and γ_i refers to either the 406 or 379 keV transition. Using this expression with the data of Tables 5-1 and 5-3 leads to the values of $T_{65} + T_{79}$ given in Table 5-4. Table 5-4 also lists the transition intensities expected from the measured photon intensities for various assumptions concerning the multipolarities of the 65 and 79 keV transitions. It is shown from these that agreement between $(T_{65} + T_{79})_{exp}$ and $(T_{65} + T_{79})$ predicted can only occur if <u>both</u> transitions are E1 in character.

In a similar way one can show that the 67 keV transition is M1.

It can be seen from the simplified level scheme to the right that

Table 5-4

a) The 65 and 79 keV transitions

EXPERIMENTAL $(T_{65}+T_{79})$
TRANSITION INTENSITIES

Cascade	$(T_{65}+T_{79})$ exp.
579-405	17±6
579-379	15±6
331-405	<18
331-379	<18

EXPECTED T_{65} and T_{79} TRANSITION
INTENSITIES FOR VARIOUS MULTIPOLARITIES

	E1	M1	E2
65	8	34	59
79	13	45	62

CONCLUSION: Both the 65 and 79 keV Transitions are E1

Table 5-4

b) 67 keV Transition

EXPERIMENTAL T_{67} INTENSITY FOR VARIOUS 146 keV MULTIPOLARITIES

Origin	146 (E1)	146(M1+E2)
494-146	53±10	45±10
263-146	36±10	27±10
494-379	38±10*	54±10*
494-405	34±10*	51±10*

EXPECTED T_{67} INTENSITY FOR VARIOUS 67 keV MULTIPOLARITIES

E1	M1	E2
10	43	72

*Assuming that 65 and 79 keV transitions are E1

CONCLUSION: The 67 keV Transition is predominantly M1

$$T_{67} = I_{146}(1+\alpha_{T146})\left(\frac{I_{\gamma}I_{\gamma i}}{(I_{406} + T_{65} + T_{79})C_{\gamma-\gamma i}} - 1\right)^{-1}$$

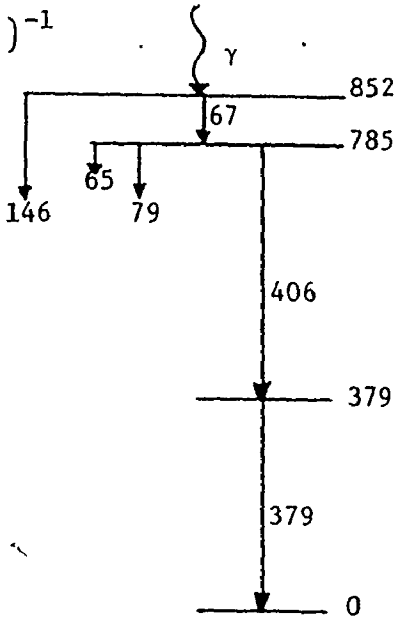

Table 5-4 tabulates values of T_{67} derived from this expression for four combinations of γ and γ_i and for values of α_{T146} appropriate to pure E1 or pure M1 multipolarities for the 146 keV transition. It is clear that the values of T_{67} are quite insensitive to the value of α_{T146} used.

The same table also presents the T_{67} intensity expected from the level structure if the 65 and 79 keV transitions are $\ell = 1$ for various multipole assignments to the 67 keV transition. Agreement is only possible if the 67 keV transition is predominantly M1.

The errors associated with the gamma ray intensities and coincidence probabilities are such that one cannot deduce meaningful values of mixing ratios from this type of analysis. However, the arguments presented above do clearly define the relative parities of a number of very important states in ^{151}Gd.

5.7 Gamma Ray Angular Distributions

Some 40 seven-point angular distributions were determined for transitions in ^{151}Gd and fitted to the function

$$W(\theta) = A_0\,[1 + A_2P_2 + A_4P_4]$$

The fourth and fifth columns of Table 5-1 present the A_2 and A_4 values derived from these 3-parameter fits. In addition, for those transitions which were masked by Pb lines in the target backing, the four point distributions were similarly analyzed.

For each gamma ray, the experimental data has been tested against a number of possible models, each of the form $J_i \xrightarrow[L,L+1]{} J_f$, as a function of the mixing parameter

$$\delta = \langle J_f \,||\, L+1 \,||\, J_i \rangle \,/\, \langle J_f \,||\, L \,||\, J_i \rangle$$

and the population parameters of the initial state. The quality of the fit was determined by the value of the reduced χ^2 of the least squares fitting procedure. Working upward from the ground state of ^{151}Gd, it was usually possible to begin with a fairly reliable J^π assignment for the final state and to use the analysis to decide between various possible values for the spin of the initial state.

The alignment of the residual nuclei in the (α,2n) reaction persists to a large degree during the emission of cascading gamma rays. Although the exact population parameters of the initial states in these successive transitions are not known, the angular distributions resulting are relatively insensitive to moderate changes in these parameters. It is generally accepted that the population distribution among the m substates of a level of spin J can be adequately represented by a Gaussian $P_J(m) = C \exp(-m^2/2\sigma^2)$ (Yamazaki,1967) where σ may be expected to retain about the same value for all states excited in a given reaction. To test this assumption, the experimental angular distributions for a number of "pure" transitions in ^{151}Gd and ^{152}Gd were fitted to the model for a variety of values of σ. Because the attenuation created by the finite solid angle of the detector was very small (Q_2 = 0.99 and Q_4 = 0.97), this attenuation was incorporated into the parameter σ for the purposes of analysis.

Fig. 5-10 presents the results for the ground-state band of ^{152}Gd produced by the (α,n) reaction and for a number of selected "pure" multipole transitions in ^{151}Gd formed by the (α,2n) reaction. For both ^{151}Gd and ^{152}Gd, the data for states of spin > 2 are reasonably well fitted to a σ value of $\sim$ 2.0. It should be noted that, for the high lying levels of either nucleus, χ^2_{min} is quite insensitive to the value of σ chosen. Fig. 5-10 also shows the effect of changing δ from 0 to $\pm$ tan 2° and $\pm$tan 4° corresponding to mixing of 0.12% and 0.24% of the (L + 1) component in a pure E1 or E2 transition. The "trade-off" between σ and δ clearly makes it impossible to determine δ with high precision using this technique.

Columns 9 to 12 of Table 5-1 tabulate the parameters of the model with σ= 2.0 providing the best fit to the experimental angular distributions which is consistent with the internal conversion data. The sign of δ reported in column 12 is opposite to that used in Yamazaki's (1967) compilation. Column 13 gives the percentage of quadrupole or octupole radiation corresponding to the value of the δ in column 12. In the light of the discussion above, the entries in column 13 have an uncertainty of $\sim$0.3 because σ is not known.

Fig. 5-11, 5-12 and 5-13 present the experimental distributions and the theoretical fits for twelve transitions of importance to the level scheme to be proposed. For each transition, the experimental

Figure 5-10

The reduced χ^2 for the least squares fit of the experimental angular distributions to the theoretical "model" , for a number of pure multipole transitions between states of known J^π plotted as a function of the Gaussian population parameter σ. For each curve, the value of the mixing ratio δ is specified through the angle $\tan^{-1}\delta$. The minimum χ^2 is clearly a function of both σ and δ.

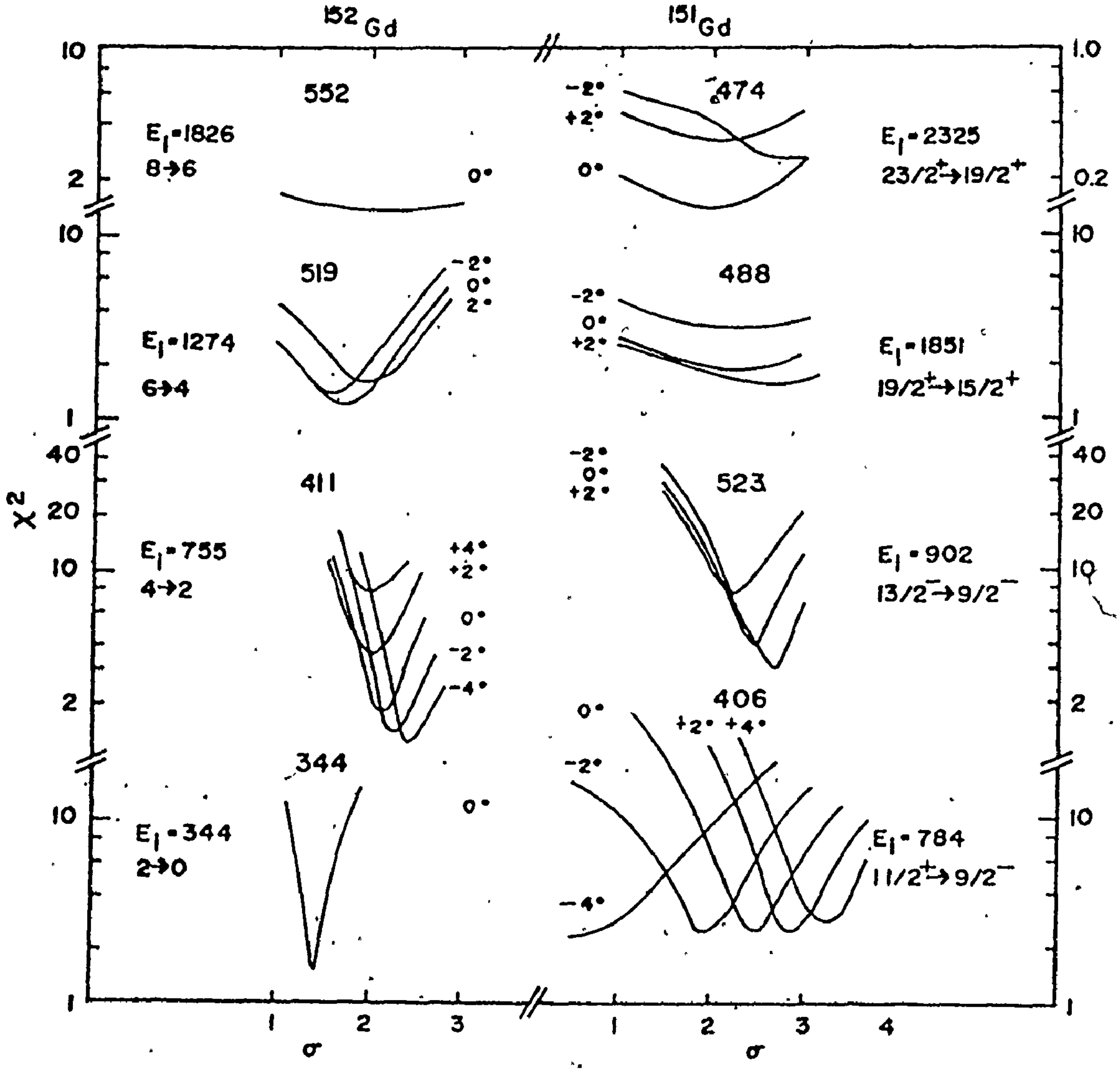
152 Gd
151 Gd
552
E1=1826
8→6
0°
474
−2°
+2°
0°
E1=2325
23/2+→19/2+
519
E1=1274
6→4
−2°
0°
2°
488
−2°
0°
+2°
E1=1851
19/2+→15/2+
411
E1=755
4→2
+4°
+2°
0°
−2°
−4°
523
−2°
0°
+2°
E1=902
13/2−→9/2−
344
E1=344
2→0
0°
406
0°
+2°
+4°
−2°
−4°
E1=784
11/2+→9/2−
χ2
10
2
10
1
40
20
10
2
10
1
1.0
0.2
10
1
40
20
10
2
10
1
1
2
3
σ
1
2
3
4
σ

Figures 5-11 , 5-12, 5-13

A comparison of the experimental angular distributions with those expected for various assumptions concerning J_i and J_f . For each transition shown , the left hand panel presents the experimental points and the theoretical curve corresponding to minimum χ^2 for the J_i , J_f choice shown. The right hand panel presents χ^2 vs $\tan^{-1}\delta$ for one or more J_i , J_f choices. The figures also show the range of $\tan^{-1}\delta$ consistent with internal conversion data. The value of χ^2 labelled LSF corresponds to the minimum χ^2 for the least squares fit of the data to a polynomial of the form:

$$W(\Theta) = \sum_{K=0}^{2} A_{2K} P_{2K} .$$

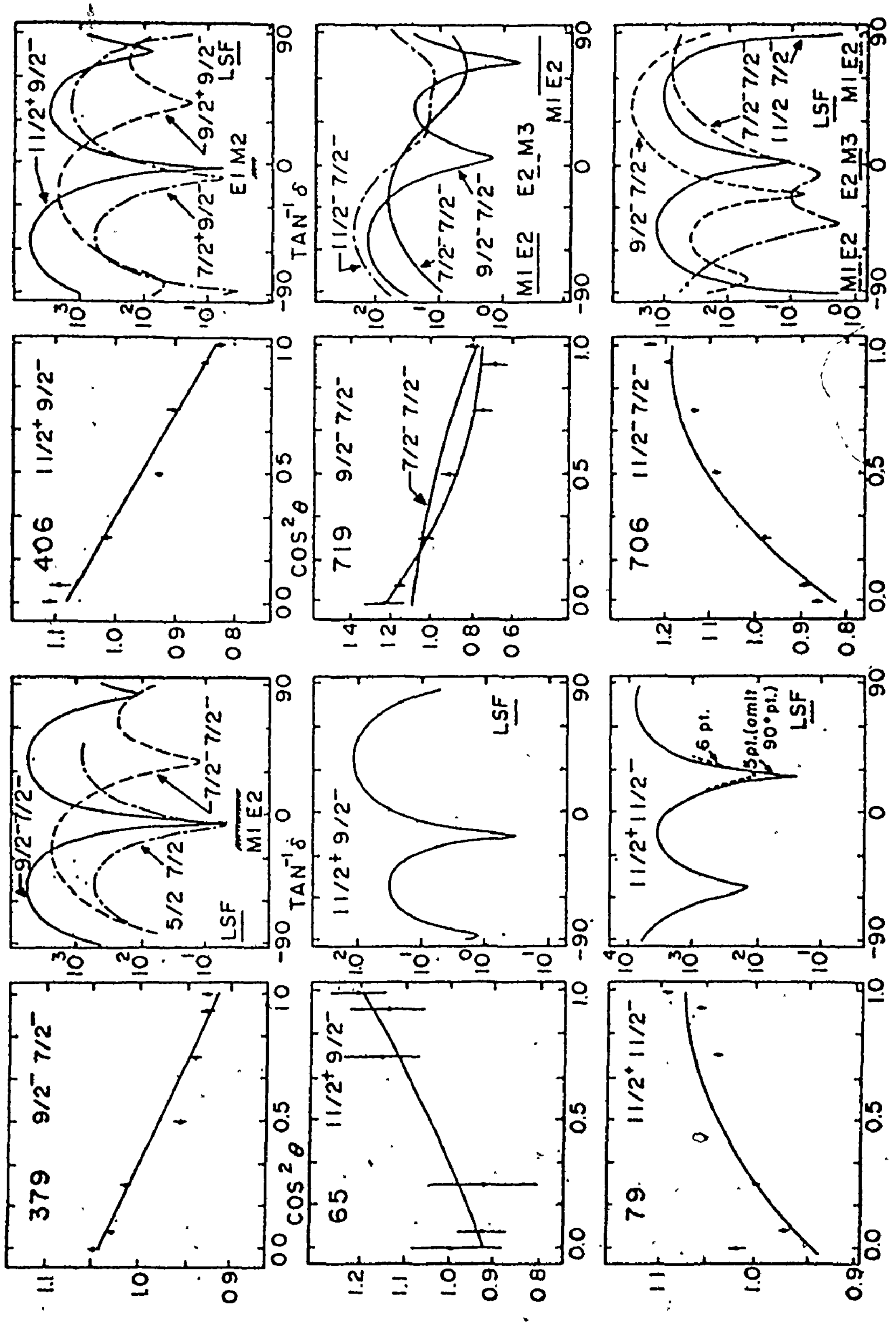
379
9/2⁻ 7/2⁻
65
11/2⁺ 9/2⁻
79
11/2⁺ 11/2⁻
406
11/2⁺ 9/2⁻
719
9/2⁻ 7/2⁻
7/2⁻ 7/2⁻
706
11/2⁻ 7/2⁻
COS²θ
TAN⁻¹δ
9/2⁻ 7/2⁻
5/2 7/2
7/2⁻ 7/2⁻
LSF
M1 E2
6 pt.
5 pt.(omit 90° pt.)
11/2⁺ 9/2⁻
7/2⁺ 9/2⁻
9/2⁺ 9/2⁻
E1 M2
11/2⁻ 7/2⁻
9/2⁻ 7/2⁻
E2 M3
11/2 7/2
0.0
0.5
1.0
-90
0
90

Figure 5-11

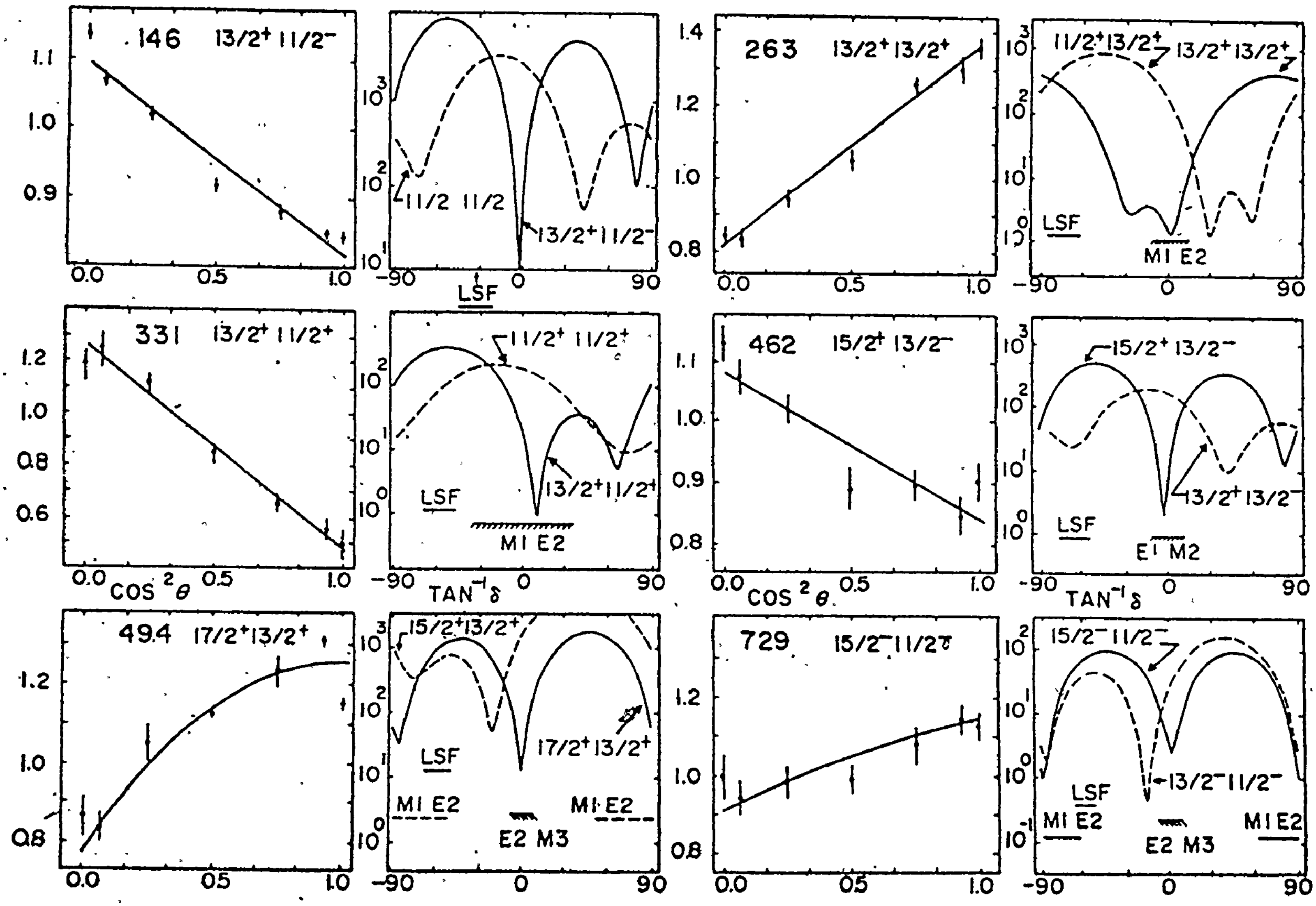
146 13/2+ 11/2−
1.1
1.0
0.9
0.0
0.5
1.0
10^3
10^2
10^1
11/2 11/2
13/2+ 11/2−
-90
0
90
LSF
263 13/2+ 13/2+
1.4
1.2
1.0
0.8
11/2+ 13/2+
13/2+ 13/2+
LSF
M1 E2
331 13/2+ 11/2+
0.6
0.8
COS $^2\theta$
11/2+ 11/2+
13/2+ 11/2+
10^0
M1 E2
TAN$^{-1}\delta$
462 15/2+ 13/2−
15/2+ 13/2−
13/2+ 13/2−
E1 M2
49.4 17/2+ 13/2+
15/2+ 13/2+
17/2+ 13/2+
M1 E2
E2 M3
729 15/2− 11/2−
15/2− 11/2−
13/2− 11/2−
10^{-1}

Figure 5-12

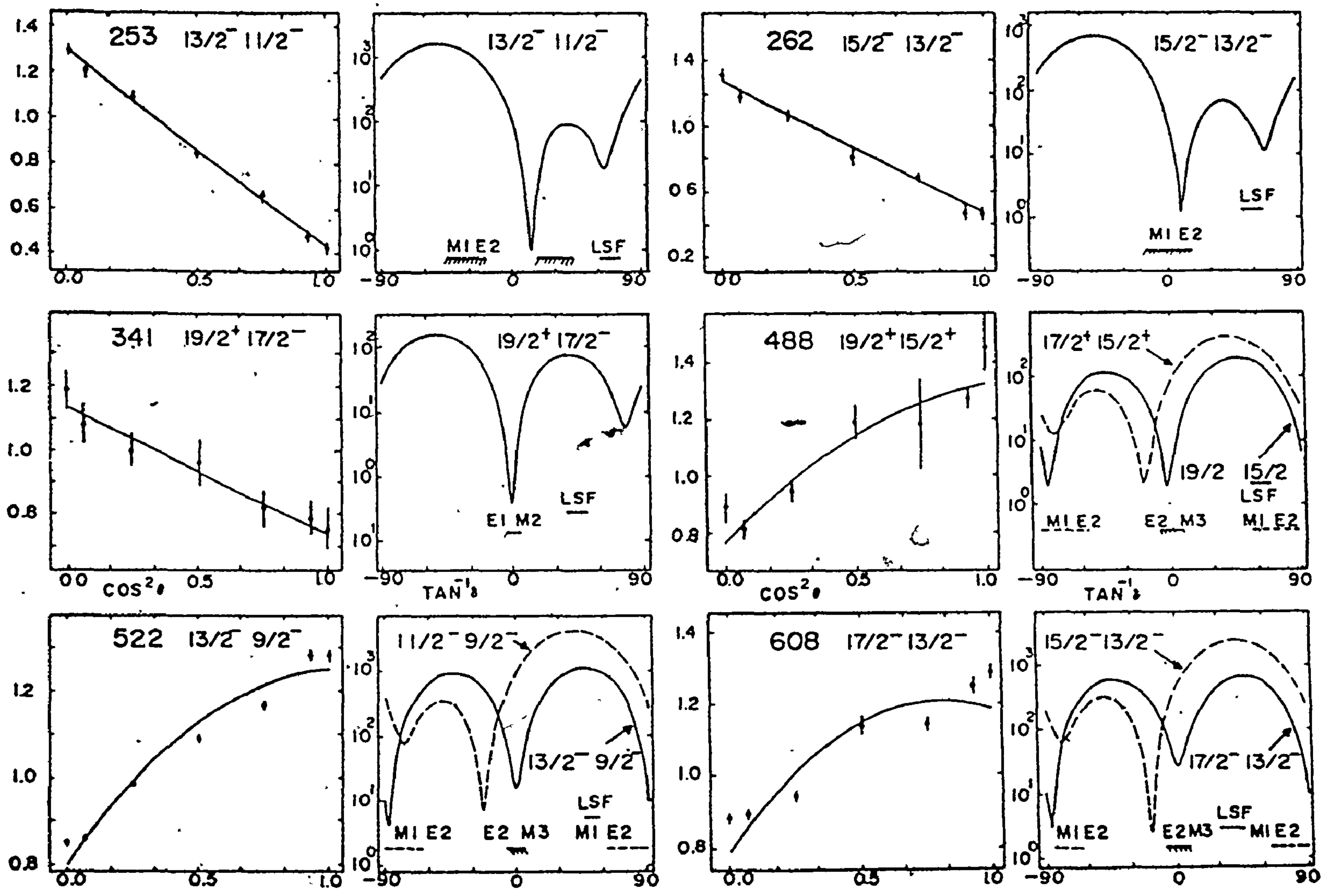
253 13/2⁻ 11/2⁻
13/2⁻ 11/2⁻
M1 E2
LSF
262 15/2⁻ 13/2⁻
15/2⁻ 13/2⁻
M1 E2
LSF
341 19/2⁺ 17/2⁻
19/2⁺ 17/2⁻
E1 M2
LSF
488 19/2⁺ 15/2⁺
17/2⁺ 15/2⁺
19/2
15/2
LSF
M1 E2
E2 M3
M1 E2
522 13/2⁻ 9/2⁻
11/2⁻ 9/2⁻
13/2⁻ 9/2⁻
LSF
M1 E2
E2 M3
M1 E2
608 17/2⁻ 13/2⁻
15/2⁻ 13/2⁻
17/2⁻ 13/2⁻
LSF
M1 E2
E2 M3
M1 E2
COS²θ
TAN⁻¹δ
0.0
0.5
1.0
-90
0
90
0.2
0.4
0.6
0.8
1.0
1.2
1.4
10⁰
10¹
10²
10³

Figure 5-13

points are shown in the left hand panel while the corresponding right hand panel presents a plot of χ^2 vs $\tan^{-1}\delta$ for the labelled spin sequence. In general, χ^2 has a minimum value for two values of δ. Often, one of these can be rejected on physical grounds, or because it is inconsistent with the limits set on $|\delta|$ by the internal conversion data. These limits are indicated by horizontal lines in the right hand panels. In some cases, the χ^2 vs $\tan^{-1}\delta$ curves are shown for several spin sequences. In these, the solid curves represent the preferred choice. The solid curve drawn through the experimental points for each transition is the theoretical distribution corresponding to minimum χ^2. A comparison of the model coefficients of Table 5-1 with the experimental ones shows that the two are in most cases indistinguishable. The values of $(\chi^2)_{min}$ associated with the experimental coefficients for the cases presented in Fig. 5-11, 5-12 and 5-13 are indicated by the lines labelled LSF. In most cases, these are very close to the minimal values of χ^2 in the χ^2 vs $\tan^{-1}\delta$ plots.

The final column of Table 5-1 presents the J^π values of the initial state for each transition, using all the information available.

5.8 Internal Conversion Coefficients

The electron spectrum was scanned from about 175 to 730 keV, using the seven-gap beta ray spectrometer described in Chapter 4, at a beam energy of 24 MeV. The momentum resolution of ~0.9 % achieved in these experiments represents a folding of the 0.5% instrumental resolution and the broadening imposed by target thickness at this resolution. Many of the conversion lines were unresolved. Fig. 5-14 presents the data accumulated over the course of 3 experimental runs. The differences in line shape associated with different experiments reflect the problems discussed in Chapter 4. Fig. 5-15 illustrates the nature of the analysis necessary to decompose an unresolved group of peaks.

Relative Internal Conversion coefficients were derived from these intensities by correcting them for electron detection efficiencies (see Chapter 4) and dividing by the intensities of the corresponding gamma rays (emitted at 55° where the $P_2(\cos\theta)$ term vanishes). These coefficients were normalized to absolute conversion coefficents by using the strong E2 transition at 344 keV in ^{152}Gd (for the low energy portion of the spectrum) and the pure E2 transitions at 508 and 706 keV transition in ^{151}Gd for the high energy portion.

The results of these analysis are presented in Tables 5-5 and 5-6 and in Fig. 5-16. The first two columns of these tables present gamma ray energies and intensities. These intensities which were derived from a singles run taken at 55° differ slightly from those of Table 5-1 which represent the mean of values determined in several runs with several different detectors. The third column gives normalized and

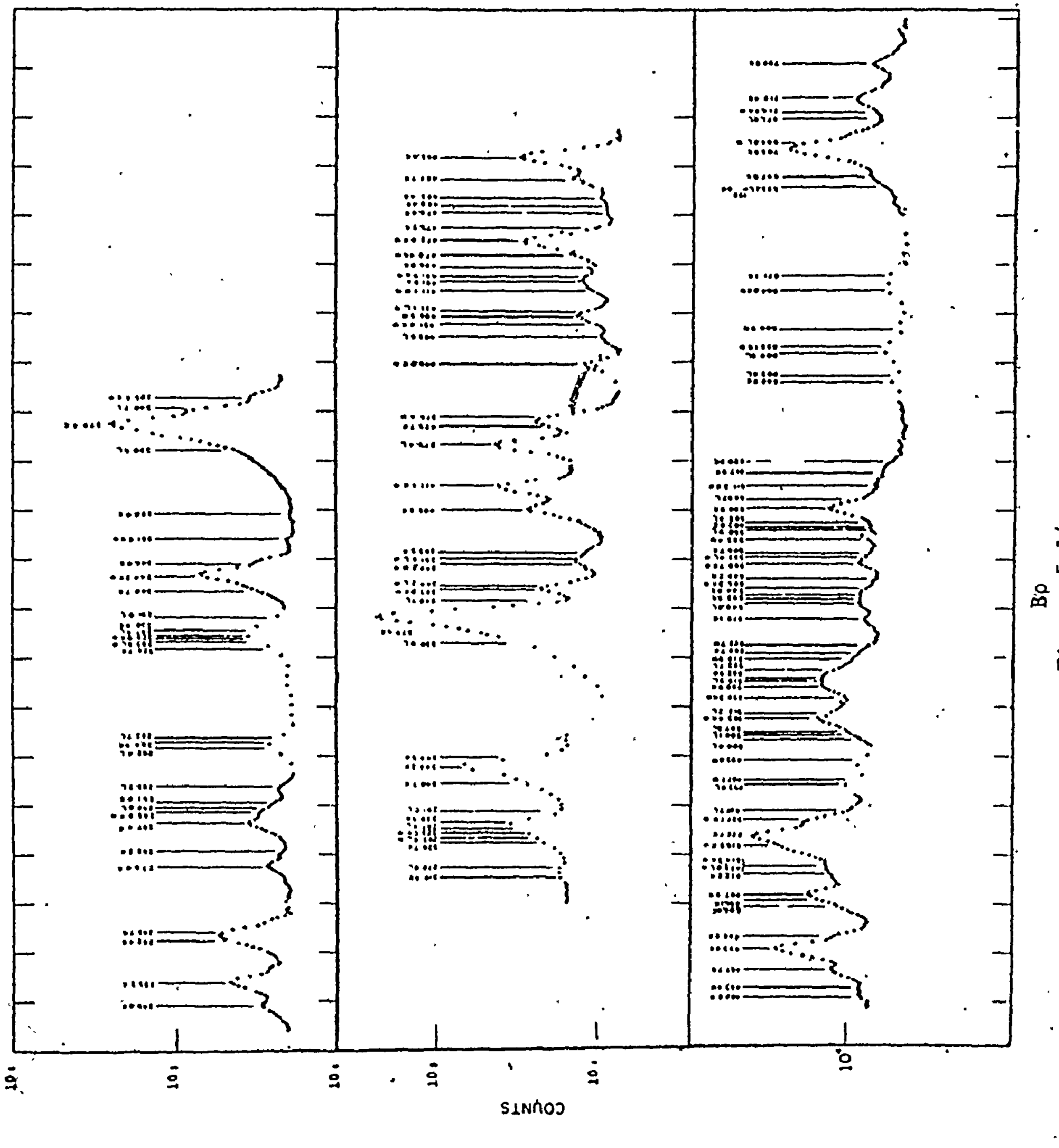

Figure 5-14

Conversion electron spectrum from the ^{149}Sm(α,xn) reactions from ~175 to ~730 keV using the "Orange" β-ray spectrometer.

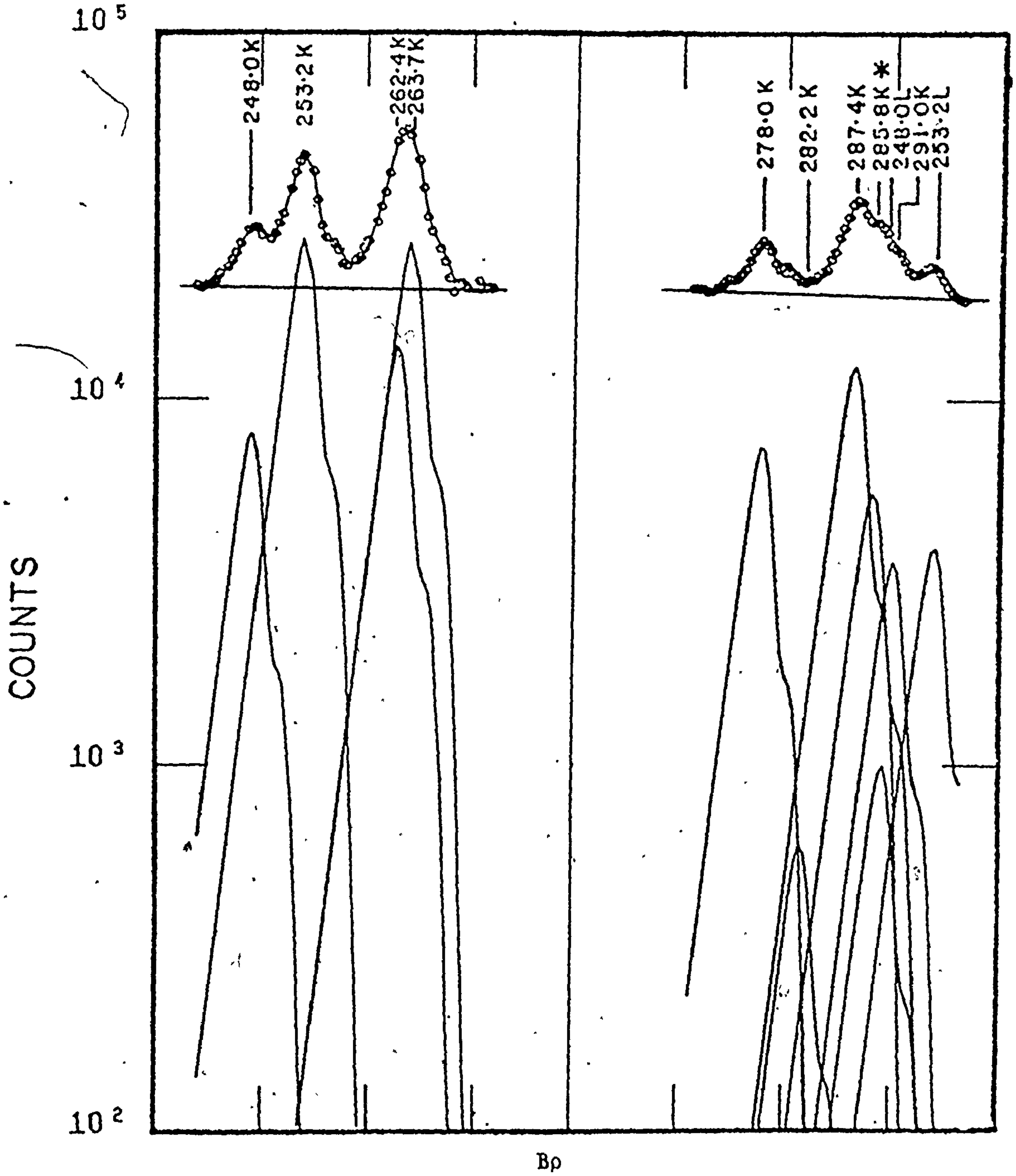

Figure 5-15

Examples of analyzed conversion electron multiplets.

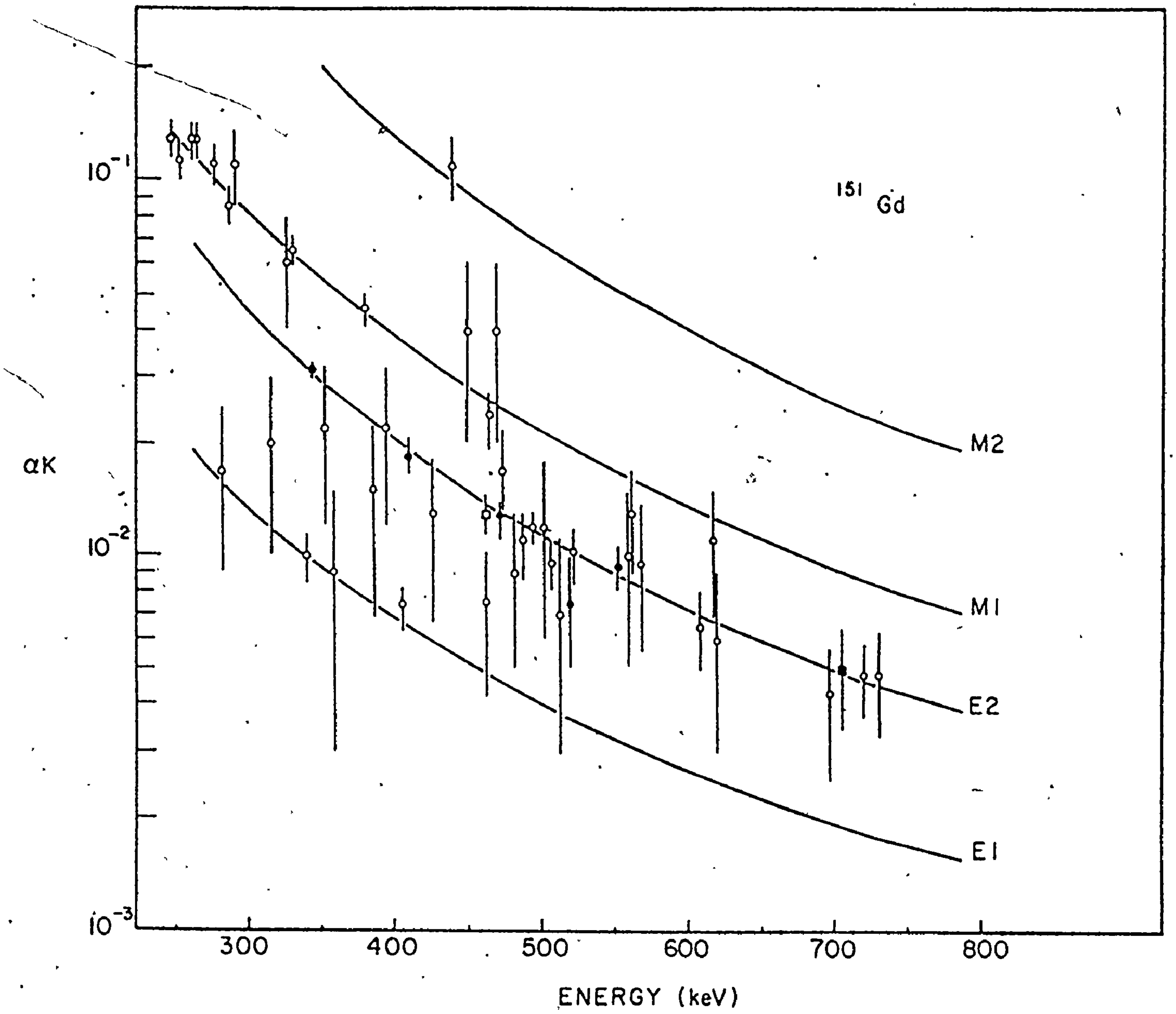

Figure 5-16

Conversion coefficients of gamma rays in the spectrum resulting from the ^{149}Sm(α,xn) reactions determined from the conversion electron spectrum.

efficiency corrected electron intensities and the fourth, the values of α_K deduced from columns 2 and 3. The experimental errors on α_K range from ∿10% for well defined and clearly resolved peaks to ±100% for very weak transitions. Confirmation of the correctness of the normalization procedure is provided by other conversion coefficents for the members of the ground state band in ^{152}Gd which are shown as solid points in Fig. 5-16 and which cluster closely about the theoretical curve for E2 transitions (Hager & Seltzer, (1968)). The one exception is the 519 keV transition whose electron peak was only partially resolved from the much stronger 523 keV transition. The remainder of Table 5-5 presents the theoretical α_K conversion coefficents for E1, M1 and E2 and the conclusions drawn with respect to the multipolarities of the observed transition. The last column identifies the position of the transition in the level structure.

Table 5-5 presents the results for transitions in ^{151}Gd. Table 5-6 presents the results for contaminant lines in the spectrum.

For weak internal conversion peaks, the determination of the background is crucial and is the most important source of uncertainty in α_K. For the K lines of transitions between 570 and 590 keV, it was impossible to obtain meaningful conversion coefficents. In many parts of the spectrum, the K peak of concern is masked by unresolved L and M peaks of stronger transitions. In cases where their multipolarities had been determined from the K-conversion coefficents, their L conversion intensity was calculated and the residue attributed to the K peak in question. Comments on individual cases appear

Table 5.5

Conversion Electron Intensities and Transition Multipolarities in ^{151}Gd

E_γ (keV)	I_γ	I_e x10^2	α_K x10^2	Comment	Theoretical α_K x10^2 E1	E2	M1	Assigned Multipolarity††	Initial State
248.0	1.5±0.1	19±2	13±1.5		2.15	8.4	13.6	M1	1364
253.2	6.5±0.2	74±7	11.3±1.2		2.05	7.8	13.0	M1	1463
262.4	3.5±0.2	45±5	12.8±1.3	a)	1.90	6.9	11.9	M1	1726
263.7	5.1±0.2	64±8	12.5±1.3	a)	1.88	6.8	11.8	M1	1116
278.0	2.0±0.2	22±3	11±1.5		1.62	5.7	10.0	M1	2004
287.3	3.9±0.2	33±3	8.6±0.9		1.50	5.2	9.0	M1	395
291.4	1.3±0.1	15±3	11±2	b)	1.46	5.0	8.8	M1	2295
296.7	0.6±0.2	(9.6-12)		c)					
318.8	1.1±0.2	1.8±1	1.6±1.4	d)	1.17	3.8	6.8	E1 or E2	427
326.7	1.0±0.2	5.2±2	5±2	e)	1.10	3.6	6.4	M1 + E2	706
330.9	4.8±0.2	34±6	7.0±1.5	f)	1.06	3.5	6.1	M1	1116

a) The 262 and 263 keV peaks are imperfectly resolved in the electron spectrum. The conversion electron data indicates that they are both M1.

b) The 291 K and 248 L lines are superposed. The total electron intensity of 17.6 has been corrected for the L contributions of the 248 keV M1 transition.

c) The 296 K and 253 L lines are superposed. The calculated electron intensity from the 253 L line is 12±3 so that no estimate of α_K for the 296 keV transition is possible.

d) The 318 K and 277 L are superposed. The calculated contribution from the L peak of 3.6 has been subtracted to give the K line intensity shown.

e) The 326 K, 285 L from Coulomb excitation, and 329 K (see table 5-6) are unresolved. Analysis of this complex peak is very unreliable. The calculated contribution from the L line of 2.6 has been subtracted.

f) The observed peak has been corrected for a calculated 5.0 contribution from the 287 L.

†† Predominant component.

Table 5-5 (continued)

E_γ (keV)	I_γ	I_{e_2} x10^2	α_{K_2} x10^2	Comment	Theorectical α_K x10^2 E1	E2	M1	Assigned†† Multipolarity	Initial State
340.6	6.1±0.1	6.1±1.5	1.0±0.2	g)	1.00	3.2	5.7	E1	1852
358.0	1.3±0.1	<1	<0.9		0.9	2.8	5.1	E1	1210
379.4	100	440±40	4.4±0.4		0.76	2.3	4.3	M1	379
395.5	1.4±0.2	3±1.5	2±1	h)	0.69	2.1	3.9	E2	395
405.5	36±1	27±3	0.74±0.09		0.65	1.95	3.6	E1	785
426.7	6.9±0.7	9±6	1.3±1.0	i)	0.57	1.70	3.2	E2	427
461.9	6±1	4±1.5	0.6±0.2	j)	0.48	1.36	2.6	E1	1364
466.0	1.3±0.1	4±2	3±2	k)	0.46	1.32	2.55	M1,E2	
473.5	4.5±0.4	8±3	1.8±0.8	l)	0.45	1.29	2.50	M1,E2	2325
479.6	1.0±0.1	2.4±1.2	1.4±0.7	m)	0.44	1.22	2.40	M1,E2	587
480.4	0.7±0.1							M1,E2	589

g) Difficult to resolve from strong 344 peak. A second determination with poorer statistics gave $\alpha_K = 1.6 \pm 0.6$.

h) Corrected for a calculated 344 M contribution of 7.6.

i) Corrected for calculated 379 M and 385 L contributions of 14.5 and 1.3 respectively.

j) 462 keV transitions appear in both ^{149}Sm and ^{151}Gd. In ^{149}Sm it is in coincidence with the 198 keV transition (Thompson, private communication) which appears free of contaminants in our spectra. In Thompson's work $I_{462}/I_{198} = 2.68$ and in our work $I_{198} = 1.17$. Therefore the gamma ray intensity of the ^{149}Sm E2 component is 3.2 and the electron intensity is calculated to be ∿4. I_γ and I_e have both been corrected for the ^{149}Sm component.

k) A weak peak between 462 K and 472 K of table 5-6.

l) The 470 K peak of table 5-6 and the 473 K conversion peak are shoulders on the strong 472 K and as such are subject to large uncertainties.

m) These peaks were analysed in 2 different runs. The errors are very large and conclusions drawn as to multipolarities cannot be taken very seriously.

Table 5-5 (continued)

E_γ (keV)	I_γ	I_{e_2} x10^2	α_K x10^2	Comments	Theoretical α_K x10^2			Assigned†† Multipolarity	Initial State
					E1	E2	M1		
483.4	1.2±0.1	1.8±0.8	1.5±0.7	m)	0.43	1.21	2.35	M1,E2	
487.7	5.9±0.5	8±2	1.3±0.4	n)	0.42	1.20	2.32	E2	1852
493.6	27±2	38±6	1.4±0.2		0.41	1.18	2.25	E2	1346
496.2	1.5±0.3			o)					
504.4	1.4±0.1	1.7±1.0	1.2±0.7	p)	0.40	1.10	2.15	M1,E2	1210
507.5	13.5±0.2	14±2	1.0±0.2	q)	0.39	1.08	2.10	E2	1853
512.2	4.5±1.0	3.4±1.0	0.8±0.3	r)	0.39	1.05	2.05	E2	1364
522.7	40.7±2	45±5	1.10±0.15		0.37	1.00	1.95	E2	902
560.9	3.5±0.1	2.7±1.5	0.8±0.3	s)	0.32	0.85	1.63	E2	1677
562.9	4.3±0.1	5.4±2	1.3±0.4	s)	0.32	0.85	1.63	M1	671

m) These peaks were analysed in 2 different runs. The errors are very large and conclusions drawn as to multipolarities cannot be taken very seriously.

n) Mean of 2 determinations.

o) Masked by 493.6 K line.

p) Almost masked by 507 K.

q) This transition is a doublet (see table 5-1). The combined electron and combined photon intensities have been used in obtaining α_K. The dominant component is E2 and the weaker M1, from the level scheme.

r) 512.2 K is incompletely resolved from 472 and 473 L which completely mask the region of the 514 and 515 K.

s) The 519 L of calculated intensity 2.7 falls between the 561 and 563 K. The total remaining intensity of 8.1 is distributed rather arbitrarily between the 560 K and 563 K.

Table 5-5 (continued)

E_γ (keV)	I_γ	I_{e} x10^2	α_K x10^2	Comment	Theoretical α_K x10^2			Assigned†† Multipolarity	Initial State
					E1	E2	M1		
568.7	1.8±0.5	3.4±2	2±1	t)	0.31	0.84	1.62	M1,E2	2295
579.1	3.5			u)					
583.5	2.5			u)					
584.8	4.9			u)					
586.3	2.7			u)					
589.2	1.8			u)					
608.9	15.6±1.5	10±2	0.7±0.2		0.27	0.73	1.73	E2	1511
617.8	1.3±0.2	1.6±0.4	1.2±0.3		0.25	0.68	1.30	M1,E2	618
620.5	1.8±0.2	1.1±0.3	0.7±0.3		0.25	0.68	1.30	E2	2915
697.6	5.3±0.5	2.4±0.8	0.5±0.2		0.20	0.51	0.94	E2	1077
705.9	46±2	24±5	0.52±0.10		0.19	0.50	0.91	E2	706
719.4	12.0	6.2±1.5	0.52±0.11	v)	0.19	0.48	0.88	M1,E2	1506 1425
729.0	6.8	3.6±0.7	0.52±0.11		0.18	0.46	0.85	E2	1435

t) This line is unresolved from the 519 M, 527 L and 523 M with a total calculated intensity of 2.4. The residue of the peak has been attributed to 569 K.

u) The analysis of the many weak peaks in this region is so sensitive to the choice of background as to make the results meaningless.

v) This is an unresolved triplet (see table 5-1) and so the derived multipolarity is uncertain.

Table 5-6

Conversion Electron Intensities and Transition Multipolarities for Contaminant Transitions

E_γ (keV)	I_γ	I_e $\times10^2$	α_K $\times10^2$	Comment	Theoretical α_K $\times10^2$ E1	E2	M1	Assigned Multipolarity	Origin
282.2	0.4±0.1	0.7±0.3	1.7±0.8		1.56	5.3	9.5	E1	
329.0	0.9±0.2	3.8±2	4±2	a)	1.08	3.5	6.4	M1 + E2	
344.2	34.8±0.9	103±10	3.1±0.3	b)	0.96	3.15	5.70	E2	^{152}Gd
351.6	1.9±0.1	4±2	2±1		0.95	3.0	5.3	E1 or E2	
385.8	2.8±0.3	5±2	2±1	c)					
411.1	31.5±0.6	55±3	1.86±0.1		0.53	1.82	3.55	E2	^{152}Gd
440.0	0.8±0.09	9±3	11±4		0.50	1.59	3.1		
451.4	0.9±0.1	4.5±2	5±2	d)	0.5	1.4	2.8		
461.9	3.2	∿4	1.3±0.5	e)	0.48	1.36	2.6	E2	^{149}Sm
470.4	2.4±0.2	10±4	4±2	f)	0.46	1.30	2.52		
472.0	23±2	29±4	1.3±0.2		0.46	1.30	2.48	E2	^{152}Gd
519.5	15.1±1.5	11±1	0.8±0.2		0.38	1.03	1.95	E2	^{152}Gd
527.1	1.6±0.1	6±2	3.5±1.3		0.36	0.98	1.88		^{152}Gd
553.4	13.4±1.0	10±2	0.8±0.2	g)	0.33	0.90	1.70	E2	^{152}Gd
714.8	2.3	1.4±0.5	0.6±0.2		0.18	0.48	0.88		

a) See comment e) Table 5-5.

b) Member of g.s.b. ^{152}Gd therefore pure E2, used for normalization.

c) Corrected for a calculated 344 L contribution of 23.

d) Incompletely resolved from and located between the 405 L and 411 L peaks of intensities 4 and 10 respectively. The α_L values for these two peaks are consistent with their E1 and E2 assignments as given in Table 5-5.

e) See comment j) of Table 5-5.

f) See comment l) of Table 5-5.

g) Corrected for 507 and 512 L of total intensity ∿3.6.

as footnotes to Tables 5-5 and 5-6.

Although the conversion coefficents resulting from these measurements are not of high quality, as measured by the standards of beta ray spectroscopy with radioactive sources, they are comparable in quality with those obtainable in on-line accelerator experiments. Despite the fact that the instrumental resolution was inadequate to obtain first class internal conversion data, it has been generally possible to distinguish E1 from E2 or M1 + E2 mixtures and thus to give essential information concerning the parities of states. The data is inadequate for determining M1/E2 mixing ratios.

A number of transitions (341, 406, 462) are seen to be E1 in character. Of these, the 406 keV transition is crucial to the later discussion and interpretation of the structure. Fig. 5-17 presents a comparison of the electron and gamma ray spectrum for this transition.

The experimental data is shown as solid dots and the spectrum corrected for the background (the nearly horizontal solid line) is shown by a series of x's. The analysis of this spectrum was carried out graphically to give the peaks shown. The line shape for all peaks in the analysis was obtained from the strong 379-K conversion line.

Since the 411 keV transition in ^{152}Gd is pure E2, it can be used for internal normalization. Using this normalization, the 406 K peaks expected for various choices of multipolarity (E1, E2, M1) were calculated and shown as dashed curves in the Figure. It is clear that the 406 keV transition must be E1 and that therefore the states connected by this transition have opposite parity.

Figure 5-17

A comparison of the electron and gamma ray spectra in the 400 keV region. The upper spectrum was recorded with a Ge(Li) detector; the lower with the "Orange" β-ray spectrometer. The electron data have been resolved into an almost constant background and electron peaks with the same line shape as the strong K conversion line of the 379 keV transition. The 7 gap "Orange" spectrometer removes most of the anisotropy in the emission of conversion electrons. It is estimated that the maximum correction to any conversion electron intensity in the geometry of this experiment is 20°/₀. Such effects are far too small to void the conclusion that the 406 keV transition is E1 in character.

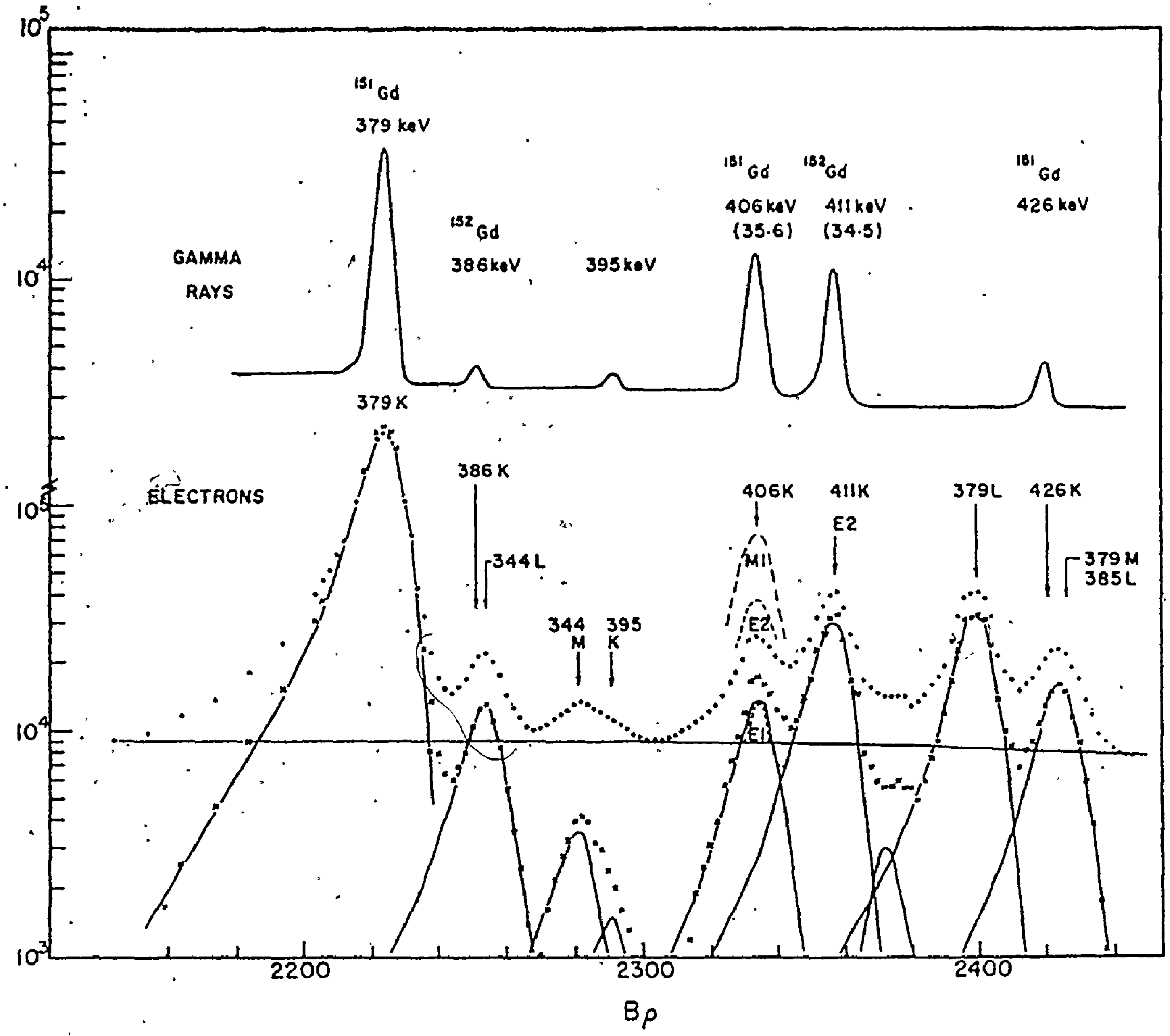

10^5
10^4
10^5
10^4
10^3
GAMMA RAYS
^{151}Gd 379 keV
^{152}Gd 386 keV
395 keV
^{151}Gd 406 keV (35.6)
^{152}Gd 411 keV (34.5)
^{151}Gd 426 keV
ELECTRONS
379 K
386 K
344 L
344 M
395 K
406 K
M1
E2
E1
411K
E2
379L
426K
379 M
385 L
2200
2300
2400
Bρ

Figure 5-17

5.9 The Particle Transfer Measurements

The author was peripherally involved with single nucleon transfer experiments being carried out simultaneously at McMaster but had no substantial part in the interpretation. These experiments are mentioned here as additional support for the level assignments discussed in section 5.10.

Only a small fraction of the states populated in the present (α,2n) study are seen in the (^{3}He,α) and (d,t) transfer studies. Table 5-7 presents the energies of the states common to the present work and the work of Løvhøiden and Burke (1975). The table also contains the differential cross-sections for the (d,t) reaction at 90° and the (^{3}He,α) reaction at 30°, taken from this paper. The ratio of the (^{3}He,α) to (d,t) cross-sections is a sensitive function of ℓ value and has been used to obtain the values of Table 5-7. The J^{π} assignments are those of Løvhøiden and Burke (1975).

5.10 Spin and Parity Assignments

The level structure of Fig. 5-18 satisfies the data presented and the measured coincidence probabilities. Throughout this work, the position has been taken that coincidence evidence is required before a transition can be definitely assigned to ^{151}Gd. The few exceptions involve weakly populated, low spin states, some of which were observed in the electron capture studies of Gonsior et al (1971) and Hammaren et al (1975), or transitions which fit between well established levels.

Table 5-7

Cross-sections, ℓ-transfer values, and spin-parity assignments for states in ^{151}Gd populated in the (d,t) and (^{3}He,α) reactions. (Løvhøiden and Burke, 1975)

Energies			dσ/dΩ in μb/s.r.		ℓ-value	J^π
			(d,t)	(^{3}He,α)		
(α,2n)	(d,t)[a]	(^{3}He,α)	90°	30°		
0	0	0	358	30	3	$7/2^-$
108	109	111	6	~ 3	≤ 4	$5/2^-$
379	380	375	25	50	5	$9/2^-$
395	395	-	119	≤ 3	≤ 2	$3/2^-$
427	426	429	21	3	3	$(7/2^-)$[b]
587	587	-	66	<3	1	$3/2^-$
618	620	-	21	<3	≤ 3	$5/2^-$
671	671	667	54	8	3(2)	$7/2^-$
706	706	-	2	-	-	-
852	854	850	7	91	6	$13/2^+$
902	913	914	2	11	5,6	ℓ=5
1210	1209	1209	29	94	5	$11/2^-$

a) The energy calibration for the (α,2n) experiment gives different energies from those of the (d,t) and (^{3}He,α) experiments which suggests that the 902 keV state of the present work is not excited in the particle transfer work.

b) Present work favors a $5/2^-$ assignment.

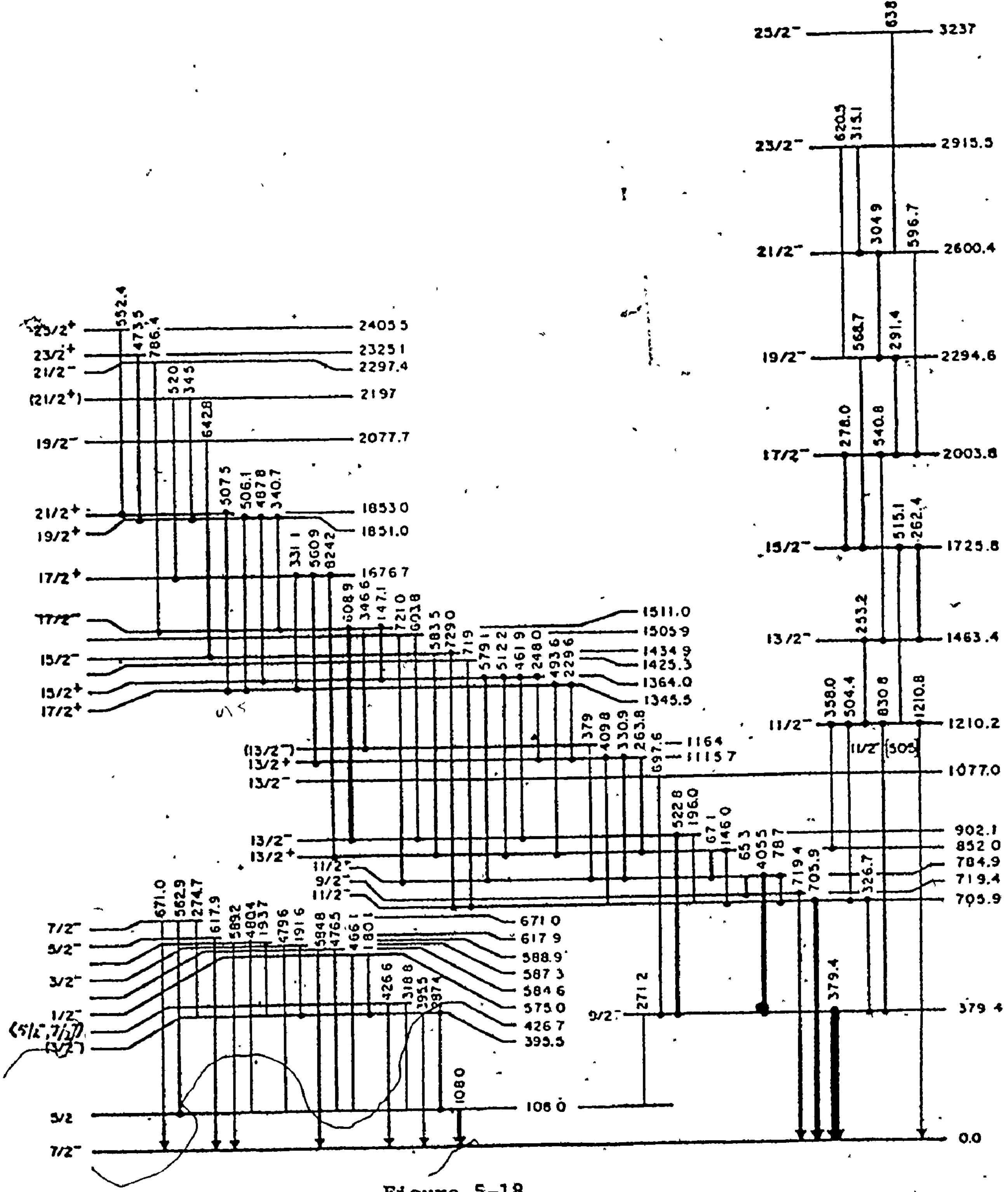

Figure 5-18

The level structure of ^{151}Gd as deduced from the present measurements. Assignments based on coincidence evidence are indicated by a dot on the end of the transition arrow.

Since the (α,2n) reaction transfers a large amount of angular momentum, the residual nucleus is formed in a high spin state from which it deexcites by gamma ray cascades. One can therefore, in general, expect that the spin of the initial state in any transition will be higher than that of the final state. This argument has been used in favouring the adoption of a higher spin in cases when the data cannot distinguish between transitions such as J → (J − 2) and J → (J + 2). Also, as a consequence of this mechanism, we see very few low spin states.

The spin of the ground state of ^{151}Gd has been measured by Ekstrom (1974) to be 7/2 and the systematics of nuclei and the shell model strongly suggest that this is a negative parity state created by an odd neutron in the $f_{7/2}$ shell.

Many of the levels in the lower left hand portion of Fig. 5-18 are weakly populated in (α,2n) and the spin assignments depend heavily on electron capture and particle transfer data. The present experiments offer additional support for the following assignments made by Gonsior et al (1971) and Hammaren et al (1975); 108($5/2^-$), 395($3/2^-$) and 575($1/2^-$) keV. We also identify the 587 keV state seen by both groups but prefer Hammaren's $3/2^-$ assignment which we base on the particle transfer work. The 427 keV state was identified by Hammaren et al and assigned $J^\pi = 5/2^-$ on the basis of $\gamma-\gamma$ coincidence data. This assignment is consistent with our angular distributions. However the particle reaction data is ambiguous and Afanasiev et al,(1975) have assigned it as 7/2−. As a result of the uncertainty J^π=(5/2−,7/2−). The remaining states of the group are not observed in electron capture and therefore presumably have $J^\pi \geq 5/2$.

The existence of the 671(7/2$^-$) keV state is solidly established by both the (α,2n) and particle work, the 617 (5/2$^-$) keV level is moderately well established, and the 585 and 589 keV states must be regarded as tentative. None of the other states populated in electron capture are observed in our (α,2n) measurements.

The 379.4 keV state is very strongly populated and deexcites by an M1 ground state transition. The angular distribution data Fig.5-11 restricts its spin to 5/2$^-$ or 9/2$^-$. The particle reaction work limits J^π to 9/2$^-$ or 11/2$^-$ so that it must be assigned J^π = 9/2$^-$. The 9/2$^-$ choice is also consistent with the angular distribution of the weak 271 keV transition from the 379.4 to the 108.0 keV (5/2$^-$) state.

The 705.9 and 852.0 keV states will be discussed together. The 706 keV state is strongly populated and decays to the ground state by an E2 transition. The angular distribution of Fig. 5-11 is characteristic of a stretched E2 and picks out 11/2$^-$ as the preferred choice for J^π. The 852 keV state is strongly populated by an ℓ = 6 transfer in the particle experiments so that its J^π is either 11/2$^+$ or 13/2$^+$. The two states are connected by a strong dipole transition of energy 146 keV whose angular distribution (Fig. 5-12) is quite inconsistent with the 11/2$^+$ choice. The very sharp minimum in the χ^2 vs δ plot for the 13/2$^+$ choice occurs for an E1 transition with a 0.09% M2 admixture. The 13/2$^+$ choice for the 852 keV state was made by Løvhøiden et al (1975) by invoking the fact that no shell model strength for an 11/2$^+$ is expected in this region of the mass table. The present data makes it unnecessary to invoke the model to reach this conclusion.

The 784.9 keV state deexcites via a strong E1 transition of 406 keV to the $9/2^-$ state at 379 keV and by weaker transitions of 65 and 79 keV to the 719 and 706 keV levels. Fig. 5-11 shows clearly that the spin of the 784.9 keV state must be either $11/2^+$ or $7/2^+$. The presence of the 67 keV transition from the 852.0 state eliminates the $7/2^+$ choice. The M1 character of the 67 keV (852.0 → 784.9) transition established by the γ-γ coincidence probabilities is consistent with the angular distribution data, although either a pure dipole or a pure quadrupole solution would give good fits to the $13/2^+ \rightarrow 11/2^+$ "model". The E1 character of the 79 keV (784.9 → 705.9) transition, is likewise confirmed by the angular distributions of Fig. 5-11. The rather large (18%) M2 component required to obtain a good $11/2^+ \rightarrow 11/2^-$ "model fit" to the experimental data can be attributed to errors in the experimental yields for this low energy transition.

The 719 keV state is also deexcited by an E2 transition but the angular distribution of Fig. 5-11 clearly indicates that it is not of the stretched E2 type. The data of Table 5-1 are consistent with $J^\pi = 7/2^-$ or $9/2^-$. The 65 (784.9 → 719.4) keV transition connecting this state to the $11/2^+$ state at 784.9 keV eliminates the $7/2^-$ choice.

The 902 keV state deexcites to the 379.4 keV ($9/2^-$) state by means of a stretched E2 transition of energy 523 keV. The data of Fig. 5-13 show clearly that the $13/2^-$ choice alone is acceptable. The $5/2^-$ choice, which would also fit the angular distributions is inconsistent with the large positive slope of the cross-section versus excitation energy function for this transition and with $\ell = 5$ or 6 from the particle transfer experiment.

The 1077 keV state is based on the existence of a strong 697-379 keV cascade. The four-point angular distribution and internal conversion data of Table 5-1 are consistent with the 697 keV transition being a stretched E2, thus defining J^{π} for the 1077 keV state as $13/2^{-}$. Unfortunately, the 697 keV transition was masked by an impurity line in the 7-point angular distribution experiment.

The 1115.7 keV state deexcites to the 784.9 ($11/2^{+}$) and 852.0 ($13/2^{+}$) states by the 331 and 263 keV M1 transitions as shown in Fig. 5-12 and Table 5-1. The data for these two transitions uniquely define J^{π} for the 1115.7 keV state as $13/2^{+}$.

The 1345.5 keV state deexcites by a strong 493.6 keV transition to the 852.0 ($13/2^{+}$) level and a much weaker 229.6 keV line. Fig. 5-12 and Table 5-1 show clearly that the 493.6 keV transition is a stretched E2, which defines J^{π} as $17/2^{+}$ for the 1345.5 keV level. The 4-point distribution for the 229.6 keV transition supports this conclusion, and eliminates the possibility of a $9/2^{+}$ assignment which would fit the 494 keV data reasonably well.

The 1210 keV state is deexcited by four transitions, most of which are too weak to yield good angular distribution or internal conversion data. The best evidence for the J^{π} assignment of $11/2^{-}$ is found from the 358.0 keV transition which deexcites to the 852.0 ($13/2^{+}$) state by an E1 transition. The entire decay pattern for this state supports the assignment. This state is strongly populated by an $\ell = 5$ transfer in the (d,t) and (^{3}He,α) experiments and has also been assigned $J^{\pi} = 11/2^{-}$ by Løvhøiden and Burke (1975).

The 1210 keV state is populated by a sequence of transitions which form a well developed rotational band whose higher members decay only by intra-band transitions. This sequence is defined by a cascade of predominantly M1 transitions of energies 253, 262, 278, 291, 305 and 315, most of whose multipolarities are defined by angular distributions and internal conversion data, and a weaker set of crossover transitions of energy 515, 541, 569, 596, 620 and 638 keV, which were in the main too weak to yield angular distribution and internal conversion data. These states are shown at the right of Figure 5-18 and two of the distributions are presented in Fig. 5-13.

The 1364 keV state decays to the 785 keV ($11/2^+$), 902 ($13/2^-$) and 1116 ($13/2^+$) states. The E1 transition (462 keV) to the 902 keV state shown in Fig. 5-12 clearly defines its spin as $11/2^+$ or $15/2^+$. The 579 keV stretched E2 eliminates the $11/2^+$ choice, and the 248 keV transition to the 1116 keV level is consistent with the $15/2^+$ assignment. The absence of transitions to low lying negative parity states of spin 7/2, 9/2 and 11/2 is also consistent with the assignment.

The 1425 keV state is identified purely on the existence of 719-706 keV coincidences with a coincidence probability of $\sim$2. The presence of these coincidences indicate that either the 706 or the 719 keV gamma ray of Table 5-1 is a doublet. In either case, the level defined is at 1425 keV. We cannot assign a spin or parity to this state.

The 1434.9 keV state is based on 583-146 and 729-706 keV cascades. The data of Table 5-1 and Fig. 5-12 show clearly that the 729 keV transition is a stretched E2 and that the 583 keV transition is dipole.

These facts define J^{π} as $15/2^{-}$ for this level.

The 1505.9 keV state is defined by the 604-523 and 721-406 keV cascades. The 604 keV transition appears to be dipole in character but no internal conversion data exists. The data available limits J^{π} to $11/2^{\pm}$, $13/2^{\pm}$ or $15/2^{+}$ with the expectation that the higher spin choices are more likely.

The 1511.0 keV level is deexcited by the strong 609 keV transition and two much weaker lines. Fig. 5-13 and Table 5-1 show that the 609 keV transition to a $13/2^{-}$ state is stretched E2 in character, thus defining $J^{\pi} = 17/2^{-}$ for the 1511.0 keV state. The $9/2^{-}$ choice is inconsistent with the pattern of deexciting gamma rays since it would result in a large number of unobserved transitions.

The 347-379 keV cascade which couples the 1511 keV ($17/2^{-}$) state to the 785 ($11/2^{+}$) state defines an intermediate level at either 1131.5 ($15/2^{+}$) or 1164 ($13/2^{-}$) keV. These restrictions on J^{π} follow from the fact that the angular distribution of the 347 keV transition is characteristic of a stretched E2. The 379 keV transition is completely masked in the direct spectra by the much stronger 379 → 0 keV transition, the assigned intensity of 2.5 being based on coincidence probabilities. One can make a weak argument against the first choice from the absence of a 720 keV transition between the 1851 ($19/2^{+}$) and 1131 ($15/2^{+}$) states. In this case the 1131 keV state would become the $15/2^{+}$ Yrast level and one would expect the 720 keV transition to it to be very strong.

The 1676.7 keV state is defined by the 561-331 and 331-494 keV cascades. The 4-point distribution and the internal conversion data for the 561 keV transition indicates that it is a stretched E2. J^π for this state is thus $17/2^+$.

The 1851.0 keV state is deexcited by 341-609, 488-462 and 506-494 keV cascades. The internal conversion coefficients and angular distribution data of the 341 and 488 keV transitions clearly define J^π for the state as $19/2^+$ (Fig. 5-13).

The 1853.0 keV level is established solely by the strong 508-494 keV cascade. The 508 keV transition is a stretched E2 and therefore J^π for this state is $21/2^+$. There is no possibility that the 1851 and 1853 keV states actually are one state.

The 2077.7 keV state is based solely on evidence for the 643-729-706 keV cascade. No internal conversion data exists for the 643 keV transition but the angular distribution fits a stretched E2 distribution. The state is therefore assigned $J^\pi = 19/2^-$.

The 2297.4 and 2325.1 keV states are based on the 786-609 and 473-488 keV cascades respectively. The angular distributions of both the 786 and 473 keV transitions are stretched E2, and lead to $21/2^-$ and $23/2^+$ assignments for these two states.

The 2405.5 keV state is defined by the 552-508 keV cascade. Although the intensity of the 552 keV transition is relatively large (2%), it is masked in the direct spectrum by a strong 553 keV gamma ray in the ground state band of ^{152}Gd. This level was also observed by Kleinheinz et al (1974) who assigned it $J^\pi = 25/2^+$. Since they were using the (α,3n) reaction to populate this state, it is likely that the ^{152}Gd contaminant in their experiment would have been weaker than in ours. The level at 2197 keV is based on coincidence data involving two weak gamma rays for which neither internal conversion nor angular distribution data exists. The spin assignment of $21/2^+$ for this state is thus very insecure.

Although the spin assignments for a number of high spin states made above would appear to be based on rather weak grounds, we have been considerably influenced by the fact that these states appear in the (α,3n) work of Kleinheinz et al as members of structures that extend to spin values of two to four units higher than we can excite in our work. The only level seen by Kleinheinz et al (1974) below 2000 keV which we have not included is the 1990 keV state. It is presumably based on a 479-609 keV cascade which we do not observe. It is possible that the 479-609 keV cascade was much stronger in the (α,3n) experiments.

The coincidence data has made it possible to place all the transitions of intensity greater than 1.7% which have excitation functions typical of the (α,2n) process. There are seven unidentified transitions of intensity 1 to 1.7% and six of lower intensities. A number of these are in coincidence with the 379 keV transition but the data does not permit one to identify the levels from which they come.

Chapter 6

DISCUSSION OF EXPERIMENTAL RESULTS

6.1 Introduction

In this study of ^{151}Gd approximately 40 levels have been identified. The interpretation in terms of existing models is not clear cut. In its ground state ^{151}Gd is considered to be a spherical nucleus. However it borders on the mass region wherein there is a rapid transformation to stable deformed ground state configurations. The data presented in Chapter 5 indicate a large number of intense stretched E2 transitions which suggests collective motion among the nucleons. It is possible on the basis of the coincidence spectra to group levels into band-like structures but these cannot be closely predicted in most cases by existing models of nucleon motions.

The level structure in ^{151}Gd can be described to a limited extent by means of the Nilsson model with pairing and Coriolis coupling included. It is not possible to obtain a complete description of the observed states with a single choice of deformation.

The variable moment of inertia model (Mariscotti et al. (1969)) which is applicable to "soft nuclei" works well for the $11/2^-$ band and may be applicable to one or two other structures. The decoupled band theory of Stephens and Diamond does not apply in ^{151}Gd, although there are many structures which bear a superficial resemblance to the so-called "decoupled bands". The following sections will outline the extent to which it has been possible to interpret the levels in ^{151}Gd in terms of these models

6.2 Properties of Coriolis Coupling Calculations

To aid the reader in understanding the interpretation of the data a brief review of the consequences of the Coriolis interaction is presented. The discussion relates to orbitals originating from the $i_{13/2}$, $f_{7/2}$ and $h_{9/2}$ shell model states which exist near the Fermi surface of N = 87 odd A nuclei. Some of these will be hole states others particle states depending on the deformation of the nucleus. The behaviour of a hole state is analogous to that of a particle state with the sign of the deformation reversed.

6.2.1 The Effect of Coriolis Coupling on the Composition of States

The Coriolis interaction destroys the purity of the wave function of a state by mixing in, to varying degrees, the wave functions of other states having the same parity and K value differing by 0 or 1 unit. This implies the mixing not only of wave functions of states originating from the same shell model state but also of wave functions of states arising from other shell model states which have the same parity e.g. the $f_{7/2}$ and $h_{9/2}$ shell model states. The degree of mixing is a function of the energy separation of the states and the deformation of the nucleus. The mixing of the nearest $\Delta K = 1$ orbitals arising from the same shell model state is the more important effect with diminishing contributions from the components which exist at successively higher excitations. As the deformation of the nucleus increases so also does the mixing of other components from both sources. At a deformation of $\delta \sim .2$ both types of mixing make approximately equal contributions with the result that the wave function of a particular state cannot be identified with any particular orbital. Furthermore transitions which should be forbidden by the K selection rules are permitted since the states involved can no longer be characterized by a single K value. It is characteristic of the above mentioned orbitals that for small deformations ($\delta \sim .10$) both types of mixing are minimal.

6.2.2 The Effects of Decoupling on the Energies of States

The Coriolis interaction has a diagonal contribution from K=1/2 orbitals. The effect is to decouple the motion of the particle (or hole) from the motion of the core. This is characterized by an increase in the excitation of alternate spin members of a rotational band built on the orbital. The effect can be small in cases where the K=1/2 orbital is a minor component of a mixed wave function. The normal rotational band pattern is only slightly perturbed in such cases. The effect can also be quite large if the rotational band is built on a state the major component of which is K=1/2. For a small prolate deformation, the large decoupling effects can lift half of the states to such high excitations that they are not populated experimentally. If there is only one shell model state involved (e.g. the $i_{13/2}$ case) the remaining half form a sequence of states with spin I = j, j+2, j+4 etc. which are coupled by E2 transitions. If there are two or more shell model states involved (e.g. the $f_{7/2}$ and $h_{9/2}$ cases) the low lying states will form two spin sequences: I = j, j+2, j+4 and I = j+1, j+3 etc. Superficially these may appear to form a single rotational band. However if the

Coriolis mixing between the two shell model states is weak (e.g. at small deformations), the $\Delta I=1$ transitions between the two $\Delta I=2$ sequences may also be weak and not be observable. As the degree of mixing increases the $\Delta I=1$ transitions will increase in intensity.

6.3 The Negative Parity States

The data of chapter five establish a sequence of levels at 1210, 1463, 1726, 2004, 2295 and 2600 keV with energies which roughly follow an I(I+1) rotational band spacing. The band head has $J^{\pi}=11/2^{-}$ and each state is connected to the next by an M1 transition. None of the states in this sequence decays to states outside of the group with the exception of the band head. This indicates very little mixing with other states of the nucleus.

The data also indicate that the 7/2, 11/2 15/2 and 19/2 sequence of negative parity states connected by the 379, 523, 609 and 786 keV transitions are very weakly coupled to the $9/2^{-}$, $13/2^{-}$, $17/2^{-}$ sequence connected by the 706, 729 and 643 keV transitions. This is unusual since a full sequence of spins is present and one would ordinarily expect to see the strong M1 transitions between the alternate members of the two sets of states.

Furthermore the negative parity states at 427, 671, 719 and 1077 keV do not interact with each other or with the above mentioned cascades except where it is possible to de-excite to the ground state in the most direct manner.

Based on the discussion of section 6.2 this evidence suggests that the nucleus may be only slightly deformed when these states are populated.

The Coriolis coupling program has been used to calculate the relative positions of the negative parity states. Pairing correlations were included. One calculation employed all the orbitals originating from the $h_{11/2}$ shell model state with a rotational parameter which reproduced the spacing of the 1210 and 1463 keV states.

Another calculation used all the orbitals originating from the $f_{7/2}$ and $h_{9/2}$ shell model states. Both sets were included in the same calculation because they are very close in excitation and are expected to interact through the Coriolis force. A rotational parameter was chosen to reproduce the spacing of the 379 and 902 keV levels at a deformation of +0.10. The Fermi level was set on the 3/2 [521] orbital based on the normal filling of Nilsson states. The other parameters (μ, κ and attenuation) were set to accepted values. The zero of energy was chosen to match the excitation of the first $9/2^-$ level at 379 keV.

6.3.1 The $11/2^-$ [505] Band

The data establish a sequence of levels based on the state at 1210 keV with energies which roughly follow an I(I+1) rotational band spacing.

The fact that this band is not strongly decoupled is evidence that it cannot be based on a low K Nilsson orbital originating in the $h_{9/2}$ shell. Furthermore, the $11/2^-$ [505] state which is related to the $h_{11/2}$ shell model state should lie below the Fermi surface and be a strongly populated hole state in this reaction. It is strongly populated in the (^{3}He,α) reaction studied by Burke et al (1975).

Using the program SNOOPY[+] it is possible to calculate the positions of the members of the rotational band built on the $11/2^-$ orbital. In this calculation all orbitals of the $h_{11/2}$ shell were included. The deformation was estimated using the general empirical relationship (Stephens et al,1972) between the 2^+ energies and the E2 transition lifetimes, which essentially all even-even nuclei follow.

$$\beta \sim \left(\frac{1225}{6(\hbar^2/2I)^{7/3}} \right)^{1/2}$$

For this case $\beta = 0.29$ using $E_{13/2 \to 11/2} = 13\hbar^2/2I = 253$ keV. Since the deformed core is the even-even nucleus ${}^{150}_{64}\mathrm{Gd}_{86}$ this expression should remain valid.

A comparison of the experimental energy levels relative to the bandhead and the predictions of the Nilsson model calculation is presented in Fig. 6-1. All spin members are accounted for although the predicted spacing becomes increasingly greater than the observed spacing. Table 6-1 presents the amplitude of the components of the wave functions which are mixed in these levels.

[+] Nilsson model program incorporating Coriolis coupling and pairing,written in Bergen, Norway. Standard parameters were used κ=0.06, μ = 0.42 and attenuation = 0.75.

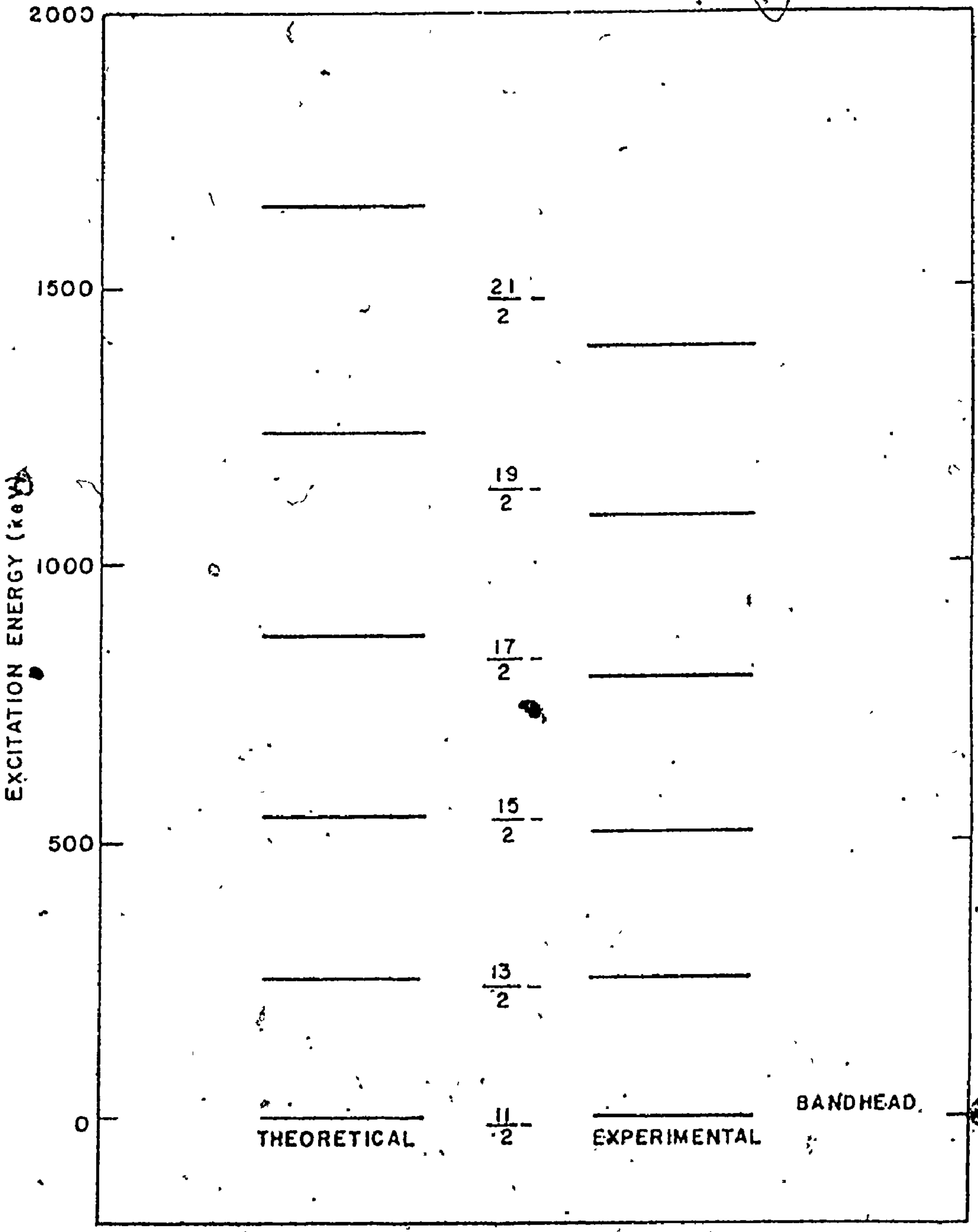

Figure 6-1

A comparison of the calculated and experimental energy levels of the $11/2^-[505]$ rotational band relative to the bandhead.

Table 6-1

	21/2	19/2	17/2	15/2	13/2	11/2
11/2[505]	0.97	0.98	0.98	0.99	0.99	1.00
9/2[514]	0.24	0.21	0.19	0.16	0.12	0.08
7/2[523]	0.05	0.04	0.03	0.02	0.01	0.01
5/2[532]	0.00	0.00	0.00	0.00	0.00	0.00
3/2[541]	0.00	0.00	0.00	0.00	0.00	0.00
1/2[550]	0.00	0.00	0.00	0.00	0.00	0.00

The model predicts that the excitation of the $9/2^-$[514] state occurs 1650 keV above the $11/2^-$[505] ground state and that the other Nilsson states involved are at still higher energies. Hence it is not surprising that the wave functions for members of this band are dominated by the $11/2^-$ component. One might expect to see transitions of energy ~1500 keV between the $9/2^-$[514] and $11/2^-$[505] band heads. However, states at this level of excitation are very weakly populated in our experiment and the detection efficiency for the high energy transitions involved was low.

For a rigid rotor, the angular momentum dependence of the excitation energy is given by $E(I) = \frac{\hbar^2}{2\mathcal{I}} I(I+1) = AI(I+1)$ where $\mathcal{I}$ is the moment of inertia of the rotor and A is the rotational parameter. Rearrangement of this expression leads to

$$[E(I) - E(I-1)]/2I = \frac{\hbar^2}{2\mathcal{I}} = A$$

Since for a non-rigid rotor one can expect $\mathcal{I}$ and hence A, to vary with spin, a plot of $[E(I) - E(I+1)]\ /2\mathcal{I}$ versus I gives a graphical representation of how the moment of inertia changes with I. It is obviously convenient to express A in keV and $\frac{2\mathcal{I}}{\hbar^2}$ in $(\mathrm{keV})^{-1}$.

A plot of A versus I is shown in Fig. 6-2 for the $11/2^-$ bands in the gadolinium nuclei with neutron number 87, 89 and 91. The data show clearly that there is a systematic reduction in A (an increase in $\mathcal{I}$) as the spin of the nucleus increases and that the rate of this change is greatest for ^{151}Gd with 87 neutrons. Thus ^{151}Gd is much "softer" against shape changes than ^{153}Gd or ^{155}Gd which have respectively two and four additional neutrons in the core.

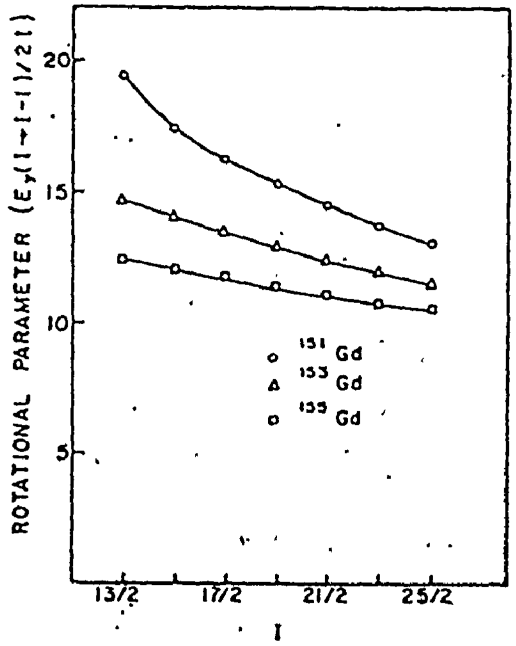

Figure 6-2: Rotational parameters for ^{151}Gd, ^{153}Gd, and ^{155}Gd.

For the VMI fit, to the energy levels of this rotational band, the first three excitation energies were used to generate the parameters I_K and C which determine the function $I(I)$. The remaining four levels were predicted on the basis of these parameters and therefore represent a test of the theory. Table 6-2 includes the predicted energies both for the states populated in the present work and the $25/2^-$ state identified by Kleinheinz et al (1974). The agreement between the predicted and experimental values is gratifying.

Table 6-2

Variable Moment of Inertia Fit to the $11/2^-[505]$ Band

Excitation Energy (keV)	Spin	VMI Fit
253.2	13/2	252.5
515.6	15/2	516.4
793.7	17/2	793.3
1085.1	19/2	1083.5
1390.1	21/2	1386.5
1705.3	23/2	1702.0
2027	25/2	2029.6

Fig. 6-3 presents the values of $\mathcal{I}$ as a function of $2\mathcal{I}$ derived from the VMI model, shown as the solid curve. These values are derived from equation 3-27.

The figure also shows the experimental values of $\mathcal{I}$ derived from the rotational parameters of Fig. 6-2. Each experimental $\mathcal{I}$ value has been associated with the spin midway between that of the initial and final state used to obtain $\mathcal{I}$.

The agreement between the variable moment of inertia calculation and the experimental values is impressive.

An alternate method of studying this structure is to adapt the variables used for the testing of "back-bending" in even-even nuclei to our purpose. For such nuclei, it has been customary to plot:

$$2\mathcal{I}/\hbar^2 \quad \text{vs} \quad \hbar^2\omega^2$$

where $2\mathcal{I}/\hbar^2 = (4I - 2)/(E_I - E_{I-2})$ and $\hbar^2\omega^2 = (E_I - E_{I-2})^2 f(I)$. Several different forms of f(I) are in common use, all designed to make $2\mathcal{I}/\hbar^2$ a linear function of $\hbar^2\omega^2$ at small I values (Sorensen, (1973)).

These formulae are not valid for nuclei with half-integral spins and it is a non-trivial exercise to find a function f(I) suitable for such cases. Volkov has proposed a theoretically justifiable modification of the Sorensen function which leads to a linear relation between $2\mathcal{I}/\hbar^2$ and $\hbar^2\omega^2$ as follows. We define

$$I = N+K \qquad N = 0,1,2\ldots$$

$$2\mathcal{I}/\hbar^2 = (2N+2K) / (E_N - E_{N-1})$$

$$\hbar^2\omega^2 = (E_N - E_{N-1})^2 f(I,K)$$

$$f(I,K) = (N+K)(4/3)^3 \Big/ \left(\{N(N+2K+1)\}^{2/3} - \{(N-1)(N+2K)\}^{2/3} \right)^3$$

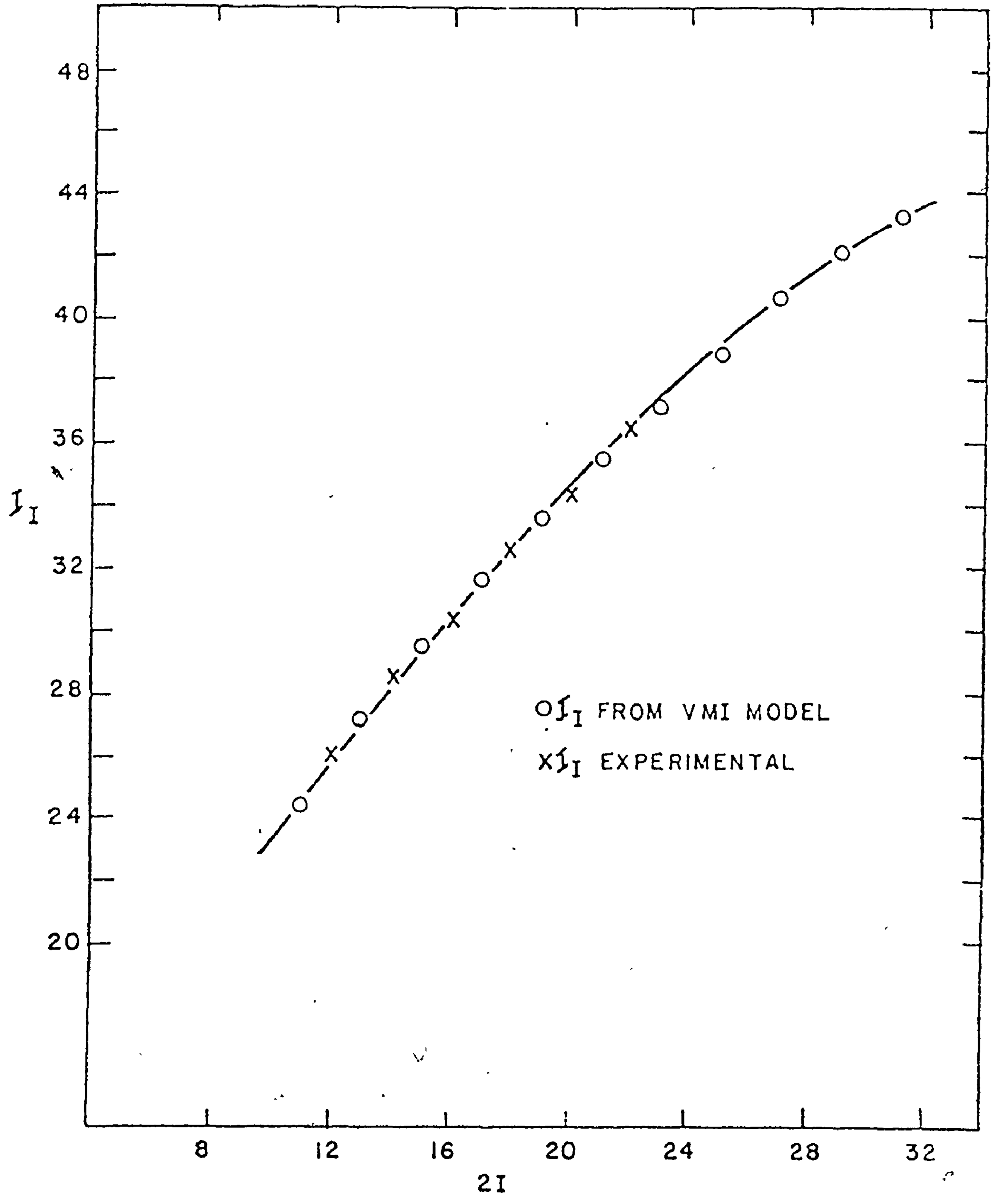

Figure 6-3

A comparison of the moments of inertia for the various states of the $11/2^-[505]$ rotational band as calulated by the VMI fit to the level energies and as determined from the rotational parameters of Fig. 6-2.

Fig. 6-4 presents the results of applying this analysis to the $11/2^-$ [505] band in ^{151}Gd, ^{155}Gd and ^{149}Sm, ^{151}Sm. The data have been drawn from various sources, as indicated in Table 6-3. All cases show the same characteristic behaviour, with a linear section up to $\hbar^2\omega^2 \sim 0.06$ followed by a concave section reminiscent of the onset of back bending. The solid curves represent the least squares fit of the lower spin points to the linear function $2I/\hbar^2 = 2I_o/\hbar^2 + C\hbar^2\omega^2$ and Table 6-3 tabulates the results of the fitting procedure. The most remarkable feature of Table 6-3 is the constancy of the parameter C over the range of nuclei shown. It can be associated with the "softness" of the nucleus to deformation and the deformation parameter, β, can be associated with ($2I_o/\hbar^2$) through the relation defined in equation 6-1.

The value of β appears to be independent of the proton number but increases steadily with the addition of neutrons in both Samarium and Gadolinium. Since β is related to the intrinsic quadrupole moment through the expression $Q_o = 3Z.R_o^2A^{2/3}\beta/\sqrt{5\pi}$, one can readily calculate these moments for these nuclei.

The first two comumns of Table 6-4 present the spin assignments and transition energies for the M1 + E2 cascade members of the $11/2^-$ [505] band in ^{151}Gd. The third and fourth columns present the experimental mixing ratios obtained from the internal conversion and angular distribution data of Table 5-1. The fifth column presents the values of δ deduced from the ratio of the cross-over to the cascade photon intensities using the unified model for bands with pure K (Alexander, Boehm and Kankeleit, (1964)). The values of δ deduced from this model are a

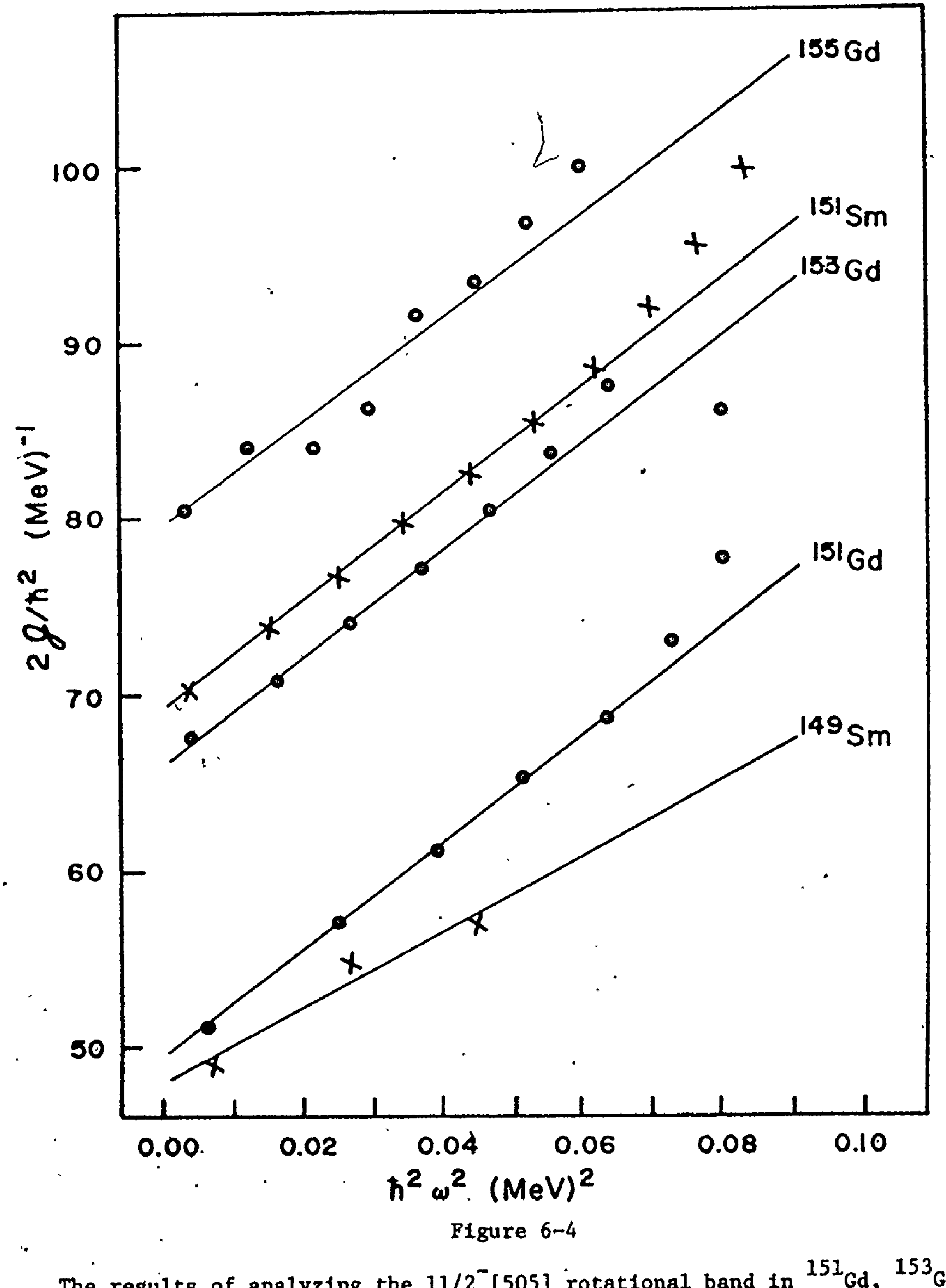

Figure 6-4

The results of analyzing the 11/2$^-$[505] rotational band in ^{151}Gd, ^{153}Gd, ^{155}Gd, ^{149}Sm and ^{151}Sm using the modified Sorenson function.

Table 6-3

Nuclear parameters for the $11/2^-[505]$ band

Nucleus	$\frac{2I_0}{\hbar^2}$ $(MeV)^{-1}$	C $(MeV)^{-3}$	β	Q_0 bns	Number of Transitions identified	Number of Transitions fitted	Source of Data
${}^{149}_{62}Sm_{87}$	48.2±1.5	215±51	0.288	5.45	3[a]	3	Thompson et al, 1975
${}^{151}_{62}Sm_{89}$	69.5±0.1	304±3	0.341	6.52	10	6	Cook et al, 1975
${}^{151}_{64}Gd_{87}$	49.6±0.3	305±5	0.288	5.70	7	5	Smith et al, 1973
${}^{153}_{64}Gd_{89}$	66.3±0.2	302±9	0.330	6.52	8	5	Løvhøiden et al, 1972
${}^{155}_{64}Gd_{91}$	79.5±13	301±46	0.354	7.08	8	6	Løvhøiden et al, 1970

a) We have been unable to identify the three additional transitions in this band reported by Kleinheinz et al in the Julich Annual Report for 1974.

Table 6-4

A Comparison of Experimental and Theoretical Mixing Ratios

I_i I_f	E (keV)	$\|\delta\|$ (α_K)	$\delta^{a)}$ $(\gamma(\theta))$	$\|\delta\|$ (model)	$\|(g_K - g_R)/Q_o\|$ from $\delta_{\gamma(\theta)}$	from δ_{Model}
13/2→11/2	253.2	0.7±0.4	+0.22±.05		0.17±.04	
15/2→13/2	262.4	<0.3	+0.18±.05	0.41±0.05	0.18±.04	.08±010
17/2→15/2	278.0	<0.3		0.35±.04		.088±.010
19/2→17/2	291.4	<0.3	+0.13±0.13	0.37±.04	0.21±.21	.078±.010
21/2→19/2	304.9		<+0.16	0.37±.04	>.17	.073±.010
23/2→21/2	315.1		−0.12±0.28		>.16	

a) Limits of error on δ correspond to the 0.1% confidence limit.

factor of ∿ 2.2 larger than those extracted from the angular distribution data, and lead to quite different estimates of $|(g_K-g_R)/Q_o|$ as is shown in the last two columns of Table 6-4. This discrepancy cannot be explained.

Data from our earlier publication (Smith et al,1973) is reproduced in Table 6-5. It shows that the values of $|(g_K-g_R)/Q_o|$ derived from the gamma ray branching ratios are essentially the same for ^{151}Gd, ^{153}Gd and ^{155}Gd. Unfortunately, the published angular distributions for the two heavier gadolinium nuclei are so limited that one cannot determine whether or not a similar discrepancy would exist in the value of δ for these cases.

The 11/2$^-$[505] state exists at quite low excitation energies in ^{153}Gd and ^{155}Gd (171 keV and 121 keV, respectively) and is known to be isomeric because of K forbiddenness, Løvhøiden et al (1970) and Løvhøiden et al (1972). In the present experiment the resolving time of the γ-γ coincidence circuit sets an upper limit of 50nsec for the 1210 keV level in ^{151}Gd. The main mode of decay for the 1210 keV level is via the 830 keV M1 transition to the level at 379 keV. The Weisskopf estimate for the half-life of an 830 keV M1 transition is in the picosecond range. Even if this estimate were increased several orders of magnitude as a result of shape hindrance of the transition, the lifetime of the 1210 keV level would be too short to have been observed. The large difference in excitation energy for the 11/2$^-$[505] states in ^{153}Gd and ^{151}Gd may be related to a change in deformation,since the single particle energy for this state varies strongly with this parameter.

Table 6-5

Mixing Ratios and g-factors for the $11/2^-[505]$ Band

Transition $I_i \rightarrow I_f$	Energy (keV)	δ^2	$\lvert (g_K - g_R)/Q_0 \rvert$
$13/2 \rightarrow 11/2$	253.2		
$15/2 \rightarrow 13/2$	262.4	0.17±0.04	0.081±0.010
$17/2 \rightarrow 15/2$	278.0	0.12±0.03	0.088±0.010
$19/2 \rightarrow 17/2$	291.4	0.14±0.03	0.077±0.010
$21/2 \rightarrow 19/2$	304.8	0.14±0.03	0.073±0.010

Nuclide	Mean Value $\lvert (g_K - g_R)/Q_o \rvert$
^{151}Gd	0.080±0.010
^{153}Gd	0.076±0.011
^{155}Gd	0.076±0.006

It could also be due to the difference in energy for spherical and deformed potential surfaces.

6.3.2 States Which Exhibit Coriolis Coupling

The results of the Coriolis coupling calculation which involved both the $h_{9/2}$ and $f_{7/2}$ orbitals are presented together in Table 6-6 in order to facilitate comparison. Part a) of the table contains the calculated level energies and identifies each level with the shell model state which provides the largest components in its wave function. Part b) of the table shows the composition of each state in terms of the Nilsson orbitals included in the basis. It can be seen that the wave function associated with each state has large components belonging to one shell model state and small components of the other. Thus one may feel justified in associating each state with either the $h_{9/2}$ or $f_{7/2}$ shell model states.

The low lying states associated with the $h_{9/2}$ and $f_{7/2}$ shell model states form a complete sequence of spin values which resemble a mildly decoupled band. However part a) of the table shows that every other member of each set is raised to high excitation to produce this effect. Part b) of the table shows that little mixing occurs between the two sets of states, hence each state prefers to decay to the other members of its own sub-band via E2 transitions.

6.3.2.1 States Related to the $h_{9/2}$ Orbitals

The low lying $9/2^-$,$13/2^-$,$17/2^-$ and $21/2^-$ states based on the 1/2[530] orbital of the $h_{9/2}$ shell model state have been identified with the levels at 379,902,1511 and 2297 keV respectively. The energies calculated for each of these states show a systematic increase over the measured values. This is to be expected since the program

Table 6-6(a)

Energies of the Bands Built on the $f_{7/2}$ and $h_{9/2}$ K=1/2 Bands

I	E(keV)	
	1/2[541]	1/2[530]
1/2	950.3	790.5
3/2	346.2	1859.1
5/2	2011.6	309.1
7/2	366.5	3300.8
9/2	3515.5	379.4
11/2	853.4	5186.0
13/2	5444.1	908.4
15/2	1787.5	7508.9
17/2	7804.5	1883.6
19/2	3164.5	10270.1
21/2	10602.9	3301.6

Table 6-6(b)

Composition of the Negative Parity Yrast Levels

f7/2	h9/2	1/2	3/2	5/2	7/2	9/2	11/2	13/2	15/2	17/2	19/2	21/2
		SPIN										
1/2[541]		.34	.87	.13	.80	.11	.79	.10	.79	.10	.79	.10
	1/2 [530]	.94	-.06	.75	-.05	.75	-.05	.75	-.05	.75	-.06	.7
3/2[532]		.00	.49	.26	.53	.21	.53	.19	.53	.18	.75	.1
	3/2 [521]	.00	-.08	.53	-.07	.53	-.07	.52	-.07	.52	-.08	.5
5/2[523]		.00	.00	.19	.25	.19	.27	.18	.27	.18	.27	.1
	5/2 [512]	.00	.00	.19	-.05	.25	-.05	.26	-.05	.27	-.05	.2
7/2[514]		.00	.00	.00	.06	.09	.08	.10	.09	.11	.10	.1
	7/2 [503]	.00	.00	.00	.01	-.06	.02	-.08	.02	-.09	.02	-.0
	9/2 [505]	.00	.00	.00	.00	.02	.01	.03	.02	.04	.02	.0

employs a rigid rotor formula and cannot account for the compression resulting from the gradually increasing moment of inertia as illustrated by the VMI analysis of the $11/2^-[505]$ rotational band.

The program also calculates low lying $1/2^-$ and $5/2^-$ states at energies of 790 and 309 keV respectively. These have been identified tentatively with the observed $1/2^-$ and $5/2^-$ levels at 575 and 108 keV. A recent paper by Afanasiev et al (1975) has shown that these two states are collective in nature. Fig. 6-5 presents a comparison of the experimental negative parity level energies and the calculated values. The calculated positions of the $1/2^-$ and $5/2^-$ states seem to agree quite well with the observed values however the evidence for the assignment is regarded as weak.

6.3.2.2States Related to the $f_{7/2}$ Orbitals

The low lying $11/2^-$, $15/2^-$ and $19/2^-$ state based on the 1/2[541] orbital of the $f_{7/2}$ shell model state have been identified with the levels at 706, 1435 and 2078 keV respectively. The calculated energies for these states also show a systematic increase over the observed level energies. The program also calculates low lying $3/2^-$ and $7/2^-$ states at energies of 346 and 366 keV respectively. These may correspond to the states at 395(3/2-) and 427(5/2- or 7/2-). However as a result of the uncertainty in the spin of the 427 keV state no conclusion is possible at the the present time.

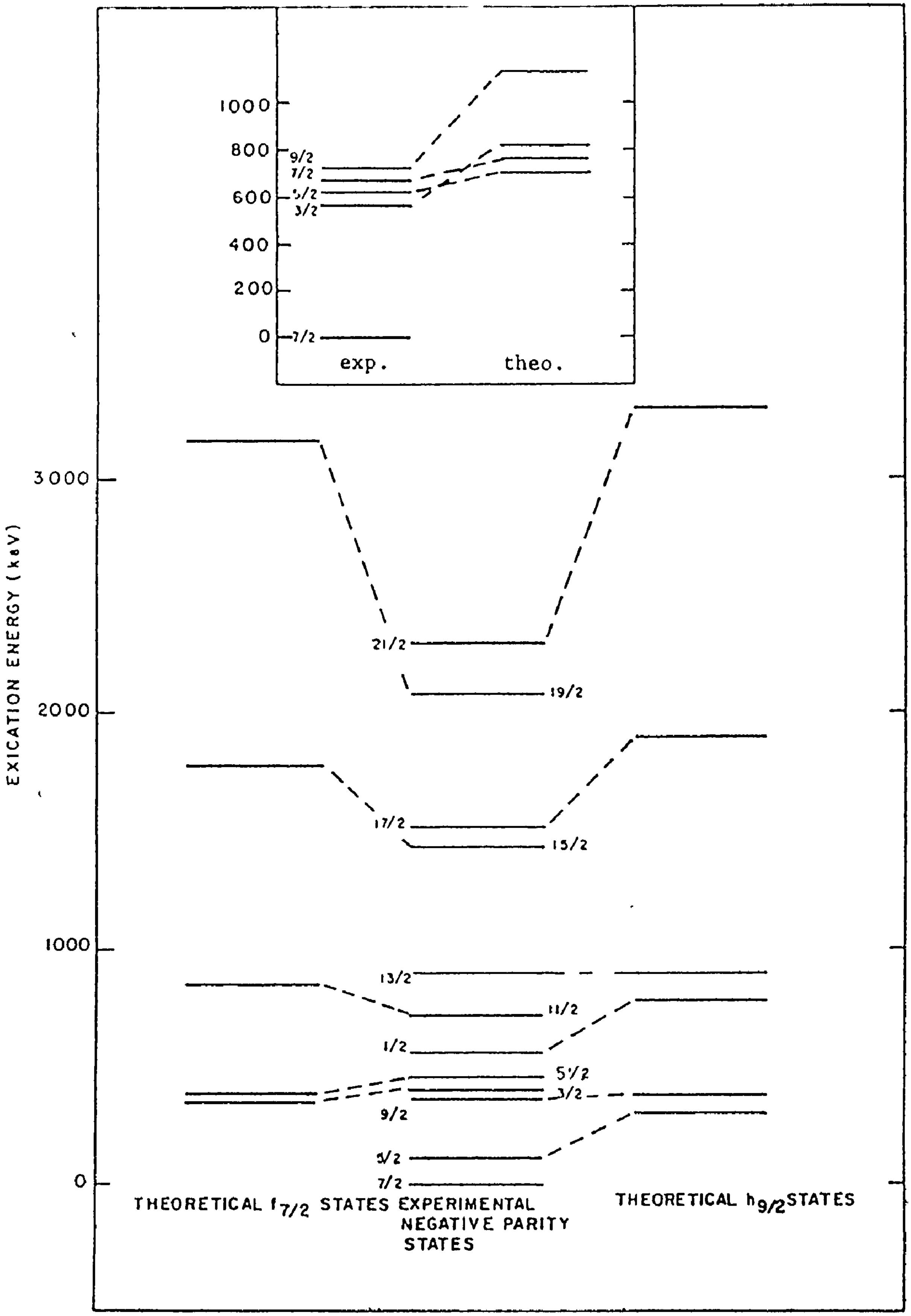

Figure 6-5

A comparison of the calculated and experimental excitation energies of the negative parity $f_{7/2}$ and $h_{9/2}$ orbitals.

6.3.3 Other Negative Parity States

There are six remaining negative parity states at 587 (3/2), 617 (5/2), 671 (7/2), 719 (9/2), 1077 (13/2) and 1164 (13/2) keV. The first four of these may have counterparts among the levels calculated from the $f_{7/2}$ and $h_{9/2}$ orbitals (see insert Fig. 6-5). These are highly mixed states which may be roughly designated as K = 3/2, K = 3/2, K = 5/2 and K = 3/2 but about which little else can be said.

For the states at 1077, and 1164 keV the model offers no explanation since the next lowest $13/2^-$ state is calculated to occur at $\sim$ 2030 keV.

In conclusion the standard Nilsson model calculation with Coriolis coupling and pairing does not provide a very good explanation of the observed states.

The assymetric rotor model of Meyer ter Vehn (1974) provides a mechanism for obtaining several $9/2^-$ and $13/2^-$ states. However, the data is not yet complete enough at this state to test the validity of this model.

6.4 The Positive Parity States

The positive parity states which are shown in Fig. 5-18 and appear again in the central portion of Fig. 6-6, form a very interesting but puzzling structure. Kleinheinz et al (1974) accounted for the 852 (13/2), 1346 (17/2), 1853 (21/2), 2405 (25/2), 3006 (29/2) sequence shown at the left of this section of Fig. 6-6 in terms of the decoupled band model but assigned negative parity to all the remaining positive parity states shown in Fig. 6-6. Their assignments became untenable with the discovery that the strong 406 keV transition and a number of others were E1 rather than M1 (Smith et al, 1975). As shown in Fig. 6-6, there is now a plethora of positive parity states; one $11/2^+$, two $13/2^+$, two $15/2^+$, two $17/2^+$, one $19/2^+$, two $21/2^+$ and single states of $23/2^+$, $25/2^+$, $27/2^+$ and $29/2^+$ if one includes the two high spin states observed by Kleinheinz et al in the (α,3n) reaction but not seen in the present work. These states can be arranged into three sequences, the one proposed by Kleinheinz and two others, as follows: 784($11/2^+$), 1364 ($15/2^+$), 1852 ($19/2^+$), 2325 ($23/2^+$), 2864 ($27/2^+$) and 1115 ($13/2^+$), 1677 ($17/2^+$), 2197 ($21/2^+$). In all three of these the decay proceeds mainly by stretched E2 transitions. However, strong inter-sequence transitions exist so that it is probably not correct to treat any of them in isolation.

The structure of Fig. 6-6 is dramatically different from that in the more neutron-rich nuclei of this mass region (e.g. ^{153}Sm, ^{153}Gd and ^{155}Dy with N = 89 and ^{155}Gd with N = 91). In these N = 89 and 91 nuclei, the $9/2^+$ state lies below the $13/2^+$ state and the $11/2^+$ state which is not populated is assumed to be located well above the $13/2^+$ state. The structure of these nuclei can be understood in terms of the Coriolis coupling of the $i_{13/2}$ orbitals with a prolate deformation. In ^{151}Gd with N = 87, the $11/2^+$ state lies <u>below</u> the lower $13/2^+$ which is known to have a considerable $i_{13/2}$ strength from the particle transfer data (Løvhøiden and Burke, (1974)). Moreover, our (α,2n) work indicates that there are two $13/2^+$ states instead of one.

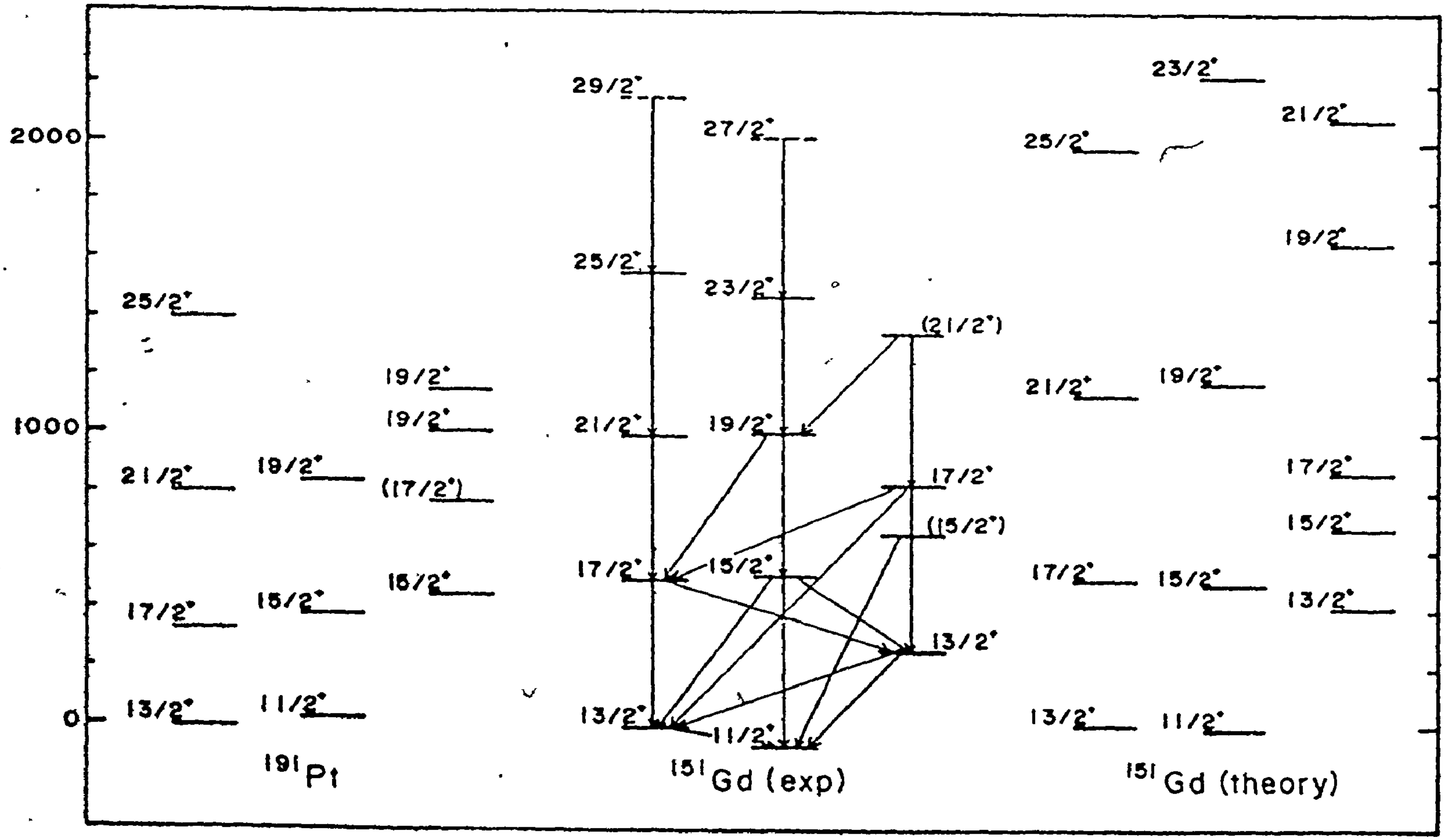

Figure 6-6

A comparison of the experimental excitation energies of the positive parity states in ^{151}Gd and ^{191}Pt and the values for ^{151}Gd calculated using the assymetric rotor model of Meyer ter Vehn,1975.

Although the decoupled band model correctly predicts the 13/2, 17/2, 21/2 . . . sequence, it requires that the 15/2, 19/2, 23/2 . . . levels as well as all states of spin less than 13/2 lie at high excitation. Thus, we must look for another interpretation.

Another possibility is to consider this structure as the result of the Coriolis interaction of a few particles in the $i_{13/2}$ shell of a nucleus with oblate deformation. Such a model would yield bands with K = 11/2 and K = 13/2 which would be mixed by Coriolis coupling with each other and with the other members of the $i_{13/2}$ bands. In this model, one might group the lowest 11/2, 13/2, 15/2, 17/2 . . . states into a K = 11/2 band which is distorted by mixing with the K = 1/2 orbital. Then one could regard the upper 13/2 state at 1116 keV as the K = 13/2 band head and build a second band on it. The results of this calculation are presented below with the calculation also performed at prolate deformation for completeness sake.

All the orbitals of the $i_{13/2}$ shell were included in the calculation and parameters were chosen as before. However, unlike the case of the negative parity states there is more than one state of a given spin. At opposite deformations different levels were suitable for determination of the rotational parameter.

For the calculations performed at positive (prolate) deformation the calculated level energies were normalized so that the excitation energy of the lowest $13/2^+$ state was 852 keV. A rotational parameter was chosen to reproduce closely the spacing between the $17/2^+$ state at 1346 keV and the $13/2^+$ state at 852 keV.

For the calculations performed at negative (oblate) deformation the calculated energies were normalized so that the excitation energy of the lowest $11/2^+$ state was 785 keV. A rotational parameter chosen to reproduce closely the spacing between the lowest $13/2^+$ state at 825 keV and the $11/2^+$ state at 785 keV.

6.4.1 Positive Parity States at Positve Deformation

The spacing between the $17/2^+$ and $13/2^+$ states at 1346 and 852 keV was inserted into the empirical formula of equation 6-1 in order to establish the deformation of the nucleus. A Coriolis coupling calculation was thus performed with a deformation of +.15. The results are presented in Table 6- 7.

As described earlier the 13/2, 17/2 and 21/2 states remain at low excitation energies while the 15/2, 19/2 and 23/2 states are pushed to high excitation energies as a result of the decoupling effect of the $1/2^+$ [660] orbital. Fig. 6-7 compares the calculated and measured excitation energies of the positive parity states. It can be seen that there is very little agreement. Relative excitations are poorly reproduced, the 11/2 state is far too high in excitation and the next lowest occurrence of a given spin value occurs at such high excitations that they were not included in the table. The calculation was repeated over a range of positive deformations but there was no value which produced a low lying $11/2^+$ state.

Figure 6-7

A comparison of the experimental excitation energies of the positive parity states and the values calculated using the Nilsson model with a deformation of $\delta = +0.15$.

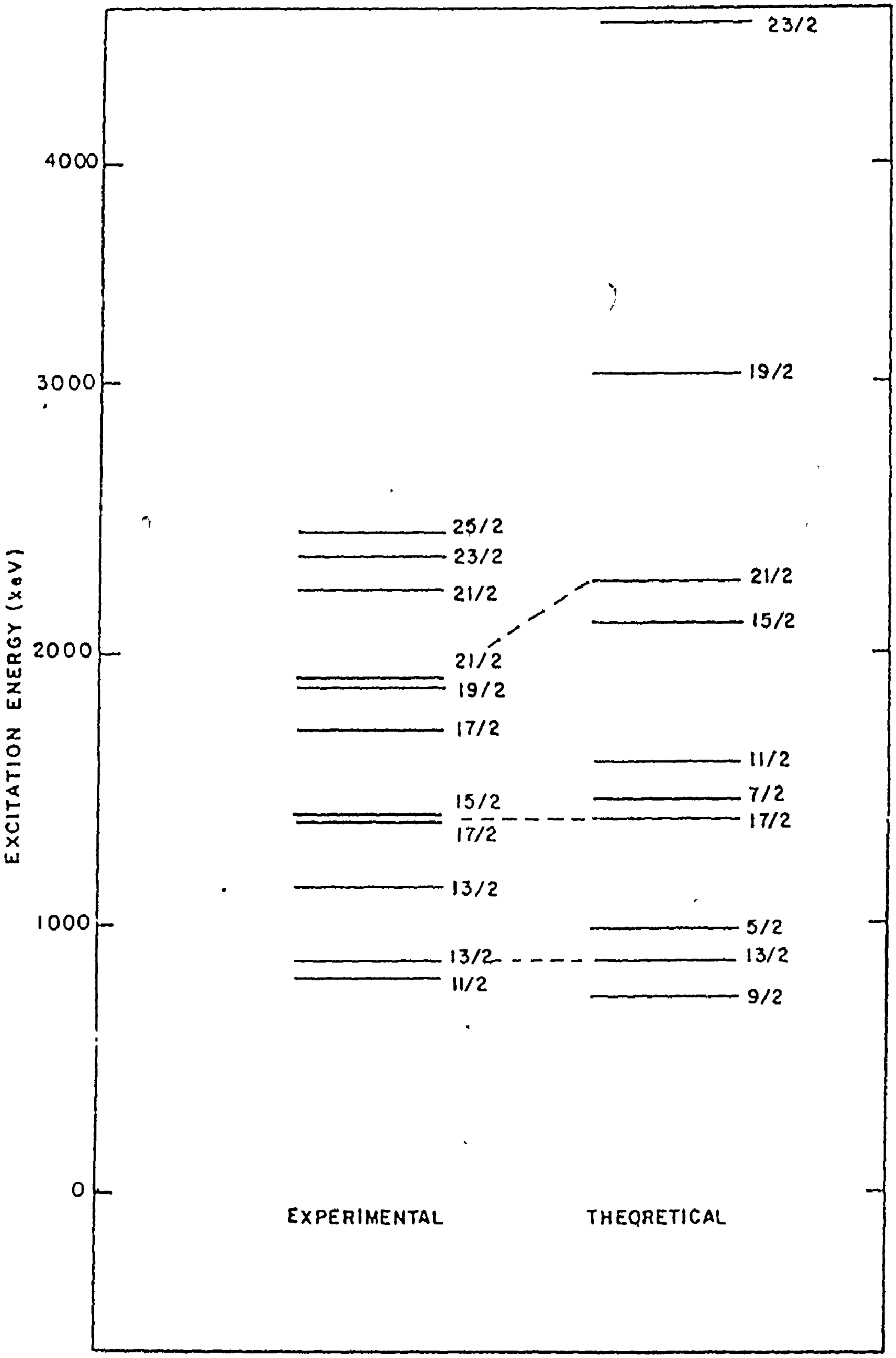
EXCITATION ENERGY (keV)
4000
3000
2000
1000
0
EXPERIMENTAL
THEORETICAL
25/2
23/2
21/2
21/2
19/2
17/2
15/2
17/2
13/2
13/2
11/2
23/2
19/2
21/2
15/2
11/2
7/2
17/2
5/2
13/2
9/2

Figure 6-7

Table 6-7

Energies and Compositions of the Lowest Positive Parity States at Positive Deformations

SPIN	ENERGY (keV)	COMPOSITION 1/2 [660]	3/2 [651]	5/2 [642]	7/2 [633]	9/2 [624]	11/2 [615]	13/2 [606]
1/2	1711.1	1.00						
3/2	1734.9	.36	.93					
5/2	981.1	.80	.56	.22				
7/2	1442.7	.25	.71	.61	.25			
9/2	723.2	.77	.56	.29	.10	.02		
11/2	1575.6	.22	.62	.63	.38	.14	.03	
13/2	852.0	.76	.55	.31	.13	.04	.01	
15/2	2094.1	.20	.58	.63	.43	.19	.06	.01
17/2	1355.9	.76	.55	.32	.15	.05	.01	
19/2	2989.1	.19	.55	.63	.46	.23	.08	.02
21/2	2231.3	.75	.54	.33	.16	.06	.02	
23/2	4256.9	.18	.54	.62	.47	.25	.09	.02

Normalized to the $13/2^+$ state at 852.0 keV. $\delta = +0.15$, $\lambda = 49300$, attenuation = 0.75, $\Delta = 46$ keV

6.4.2 Positive Parity States at Negative Deformations

The Coriolis coupling calculation was performed for the $i_{13/2}$ orbitals at a number of negative deformations. One obvious characteristic of these calculations was the fact that the $11/2^+$ state remained at low excitation since the 1/2+[660] orbital is much farther away from the Fermi surface. Another result was the existence of states of the same spin at low excitation. Figure 6-8 and Table 6-8 present the results of a calculation at a deformation of -0.15 which is the magnitude predicted by equation 6-1. This table includes the calculated excitation energies of states of each spin value and the next lowest occurrence of a given spin value if it is $\leq$ 1 MeV higher. The table also includes the composition of each state in terms of the $i_{13/2}$ orbitals included in the calculation. It is interesting to note that the lowest 13/2, 17/2, 21/2 and 25/2 all contain a large component of the 1/2+[660] orbital although there are considerable admixtures of other components. Each of these states is quite similar in composition so that we may expect them to decay strongly in cascade and less strongly to other states which do not belong to this group as is observed experimentally. The levels with alternate spin values having a similar structure have been pushed to very high excitation energies through the influence of the 1/2+[660] orbital and its large decoupling parameter.

Examination of the compositions of the remaining states and of the states to which each was found experimentally to decay indicates some degree of similarity. Where no transitions were found experimentally,

Figure 6-8

A comparison of the experimental excitation energies of the positive parity states and the values calculated using the Nilsson model with a deformation of $\delta = -0.15$.

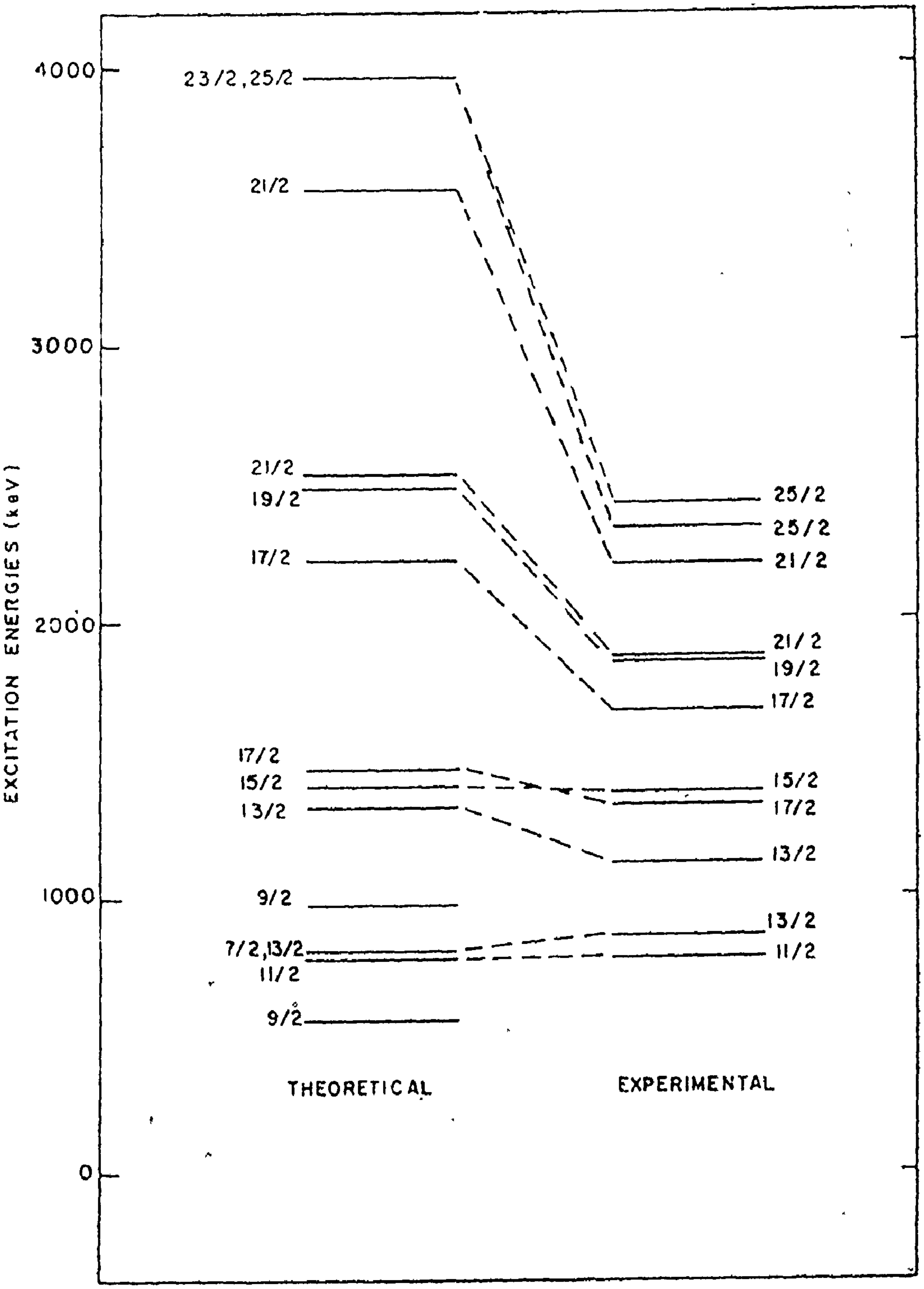
EXCITATION ENERGIES (keV)
4000
3000
2000
1000
0
23/2,25/2
21/2
21/2
19/2
17/2
17/2
15/2
13/2
9/2
7/2,13/2
11/2
9/2
25/2
25/2
21/2
21/2
19/2
17/2
15/2
17/2
13/2
13/2
11/2
THEORETICAL
EXPERIMENTAL

Figure 6-8

Table 6-8

Energies and Compositions of the Lowest Positive Parity States at Negative Deformations

SPIN	ENERGY (keV)	COMPOSITION 1/2 [560]	3/2 [651]	5/2 [642]	7/2 [633]	9/2 [624]	11/2 [615]	13/2 [606]
1/2	1805.1	1.00						
3/2	1582.8	.27	.96					
5/2	897.0	.62	.61	.50				
5/2	1496.1	-.62	-.02	.79				
7/2	800.5	.09	.36	.62	.69			
7/2	1562.0	-.20	-.61	-.37	.68			
9/2	563.2	.47	.46	.49	.48	.32		
9/2	970.8	-.56	-.34	.02	.44	.61		
11/2	785.0	.07	.26	.46	.60	.54	.25	
11/2	1481.0	-.12	-.40	-.47	-.13	.49	.60	
13/2	799.3	.55	.48	.45	.40	.29	.13	.03
13/2	1324.5	-.51	-.27	.06	.41	.58	.40	.11
15/2	1400.3	.07	.28	.47	.58	.52	.29	.08
15/2	2305.1	-.13	-.41	-.45	-.12	.42	.58	.08
17/2	1460.2	.63	.51	.42	.33	.22	.10	.03
17/2	2219.5	-.46	-.19	.15	.46	.58	.41	.14
19/2	2472.8	.08	.30	.49	.57	.49	.28	.09
19/2	3606.2	-.14	-.43	-.44	-.08	.43	.57	.30
21/2	2513.8	.68	.51	.40	.29	.17	.08	.02
21/2	3563.7	-.42	-.14	.20	.49	.58	.40	.15
23/2	3964.5	.09	.32	.50	.57	.47	.27	.09
25/2	3961.6	.71	.52	.38	.26	.15	.06	.02

Normalized to the $11/2^+$ state at 785.0 keV. $\delta = -0.15$, $\lambda = 51900$, attenuation = 0.75, $\Lambda = 50$ keV

Table 6-8 shows that the states concerned generally contain components of opposite phases which will reduce the transition intensity.

There are a number of disturbing points about this calculation. Experimentally no positive parity states of spin $< 11/2$ were observed. One might be able to rationalize this by claiming that the (α,2n) reaction does not seem to populate strongly low spin states even if they are low in excitation. However the $7/2^+$ state is calculated to have an excitation energy very close to that of the $11/2^+$ state at 785 keV so that there should be an E1 transition either to the $7/2^-$ ground state or 9/2- state at 379 keV. No such transition is observed. The calculation indicates that the $9/2^+$ state which has a structure similar to the other members of the band connected by the strong E2 cascade should also be observable but we find no experimental evidence for it nor the other low lying $9/2^+$ state which is also favourably located at 971 keV by the calculation.

Finally the $17/2^+$ state at 1346 keV which decays to the $13/2^+$ state at 852 keV via a strong 494 keV transition also decays to the $13/2^+$ state at 1116 keV by a weak 230 keV transition. However both of these transitions have approximately equal reduced transition intensities which implies that the compositions of the two $13/2^+$ states should be quite similar when in fact they are not so calculated.

Hence the Nilsson model including Coriolis coupling, quasi-particle formulation and residual interactions fails to reproduce the observed structure to any significant degree.

6.4.3 Alternative Models

6.4.3.1 The Assymetric Rotor Model

A set of positive parity states which is similar in some respects to those of ^{151}Gd has been observed in ^{191}Pt (Khoo et al (1976)). These are presented to the left hand portion of Fig. 6-6. Although in both nuclei there is both a favoured (I = j, j + 2, j + 4 . . .) and an unfavoured (I = j - 1, j + 1, j + 3 . . .) band, the latter is much lower in excitation in ^{151}Gd than in ^{191}Pt. Moreover, in ^{151}Gd there is a second favoured band at low excitation.

The structure of ^{191}Pt has been explained in terms of the model of Meyer-ter-Vehn (1975) by coupling holes in the $i_{13/2}$ shell to a rotating core with $\gamma = 30°$. The similarity between the two level schemes suggests that ^{151}Gd might be accounted for by coupling a few $i_{13/2}$ particles to a core with $\gamma \sim 30°$. The results of such a calculation are shown at the extreme right of Fig. 6-6. In this calculation γ was set at 34°, the Fermi level (λ) at 1.3 MeV above the $\nu = 1$ state and the pairing parameter (Δ) at 0.89 MeV. The rotational parameter, 57.3 keV, was derived from the energy of the first 2^+ state in ^{152}Gd. The large value of λ implies that the $i_{13/2}$ shell is filled past the $\nu = 2$ state and seems physically unreasonable since it is not clear why there should be three particles in the $i_{13/2}$ shell for an N = 87 nucleus.

The calculated wave functions for the case shown in Fig. 6-6 have been used to obtain the energy reduced E2 branching ratios shown in Table 6-9. The agreement is especially remarkable since the calculation

Table 6-9

A Comparison of the Branching Ratios

Predicted by the Meyer ter Vehn Model with Experiment

	Theory[a]	Experiment
$\frac{17/2_1 \rightarrow 13/2_2}{17/2_1 \rightarrow 13/2_1}$	0.012	0.016±0.005
$\frac{17/2_2 \rightarrow 13/2_2}{17/2_2 \rightarrow 13/2_1}$	2.7	2.3±0.7

a) The intensities predicted by the model have been adjusted to allow for the differences between the predicted and observed transition energies.

is comparing inter-band to intra-band intensities. Unfortunately, the M1 transition strengths are not at all well predicted by the model.

Although the parameters needed to fit the positive parity levels of ^{151}Gd to the triaxial-rotor-plus-particle model may be somewhat unusual, the striking agreement between the calculation and the experiment suggests that further study of the applicability of the model to this region might be fruitful.

6.4.3.2 The Modified Nilsson Calculation

The present data have shown that the present Nilsson model code consistently and progressively overestimates the excitation energy of rotational band members as the spin of the state increases. It is also obvious that this effect is due to the rigid rotor formulation which assigns a single value to the moment of inertia for all members of a rotational band. The analysis of the data on the $11/2^-$[505] band with respect to the VMI model shows that the moment of inertia is strongly dependent on the spin of the state (Fig. 6-3). Hence the specification of the input basis states for the odd A calculation should reflect the "rotational content" of each state as far as the varying moment of inertia parameter is concerned.

One way to accomplish this involves assuming that the rotational behaviour of each odd nucleus is dominated by that of the adjacent even mass core. Then each unperturbed rotational state in a given Nilsson band $|IMK\rangle$ could be characterized by the fraction of each value of the core angular momentum $\underline{R}$ allowed by the vector coupling of $\underline{R}$ and $\underline{j}$ to $\underline{I}$

contained in that state. Let us call these fractions P(IKR). The effective moment of inertia parameter for each rotational state $|IK\rangle$ can then be expressed as $1/2\,\mathcal{I}_{1K}$, where $\mathcal{I}_{IK}$ is the weighted sum of the core moments of inertia for each value of R contained in that state, the weighting factors being P(IKR). Hence

$$\mathcal{I}_{IK} = \sum_{R} \mathcal{I}_R\, P(IKR)$$

and

$$A_{IK} = \hbar/2\mathcal{I}_{IK}$$

The energies of the unperturbed rotational states $|IK\rangle$ would then be

$$E_{IK} = E_K + A_{IK}[I(I+1)-2K^2+\langle j^2\rangle+\delta_{K\frac{1}{2}}\alpha(-1)^{I+\frac{1}{2}}(I+\tfrac{1}{2})]+\tfrac{1}{2}C(\mathcal{I}_{IK}-\mathcal{I}_{0K})^2 \qquad [6\text{-}5]$$

The last term in equation 6-2 is added in analogy with the VMI model to provide the "elastic energy" term. The constant C previously termed the "softness" parameter should probably be obtained from a VMI fit to the ground state rotational band of the even A core.

Although the above procedure is a relatively straight-forward method to simulate approximately the core behaviour in these odd A nuclei, it lacks self consistency. The weighting factors P(IKR), used to calculate the moments of inertia depend intimately upon the deformation through the C_{jk} coefficients used in the expansion of the Nilsson state of the odd particle in the spherical basis. Thus a correct calculation of the moments of inertia in a rotating nucleus whose deformation is not constant must necessarily include a set of C_{jk}'s for each rotational state. The P(IKR) must therefore be redetermined for each rotational state in a manner which generates a self consistent set of moments of inertia.

As a consequence of the complication inherent in the calculation described above, Smith and Rickey (1976) adopted an alternative approach to imposing a realistic core behaviour effect on the unperturbed odd particle state. Their procedure involves an adaptation of the VMI model for these states.

These authors were attempting to obtain a theoretical description of energy level diagrams obtained in experiments on ^{101}Pd, ^{103}Pd and ^{105}Pd which bear a strong resemblance (Fig. 6-9) to those which we have observed in ^{151}Gd. VMI fits to the ground state rotational bands of the even A core nuclei in each case yielded $\mathcal{I}_0 \sim 0$. As a result the minimization of the rotational energy with respect to $\mathcal{I}$ at each spin I for $\mathcal{I}_0 = 0$ yields

$$\mathcal{I}_{IK} = \mathcal{I}_{I0} = [I(I+1)/2C]^{1/3} \text{ keV}^{-1} .$$

As a first approximation they express the odd-A moments of inertia as

$$\mathcal{I}_{IK} = \big((1/2C)[I(I+1) - 2K^2 + \langle j^2\rangle + \delta_{K\frac{1}{2}}\, \alpha(-1)^{I+\frac{1}{2}}\big)^{1/3}$$

The rotational energies to be used as input to the Coriolis calculation are then expressed as in equation 6-3. In the Coriolis calculation C and $\mathcal{I}_{0K}$ were treated as free parameters to be varied over restricted ranges. In addition the rotational parameter which appears as the energy scale factor in the Coriolis matrix element, H_{kk}, was set equal to the

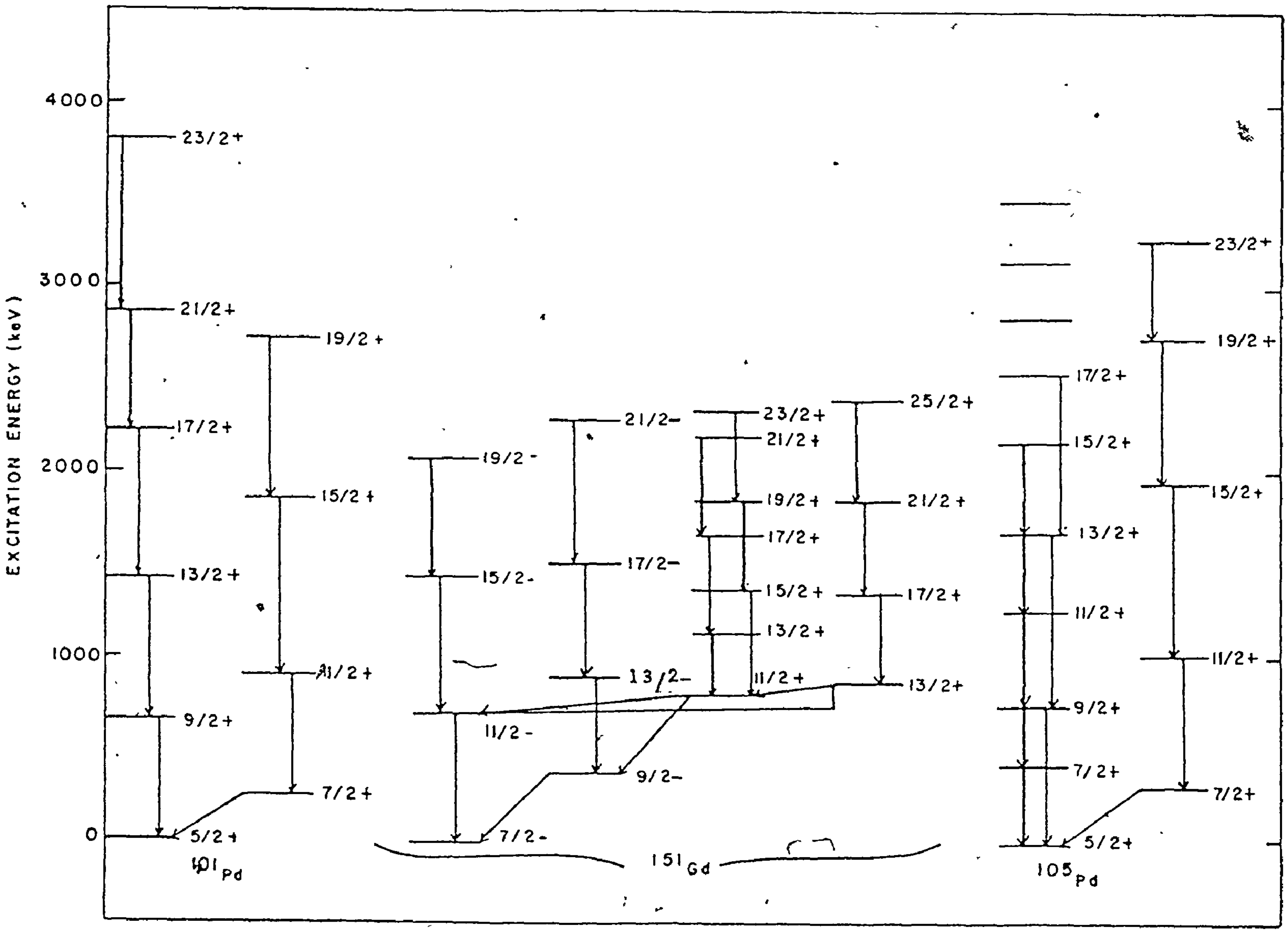

Figure 6-9

A comparison of the experimental excitation energies of the positive parity states in ^{151}Gd, ^{101}Pd and ^{105}Pd.

average value of A_{IK} and $A_{IK'}$.

Calculations of the effective moment of inertia parameter for their positive and negative parity bands are presented in Figure 6-10 reproduced from their article (Smith and Rickey (1976)).

The spin dependence of A_{IK} and hence $\mathcal{I}_{IK}$ is seen to be monotonic in all bands except the K = ½ bands where the presence of the diagonal Coriolis term induces oscillation in $\mathcal{I}$ with spin. The oscillation turns out to be essential to the success of their calculations since a calculation based on a K = ½ band with a monotonic $\mathcal{I}$ produced energy levels which in no way resembled the observed spectra.

As a result of this simple modification to their Nilsson-Coriolis coupling calculation they obtained a high degree of success in describing the excitation energies of both positive and negative parity states, reduced transition probabilities and (d,p) and (d,t) spectroscopic factors.

Unfortunately, the time required to adapt the present Coriolis coupling code to the Smith and Rickey model is not available.

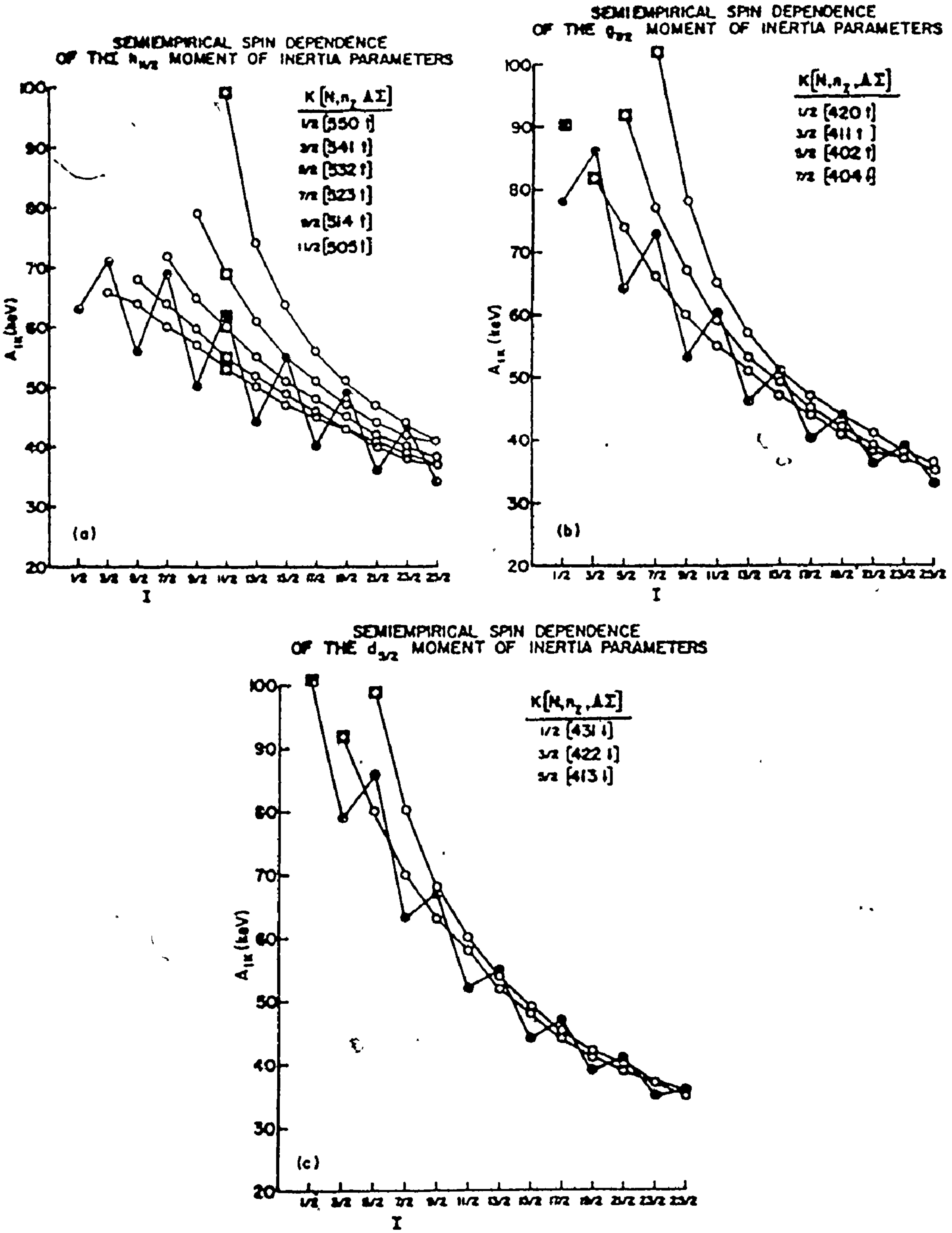

Figure 6-10

Semiempirical moment of inertia paramters for the odd neutron Nilsson states from the $h_{11/2}$, $g_{7/2}$ and $d_{5/2}$ shell model states. The points enclosed in squares represent the value of the parameter $1/(2I_{0K})$ used for each band. (Reproduced from Smith and Rickey ,1976)

CONCLUSION

The discussion of Chapter 6 has shown that the standard Nilsson model calculation employing a rigid rotor and Coriolis coupling and including pairing and residual interaction effects is inadequate for describing the structure of ^{151}Gd.

We can be quite certain from the data obtained regarding the $11/2^-$[505] band that when this orbital is occupied the nucleus has a prolate deformation of $\delta \sim +0.3$

Using the relation derived by Kleinheinz et al (1972) shown as equation 6-1, both the positive and other negative parity states ($11/2^-$ band not included) indicate a deformation of $\delta \sim +0.15$. However, it was necessary to use an oblate deformation for the positive parity states and a prolate deformation for the negative parity states to obtain a very limited agreement on relative positions of energy levels. Unless we believe that ^{151}Gd has a different stable deformation for each orbital occupied by the odd nucleon, it is clear that the Nilsson model as it presently stands cannot describe in a consistent manner the structure of this nucleus.

The assymetric rotor model of Meyer ter Vehn calulated quite closely the relative positions of the positive parity states but has as yet not yielded any explanation of those negative parity states which are not connected to the $11/2^-$[505] band. It calculates quite accurately the energy reduced E2 branching ratios of some of the positive parity states though some of the assumptions used in the triaxial calculation are unreasonable and M1 transition strengths are not well predicted. Furthermore this model fails to produce the experimentally observed compression of the energy spacings.

The "decoupled band theory" of Stephens et al (1974 accounts for only four positive parity states. The early good agreement between the calculations of this model and the observed level energies was shattered by the discovery of the incorrect parity of the group of states feeding the level at 785 keV. This gave rise to many more positive parity states than the model could produce including an $11/2^+$ state which lies below the $13/2^+$ bandhead, a situation which cannot occur according to the model. The formulation does however provide the observed compression of the energy levels though from the theoretical development in Chapter 3 it can be seen that this is caused by effectively altering the rotational parameter of the band according to the spin of the level.

This is a step in the right direction but it can be achieved more naturally through the variable moment of inertia model of Mariscotti et al (1969) rather than introducing a new coupling scheme. It is easy to conceive of the centrifugal stretching of a flexible body as the rotation frequency increases.

The VMI fit of the $11/2^-[505]$ rotational band is the most successful model tested on the present data. However it cannot stand alone because it is not microscopic in nature i.e. it cannot produce the relative positions and energy spacings of each energy level from a description of the orbitals.

The next step has already been taken by Smith and Rickey (1976). These authors have built an approximate formulation of the VMI theory into a Nilsson model calculation with pairing and Coriolis coupling. They have been extremely successful in calculating energy levels for a number of Pd nuclei in which the structure seems to be quite similar to that of ^{151}Gd. Crucial to the success of their model is the oscillation of the moment of inertia with spin value for the $K = 1/2$ bands. Without this they were unable to reproduce the observed level schemes. When it is included they obtain excellent agreement between the measured and calculated energy levels and reasonable agreement for reduced transition probabilities and (d,p) and (d,t) spectroscopic factors.

In any theory which embraces the VMI model it is implicit that the nuclear deformation is a dynamic variable if even only over a small range. It is possible that whatever discrepancies remain in the work of Smith and Rickey (1976) may be resolved by refinements to their model. At present wave functions are constructed under the assumption of constant deformation, thus the intrinsic Coriolis matrix elements as well as the reduced electromagnetic transition matrix elements do not fully reflect the dynamic behaviour of δ. Furthermore the parameters C and $\mathcal{I}_{0K}$ are not obtained in a fully-self consistent manner and work in this direction may further improve the already good agreement they have obtained. They also suggest that the model be further extended to include the assymetric rotor formulation and allow β and γ degrees of freedom.

In essence what they are proposing is a very generalized Nilsson-type model which contains the major embellishments which presently each stand alone, none being capable of doing the job by itself and enjoying only a limited success.

The effort involved in modifying our own Nilsson model code to the Smith and Rickey model is now beyond the scope of this project. However this work should be given the highest priority for future development along with new experiments to populate states of very high spin since the new model has many degrees of freedom.

The states of ^{151}Gd may very well find their explanation in the model of Smith and Rickey and it is the author's sincere belief that this will be the most fruitful path to obtain not only a description of transitional nuclei but to broaden the scope of the Nilsson model so that its validity ranges along the entire periodic table.

POSTSCRIPT

As this thesis goes to press another paper by Kleinheinz et al, 1977, has become available wherein those authors have redone the experiments on ^{151}Gd and included linear polarization measurements in order to have an independent check on the multipolarity of various gamma rays. Their experiments confirm our determination of the parities of the levels which I had disputed in their earlier work (Kleinheinz et al,1974) on the basis of the conversion electron work.

The major remaining difference between their work and the present thesis is the spin of the 1115.7 keV level. They have chosen to assign it $J^\pi = 9/2^+$ on slightly weaker grounds than I chose $13/2^+$. The coincidence data available to me indicates a number of weaker transitions which could not fit into the decay scheme if the state is $9/2^+$.

They feel that the theoretical explanation of the $13/2^+$ band is probably the result of at least three neutrons placed in the $i_{13/2}$ shell perhaps with an asymmetric core. This is in contrast to the simplest expectation of a single particle excitation for a nucleus with only five neutrons outside the closed N=82 neutron shell. This is in contrast to the feeling of the author that the single particle excitation in the context of the Smith and Rickey model may prove to be successful in explaining the data.

They conclude also that little can be said of a quantitative nature regarding the states of the $f_{7/2}$ and $h_{9/2}$ bands since multiple particle excitations result in a situation where j is no longer a good quantum number and rigorous particle plus rotor calculations for Nilsson orbitals with mixed j are not readily accessible.

Hence a considerable amount of theoretical work remains to be done to provide an unambiguous explanation of the observed level scheme of ^{151}Gd , and one would expect, other transitional nuclei.

Kleinheinz, P., 1977, Nucl. Phys. A283.

REFERENCES

1. Afanasiev, V.P., Budzynski, M., Demeter, I., Fuya, H., Gromov, K.Y., Gromova, I.I., Holbaev, I., Ion-Mihai, R., Maczka, D., Morosov, V.A., Muminov, T.M., Zhu k, V., 1974, JINR-E6-8327.
2. Alaga, G., Alder, K., Bohr, A. and Mottelson, B.R., 1955, Kgl. Danske Videnskab. Mat. Fys. Medd. 29, No. 9.
3. Alexander, P., Boehm, F., and Kankeleit, E., 1964, Phys. Rev. 133, B284.
4. Bardeen, J., Cooper, L.N., and Schrieffer, J.R., 1957, Phys. Rev., 108, 1175.
5. Bohr, A. and Mottelson, B.R., 1953, Kgl. Danske Videnskab, Selskab, Mat. Fys. Medd., 27, No. 16.
6. Bohr, A. and Mottelson, B.R., 1963, Atomn. En. 14, 41.
7. Borggreen, J., Lovhoiden, G. and Waddington, J.C., 1969, Nuc. Phys., A131, 241.
8. Cook, W.B., 1972, Ph.D. Thesis, McMaster Univ.
9. Cook, W.B., Waddington, J.C., Burke, D.G. and Nelson, D.E., 1973, Can. J. Phys., 51, 1978.
10. Cook, W.B., Johns, M.W., Løvhøiden, G., and Waddington, J.C., 1975, Nucl. Phys. A259, 461.
11. Davydov, A.S. and Filipov, G.F., 1958, Nucl. Phys. 8, 237.
12. Ejiri, H., Ishihara, M., Sakai, M., Katori, K. and Inamura, T., 1968, J. of the Phys. Soc. of Japan, 24, No. 6, 1189.
13. Ekstrom, C., Ingelman, S., Olomats, M. and Wannberg, B., 1972, Physica, Scripta, 6, 181.
14. Geiger, J.S., 1965, AECL Report CRGP-1214.

15. Gonsior, M., Gromova, I.I., Ishkakov, G.I., Kuznetsov, V.V., Kuznetsova, M.Y., Mikhailov, M., Potempa, A.V., and Fominykh, V.I., 1971, Acta Phys. Pol. B2, 307.

16. Gregory, P.R. and Taylor, T., 1972, Phys. Letters, B41, 122.

17. Grover, J.R., 1967, Phys. Rev. 157, 832.

18. Grover, J.R., and Gilat, J., 1967a, Phys. Rev. 157, 802.

19. Grover, J.R., and Gilat, J., 1967b, Phys. Rev. 157, 814.

20. Grover, J.R. and Gilat, J., 1967c, Phys. Rev. 157, 823.

21. Hager, R.S. and Seltzer, E.C., 1968, Nuc. Data. A4, Nos. 5,6.

22. Hammaren, E., Puhakka, P., Siivola, A., Tuurnaka, T., 1975, Zeits Phys. A272, 341.

23. Harmatz, B., 1976, Nucl. Data Sheets, 19, 33.

24. Hecht, K.T. and Satchler, G.R., 1962, Nucl. Phys. 32, 286.

25. Jackson, J.D., 1956, Can. J. Phys., 34, 767.

26. Jagare, S., 1967a, Nucl Phys., A95, 481.

27. Jagare, S., 1967b, Nucl. Phys., A95, 491.

28. Khoo, T.L., 1972, Ph.D. Thesis, McMaster Univ.

29. Khoo, T.L., Waddington, J.C., Preibisz, Z. and Johns, M.W., 1972, Nucl. Phys. A202, 289.

30. Khoo, T.L., Bernthal, F.M., Dors, C.L., Piiparinen, M., Saha, S., Daly, P.J. and Meyer ter Vehn, J., 1976, Phys. Letters 60B, 341.

31. Khoo, T.L., Waddington, J.C., Preibisz, Z., and Johns, M.W., 1972, Nucl. Phys. A202, 289.

32. Kleinheinz, P., Maier, M.R., Sheline, R.K., Diamond, R.M., Stephens, F.S., Sheck, W., and Stefanini, A., 1974, Institute for Nuclear Physics, Julich, Annual Report, 104.

33. Kormicki, J., Niewodniczanski, H., Stachura, Z., Zuber, K., Budziak, A., 1967, Acta Phys. Pol., 31.

34. Lederer, C.M., Hollander, J.M. and Perlman, I., 1968, Table of Isotopes, 6th edition.

35. Løvhøiden, G., Waddington, J.C., Hagemann, K.A., Hjorth, S.A., Ryde, H., 1970, Nucl. Phys. A148, 657.

36. Løvhøiden, G., Hjorth, S.A., Ryde, H. and Harms-Ringdal, L., 1972, Nucl. Phys. A181, 589.

37. Løvhøiden, G., and Burke, D.G., 1975, Can. J. Phys. 53, 1182.

38. Mariscotti, M.A.J., Scharff-Goldhaber, G. and Buck, B., 1969, Phys. Rev. 178, 1864.

39. Mayer, M.G. and Jensen, J.H., 1955, Elementary Introduction of Nuclear Shell Structure, New York.

40. MeyerterVehn, J., Stephens, F.S. and Diamond, R.M., 1974, Phys. Rev. Letters. 32, 1383.

41. MeyerterVehn, J., 1975, Nucl. Phys. A249, 111.

42. Mikhailov, V.M. and Mikhailova, M.A., 1966, Izv, Akad. Nauk. USSR 30, 1337.

43. Nathan, O. and Nilsson, S.G., 1965, Alpha-Beta-and-Gamma-Ray Spectroscopy, ed. by K. Siegbahn, Vol. 1, 601. North Holland Publ. Co., A sterdam.

44. Newton, J.O., Stephens, F.S., Diamond, R.M., Kotajima, K., Matthias, E., 1967, Nucl. Phys. A95.

45. Newton, J.O., 1969, Prog. in Nucl. Phys., Vol. 11, Ed. by Brink, D.M. and Mulvey, J.H., Pergamon Press, Oxford.

46. Newton, J.O., Stephens, F.S., Diamond, R.M., Kelly, W.H. and Ward, D., 1970, Nucl. Phys. A141, 631.

47. Newton, T.D., 1960, Energy Levels of a Completely Anisotropic Oscillator, Can. J. Phys. 38, 700 and Chalk River Report CRT-886.

48. Nilsson, S.G., 1955, Kgl. Danske Videnskab. Selsk., Mat. Fys. Medd. 29, No. 16.

49. Preston, M.A., 1962, Physics of the Nucleus, Addison-Wesley Publ. Co. Inc. Mass.

50. ScharffGoldhaber, G. and Goldhaber, A., 1970, Phys. Rev. Letters 24, 1626.

51. Smith, H.A. and Rickey, F.A., 1976, Phys. Rev. C 14, No. 5, 1946.

52. Smith, H.J., Burke, D.G., Johns, M.W., Lovhoiden, G., and Waddington, J.C., 1973, Phys. Rev. Letters, 31, 944.

53. Smith, H.J., Waddington, J.C., Johns, M.W., 1975, Bul. Am. Phys. Soc., Ser. II, 20, 624.

54. Sood, P.C., 1957, Phys. Rev. 161, 1063.

55. Sorensen, R.A., 1973, Rev. Mod. Phys. 45, 353.

56. Stephens, F.S., Diamond, R.M., Leigh, J.R. Kammuri, T. and Nakai, K., 1972, Phys. Rev. Letters 29, 438.

57. Stephens, F.S., Diamond, R.M. and Nilsson, S.G., 1973, Phys. Letters 44B, 429.

58. Stephens, F.S., 1975, Rev. Mod. Phys. 47, No. 1.

59. Thompson, J.V., Singh, B. and Johns, M.W., 1975, Physics in Canada 31, # 3, 31 and unpublished work.

60. Tjom, P.O. and Elbek, B., 1967, Kgl. Danske Videnskab. Selskab. Mat. Fys. Medd. 36, Number 8.

61. Trainor, L.E.H. and Gupta, R.K., 1971, Can. J. Phys. 49, 133.

62. Vergnes, M.N. and Rasmussen, J.O., 1965, Nucl. Phys. 62, 233.

63. Vilskii, K., 1967, Yad. Fis. 6.

64. Volkov, A.B., 1971, Physics Letters, 35B, No. 4, 299.

65. Volkov, A.B., 1972, Phys. Letters, 41B, 1.

66. Weiskopf, V.F. in Theoretical Nuclear Physics (Wiley, New York 1952) by Blatt and Weiskopf.

67. Yamazaki, T., 1967, Nuclear Data, A3, 1.